Summer 7-15-2017

Designing Nanocomposite Materials For Catalyzing Electrochemical Reactions in Anion Exchange Membrane Fuel Cells

Sadia Afrin Kabir
University of New Mexico

Sadia Afrin Kabir

Candidate

Department of Chemical and Biological Engineering

Department

This dissertation is approved, and it is acceptable in quality and form for publication:

Approved by the Dissertation Committee:

Dr. Plamen Atanassov, Chairperson

Dr. Alexey Serov

Dr. Fernando Garzon

Dr. Kateryna Artyushkova

Dr. Vijay Ramani

DESIGNING NANOCOMPOSITE MATERIALS FOR CATALYZING ELECTROCHEMICAL REACTIONS IN ANION EXCHANGE MEMBRANE FUEL CELLS

by

SADIA AFRIN KABIR

MS Chemical Engineering, University of New Mexico, 2013
BE (Honors) Chemical Engineering, BITS-Pilani, Dubai, 2011

DISSERTATION

Submitted in Partial Fulfillment of the
Requirements for the Degree of

Doctor of Philosophy
Engineering

The University of New Mexico
Albuquerque, New Mexico

July, 2017

DEDICATION

I dedicated this work to my dear family for giving me the support and inspiration I needed to come this far.

Acknowledgements

I would like to thank my advisor, Dr. Plamen Atanassov for his continuous support and guidance through the years. I consider myself to be immensely fortunate in having the opportunity to work and learn from his work and for being engaged with his research group. He has always kept me motivated, encouraged my work through his enthusiasm, and his immense knowledge. I could not have imagined having a better advisor and mentor. Needless to say, his words of advice and professional style will remain with me as I continue my career.

I would like to express my sincere gratitude to my co-advisor Dr. Alexey Serov for always assisting me in designing and executing these experiments. His guidance provided me the foundation that I needed to develop my dissertation. I also thank the members of my dissertation committee, Dr. Fernando Garzon, Dr. Kateryna Artyushkova, and Dr. Vijay Ramani for their valuable recommendations pertaining to this study and their assistance for my professional development.

Last but not the least, I want to thank my family for giving me the support I needed to achieve my goals and dreams, I could not have done this without them.

Designing Nanocomposite Materials For Catalyzing Electrochemical Reactions in Anion Exchange Membrane Fuel Cells

by

Sadia Afrin Kabir

BE (Honors) Chemical Engineering, BITS-Pilani, Dubai, 2011

MS, Chemical Engineering, University of New Mexico, 2013

PhD, Engineering, University of New Mexico, 2017

Abstract

Fuel cells are considered to be one the most promising sustainable energy technologies for energy conversion and electric power generation. With the development of stable, conductive and high performance anion exchange membranes and ionomers, there has been an increased interest towards studying various electrochemical reactions in Anion Exchange Membrane Fuel Cells (AEMFC). This increased attention has been attributed to the comparatively facile reaction kinetics, minimized corrosion effects and reduced fuel crossover in alkaline media. However, the oxygen reduction reactions (ORR) taking place in the cathode compartment of fuel cells plays a crucial role in optimizing the electrochemical energy conversion efficiency, which is why it's imperative to design electrocatalysts that can efficiently catalyze the electroreduction of oxygen in alkaline media.

Various studies have demonstrated the improved intrinsic activity, stability and accessibility of Palladium/Graphene-based nanocomposites for ORR in alkaline electrolytes, although their integration into operating AEMFCs have been quite limited to date. This is mainly due to the challenges associated with (i) synthesizing Pd nanoparticles without

surfactants and organic stabilizers (ii) fabricating porous graphitized supports with controlled morphologies that can form triple phase boundaries and (iii) a lack of standardization and optimization for integrating these nanocomposite materials into the membrane electrode assemblies of AEMFCs.

This work addresses the current limitations and technical challenges by providing a synthetic strategy for designing Pd/Graphene nanocomposites with i) controlled surface to volume ratios for enhancing the solid-liquid-gas phase boundaries, ii) modified chemical properties for improving nanoparticle dispersion and electrochemical accessibility and iii) targeted tuning of active sites through nitrogen functionalization for oxygen electroreduction in alkaline media. In particular, stable size-controlled Pd nanoparticles were synthesized using surfactant free technique and deposited on hierarchically structured nitrogen doped 3D-Graphene nanosheets that were fabricated with varying levels of micro-, and macro-porosities developed using a sacrificial templating and pyrolytic methods. Using a synergetic combination of potentiodynamic, surface analysis and spectroscopic techniques, it was demonstrated that the porosity, surface functionalization, and the nature of nitrogen moieties doped into played a significant role in in modifying the size, dispersion, electrochemical accessibility as well as activity of the Pd nanoparticles for oxygen electroreduction in alkaline media. The Pd/3D-Graphene composite materials were also integrated into a catalyst coated membrane, optimized (assembly, activation, electrode fabrication) and analyzed for their performance in H_2/O_2 fed AEMFCs operating at 60°C. It was demonstrated that conditioning of the membranes was crucial for reducing ohmic losses, whereas porosity of the supports was imperative for facilitating mass transport kinetics.

Overall, this work analyzes how the morphological and chemical properties of graphitized supports can be modified to play a key role in improving oxygen electroreduction pathways not only in the alkaline electrolytes, but also in minimizing concentration polarization losses in operating AEMFCs. The results in this study further highlights the importance of rationally designing nanomaterials for high-performance energy conversion devices, and can also be expanded to other energy storage and conversion applications such as electrodes for Li-air batteries and electrolyzers.

Table of Contents

List of Figures

List of Tables

Chapter 1

Introduction

Fuel cells are considered to be one of the most promising sustainable energy technologies for energy conversion and electric power generation. Due to their high electrical efficiency, low operating temperatures and zero tailpipe emissions, fuel cells have become ideal candidates for both transportation and residential applications.[1, 2] This is also reflected in the growing distribution of fuel cell vehicles (FCVs) in the public markets of Japan, USA and Europe pioneered by some of the world leaders in automobile manufacturing such as Toyota and Hyundai have demonstrated that fuel cells are no longer limited to niche markets. For example, fuel cell powered busses and other mobile vehicles (forklifts etc.) have been widely deployed in many cities around the globe by various municipal authorities as well as governmental entities. The increasing demand of reliable backup systems for critical civilian infrastructures such as hospitals, cell phones towers etc. have also resulted in an aggressive penetration of the existing market by fuel cell manufacturing companies such as Ballard and Intelligent Energy. Countries with a decentralized heating supply to the residential properties are now looking forward to integrating Combined Heat and Power (CHP) devices in newly constructed buildings. These CHP devices can inherently produce both electricity and heat for everyday needs of tenants from a single fuel source.[3, 4]

1.1 Polymer Electrolyte Membrane Fuel Cells

The first practical fuel cell resulted from the work begun in England in 1932 by F.T. Bacon resulted in design of 1.5 kW Apollo alkaline fuel ce11[5] operating with a KOH-H_2O electrolyte solution. However, the technology that revolutionized the current state-of-the-art fuel cells resulted from the Gemini earth-orbiting space mission (1962 to 1965) that utilized a solid polymer electrolyte - called an ion-exchange membrane (IEM) at that time – which consisted of a cationic membrane of sulfonated polystyrene resin. Since then, different types of fuel cells developed over the years - primarily classified according to (i) the type of fuel they use, (ii) the temperatures they operate at and (iii) the electrolyte or membrane utilized for transferring the ions generated during the oxidation/reduction reactions. For example, Proton Exchange Membrane Fuel Cells (PEMFC) typically operate below 100°C, whereas Phosphoric Acid Fuel Cells (PAFC) operate at medium temperatures of 150-220°C. High temperature operation is typically carried out in Molten Carbonate and Solid Oxide fuel cells, where temperatures of about 600-1000°C are usually encountered. The subject of discussion here is limited to low temperature devices such as PEM and AEM fuel cells.

1.1.1 Electrocatalyts for Proton Exchange Membrane Fuel Cells

The development of catalytic materials is essential to activate the electrochemical reactions involved in low temperature fuel cells. Electrocatalysts are routinely utilized to facilitate the kinetics of the redox reactions by decreasing the activation barrier. At present, platinum – mostly in the form of nanoparticles sized between 3-4 nm supported on carbon, [6, 7] in order to achieve the maximum number of active sites [8], or alloyed with other metals.is considered to be the most active catalyst for oxygen reduction reactions [9, 10]. Generally, a Pt loading

≤0.05 mg_{Pt} cm^{-2} is required to catalyze hydrogen oxidation reactions in the anode compartment of PEMFCs, where as much higher loading of ≈0.2–0.4 $mg_{Pt} \cdot cm^{-2}$ is required to catalyze the oxygen reduction reactions (ORR) in the cathode compartment of PEMFC, because of the sluggish ORR kinetics. Hence, current PEMFCs are heavily reliant on Pt, which accounts for up to half of the entire fuel cell cost. [11, 12]

In order to minimize costs, researchers have focused on decreasing the amount of Pt loading by reducing its particle size, modifying the shape, or alloying it with other 3d transition or oxophillic metals such as Ru, Rh etc.[6, 13] However, these methods have not been successful in mitigating the dissolution or instability of the nanoparticles under fuel cell operating conditions. [14]

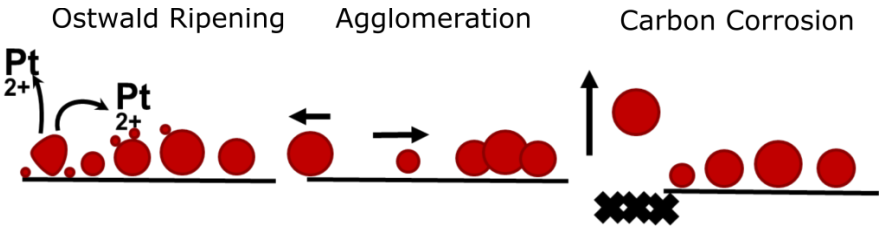

Figure 1. Simplified representation of degradation mechanisms for platinum nanoparticles on a carbon support.

1.1.2 Instability of Platinum in Proton Exchange Membrane Fuel Cells

Most of the instability is attributed to platinum dissolution which occurs during operation, and is expected to be worse for smaller nanoparticles. The main pathways for Pt dissolution involve either the direct dissolution of metal or an oxide film formation and a subsequent chemical reaction. If the dissolved or detached smaller platinum nanoparticles get redeposited on larger platinum particles, significant particle growth can occur and the according degradation mechanism is called Ostwald ripening. Agglomeration and

coalescence can also occur if dissolved Pt is redeposited on larger Pt particles, significant particle growth can occur, along with migration and collision of platinum particles on the surface of the carbon support with successive coalescence.

1.1.3 Carbon Corrosion in Proton Exchange Membrane Fuel Cells

In order to prevent sintering, Pt nanoparticles are usually supported on carbon black supports such as Vulcan XC-72R (Cabot Corp.) and Ketjen Black (KB EC600JD & KB EC600J, AkzoNobel). [15, 16] However, although corrosion of conventional carbon supports such as Vulcan is considered negligible at cell voltages lower than 0.8 V in low-temperature fuel cells, carbon corrosion and weight loss has been shown to be significant at voltages higher than 1.1 V vs. RHE. Studies have shown that conventional electrodes in automotive fuel cell stacks suffer from catastrophic failure due to degradation of the amorphous carbon supports during start-up/shut-down transients and load cycling.[17] Carbon corrosion can also result in accelerated degradation of catalysts due to an increase in oxygen-containing groups on the carbon surface will also impair the conductivity of carbon and mass transport of oxygen. Moreover, severe carbon corrosion can inevitably leading to Pt detachment and dissolution due to weakening of the interaction between particle and support, leading to losses in fuel cell efficiency.

Hence, even after decades of research on the Proton Exchange Membrane Fuel Cell (PEMFC) technology, its wide-scale implementation is still limited [14, 18] due to the instability and degradation of the Pt nanoparticles[19] under fuel cell operating conditions,[10, 20] the sluggish oxygen reduction reaction (ORR) kinetics[21] and corrosion of the amorphous

carbon black support[22]. Therefore, to further scaling up and commercialization of fuel cell technology, the development of alternative electrocatalysts and systems have become a high research priority and have prompted the research community to delve further into other types of fuel cells that can utilize non-Pt catalysts, such as Anion Exchange Membrane Fuel cells.

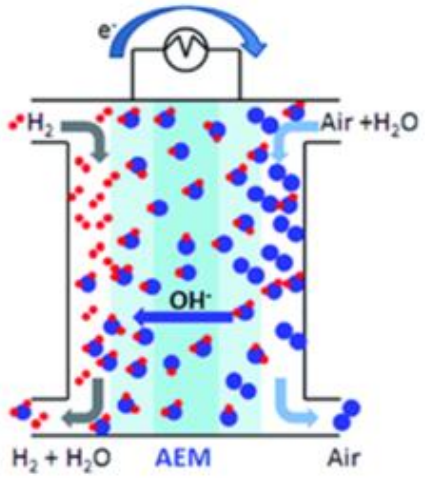

Figure 2. Schematic comparison of an Anion Exchange Membrane Fuel Cell (AEMFC, left) that are supplied with H_2 and air. Reproduced from Ref. [23]

1.2 Anion Exchange Membrane Fuel Cells

Anion Exchange Membrane Fuel Cells are a type of alkaline fuel cell (AFCs) which were first developed in the 1930s by F. T. Bacon. These early alkaline fuel cells operated with H_2 between 50-200°C and employed a liquid electrolyte (e.g., an aqueous solution of KOH) and used by NASA in the 1960s to power Apollo space missions. However, liquid electrolytes lead to formation of carbonate precipitate, which reduced the performance of AFCs. But, with recent developments made in fabricating membranes that can conduct OH- ions, the KOH electrolyte has been replaced with anion exchange membranes (AEM), which is basically an alternative to the proton exchange membrane which utilizes the

separator and ionomer made from polymeric materials. The alternative membranes are called Anion Exchange Membranes (AEM) or Alkaline Electrolyte Membranes due to their ability to conduct hydroxyl ions (OH^-) as opposed to protons) during current flow (see Fig.2).

AEMs are solid polymer electrolyte membranes that contain positive ionic groups (usually quaternary ammonium (QA) functional groups such as poly- NMe_3^+) and mobile negatively charged anions. The replacement of the traditional caustic aqueous potassium hydroxide [KOH(aq)] electrolyte with suitable commercial-available such as those from Tokuyama Co (Japan), Fumatech (Germany) or other AEM suppliers have shown great potential to substitute PEMs due to their enhanced performances.[24, 25]

With the advancements made in OH- conducting polymer electrolyte membranes– Anion Exchange Membrane Fuel Cells (AEMFC) have gained renewed and increased attention.[24-27] due to several advantages: enhanced electrokinetics of most complex reactions at high pH [28], reduced fuel cross-over from anode to cathode, lower OH^- poisoning, supposed minimized corrosion of the electrode materials at high pH [29] and therefore potential flexibility of substituting Pt-based catalysts with others metals (that are generally not stable in acidic environment and high potential values) such as palladium, silver, manganese oxide and carbon-nitride materials [30-33]. Utilizing Pt-free catalysts for fuel oxidation on the anode as well as oxygen reduction on cathode [34, 35] substantially decreases the total price of final fuel cell systems. Besides, in alkaline conditions, hydrogen can be replaced by other fuels, easily stored and transported, such as alcohols [36-40] or boron-based [41-44] and nitrogen-based [45-47] compounds.

AEMFCs operate by reducing oxygen at the cathode to produce OH−, which gets transferred to the anode compartment through the anion exchange membrane where it reacts with hydrogen to produce water. [23, 48] The kinetics of these cathodic oxygen reduction reaction (ORR) is what largely determines the overall efficiency of the fuel cell. With studies demonstrating the high instability of platinum-based catalysts in alkaline media,[49] it has become imperative to design non-platinum based electrocatalysts catalysts that are not only durable, but also show efficient catalytic activity in AEMFCs. Therefore, to further the scale up and commercialization of AEMFC technology, the development of alternative electrocatalysts has become a high research priority.

1.2.1 Oxygen Electroreduction in Alkaline Media

Electrocatalysts should be designed utilized to facilitate the oxygen electroreduction kinetics cathode compartment of fuel cells, which is an important electrochemical reaction that eventually determines the overall performance of a fuel cell. It is desirable to have the O_2 reduction reaction occurring at potentials as close as possible to the reversible electrode potential (thermodynamic electrode potential) with a satisfactory reaction rate. The mechanism of the electrochemical O_2 reduction reaction is quite complicated and involves many intermediates, primarily depending on the natures of the electrode material, catalyst, and electrolyte.

In alkaline media, oxygen electroreduction happens via the direct 4 electron reduction mechanism:

$$O_2 + H_2O + 4e^- \rightarrow 4OH^-, \quad E^\circ = 0.401\ V$$

Or though the indirect 2e- mechanism that generates peroxide radicals:

$$O_2 + H_2O + 2e^- \rightarrow HO_2^- + OH^-, \quad E^\circ = -0.065\ V$$

$$HO_2^- + H_2O + 2e^- \rightarrow 3OH^-, \quad E^\circ = 0.867\ V$$

It has been suggested the mechanism of ORR in alkaline media usually occurs via two different mechanisms: the inner and outer-sphere electron transfer mechanism. Inner-sphere electron transfer mechanism involves strong chemisorption of molecular O_2 (with or without bond breaking) on oxide free Pt active sites followed by $4e^-$ transfer

$$O_2 \rightarrow O_{2,ads}$$

$$O_{2,ads} + H_2O + 2e^- \rightarrow (HO_2^-)_{ads} + OH^-$$

$$(HO_2^-)_{ads} + H_2O + 2e^- \rightarrow 3OH^-$$

In the outer-sphere electron transfer mechanism, the solvated molecular O_2: cluster $O_2 \cdot (H_2O)_n$ interacts with the surface of the catalyst to form OH_{ads} via hydrogen bonding. Hydrogen bond formation stabilizes the solvated molecular oxygen $O_2 \cdot (H_2O)$ cluster, and promotes an outer-sphere electron transfer to form the superoxide species. In alkaline media, water molecules not only act as solvent but also serve as the source of protons required in ORR, thereby facilitating ORR kinetics.

1.2.2 Pd-based Electrocatalysts for Oxygen Electroreduction in Alkaline Media

Moreover, the flexibility of utilizing non-platinum based cathode catalysts in AEMFCs have expanded the parameter space for the design and development of materials that are highly active in alkaline media. In previous studies, various cathode catalysts such as Ru[50], Ag,[51] and Co[52] have been used instead of Pt for studying ORR in alkaline electrolytes. There has been an increased research activity in ORR electrocatalysis on Pd-based catalysts during the last decade, and the performance of Pd-based catalysts in fuel cell catalysis has been reviewed by many.[53-55] Intensive efforts have been invested towards developing alternatives to Pt/C such as shape or size modified monometallic palladium (Pd) nanoparticles[56-58] Studies have also shown the significantly enhanced performance of Pd-based catalysts towards the electroreduction of oxygen in both acidic and alkaline medias.[54, 56, 59, 60] The improved intrinsic electrochemical activity, catalyst stability and accessibility of Palladium based nanocomposites in comparison to Pt was also demonstrated for oxygen reduction reactions (ORR) in alkaline electrolytes. For example, it was shown that Pd nanoparticles with Pd(1 1 1) facets were more active for ORR in an alkaline solution than in an acidic solution, with comparable activities to Pt/C in the former.[61] Other studies have also focused on Pd-based alloys [62] such as Pd coated Ag[63] and PdNi [64-67]. For example, the specific and mass activities of Pd-Ag/C catalysts were shown to be enhanced by a factor of 3 and 2.5, respectively compared to the Pt/C electrocatalyst for ORR in alkaline media.[63] Moreover, palladium nanoparticles were also shown to be significantly more durable than Pt under

constant load cycling in alkaline media, making them promising cathode materials for AEMFCs. [68]

However, there are still a few limitations regarding the synthesis of monometallic Pd nanoparticles, as most procedures involve multi-step complicated sol-gel techniques that implement the use of organic complexes such as oleylamine, oleic acid as well as other surfactants and stabilizers such as cetyltrimethylammonium bromide (CTAB), which can produce nanoparticles that lack physicochemical homogeneity. Formerly identified impediments accompanying subpar catalytic activity originated from the existence of polymeric surfactants and their chemical bonding to the nanoparticle surface, which made them sensitive to poisoning, ultimately leading to deactivation. Pd nanoparticles that are synthesized using capping agents or stabilizers that can also get adsorbed onto the surface of Pd and reduce its electrochemically accessible surface area or inhibit ionomer-catalyst-fuel interactions in the membrane electrode assembly (MEA) of the fuel cell. Moreover, laboratory used methods for preparing Pd-based catalysts by using surfactants cannot be scaled up for multi-kilogram level due to the complex technological steps involved. Hence, the synthesis and performances of the Pd catalysts still require further improvements.

1.2.3 Catalyst Supports: Graphitized vs. Amorphous Carbon

The choice of support material is vital and highly influential in determining the behavior, performance, longevity and cost effectiveness of the catalyst and the overall fuel cell. In order to better utilize the catalytic nanoparticles, supports should meet certain requirements such: (i) good electrical conductivity for facilitating charge transfer, (ii) a large surface area for better dispersion of nanoparticles deposited on the support (iii) a porous structure that

enables the ionomer and polymer electrolyte membrane to bring the catalyst nanoparticles close to the reactants, (iv) good water handling capability to avoid flooding within the fuel cell stacks, (v) good corrosion resistance and stability in acidic and alkaline media (vi) and durability under load cycling and accelerated stress tests.

At present, to prevent the sintering, Pd nanoparticles are usually dispersed on commercial carbon supports such Vulcan XC-72 (Cabot Corp.) and Ketjen Black (KB EC600JD & KB EC600J, AkzoNobel) or carbonaceous materials such as carbon blacks, carbon nanofibers, etc. These are the most extensively used materials for catalytic support due to their high surface areas and conductivities. One of the most attractive features of utilizing porous carbon materials is that they enable the nanoparticles to interact with the reactants not only at the surfaces but also through their porous frameworks. However, the majority of these carbon supports have a substantial amorphous component, which might lead to corrosion, although studies of carbon corrosion is limited. Moreover, commercial carbon blacks such as Vulcan XC 72R are known to contain sulfur impurities (which can negatively affect deposited Pd nanoparticles). Thus, the development of alternative supports is therefore of paramount importance in terms of nanoparticle distribution and electrochemical stability.

Consequently, several attempts have been made to fabricate non-amorphous supports such as silicon carbide, ceramic materials (oxides and carbides) and graphitic supports for the dispersion of palladium and other platinum group metal nanoparticles to facilitate better utilization of dispersed noble metal nanoparticles for various electrochemical reactions [69, 70]. Among these, graphitized supports seem to have attracted the most interest due to several obvious advantages over other porous carbon materials from their extraordinary physical

and chemical properties such as high surface areas (up to 2630 m^2 g^{-1} arising from its 2D morphology estimated theoretically), mechanical and chemical stability as well as excellent electrical conductivity corrosion resistivity [71-76], making them ideal as catalyst supports [73]. Graphitic forms of carbon such as graphene nanosheets [77, 78], carbon nanotubes [79-81], multi-walled carbon nanotubes (MWCNTs), graphite nanofibers, graphene oxides etc. [58, 73, 82, 83], and fullerenes [84] are just a few of the examples. Moreover, graphene-like supports also facilitate the better utilization of noble metal nanoparticles such as Pd for various electrochemical reactions.[58, 73, 82] Moreover, the ability to tailor graphene's characteristics and tuning its electronic structure by introducing foreign atoms and dopants make graphitized materials suitable as active supports for other nanoparticles (Pd, Pt etc.) or transition metals (Fe, Ni, Co.)[73, 85-88] Dopants such as sulfur, boron and nitrogen have been routinely used for (i) modifying the electronic properties of graphene, can lead to improved conductivities, facilitated charge transfer and nanoparticle stability.[89-92]

1.2.4 Nitrogen Doped Graphitized Supports

The nature of graphene also enables it to be doped with other heteroatoms such as sulfur,[89, 93], boron[90], and nitrogen [94-96] modifying its electronic properties.[97, 98] Among the various dopants, nitrogen has been the most widely investigated due the its ability to interact with the sp^2 carbons via π-πinteractions and donating electrons into graphene's matrix, which results in result in tunable chemical and physical properties due to conjugation between the nitrogen lone-pair electrons and the graphene π-system.[95, 99-101] According to the results obtained from numerous high resolution XPS experiments, the nitrogen species that have been detected in pyrolyzed electrocatalysts are: (i) pyridinic nitrogen, (ii) pyrrolic

nitrogen, (iii) pyridine-N-oxide, (iv) quaternary nitrogen, and (v) graphitic-N).[95, 101, 102] Nitrogen dopants can also activate the neighboring carbon atoms in the C-N_x functionalized moieties for oxygen adsorption, which can be further reduced via other catalytically active sites such as Pt, Fe or Pd. [103-105] Nitrogen moieties can also be a part of the active site center for ORR itself,[106-109] and a strong correlation between nitrogen dopant level and oxygen reduction currents has been observed.[110]As a results of nitrogen incorporation into the carbons matrix, graphitized supports can get highly activated and facilitate ORR kinetics.

It has also been reported that nitrogen doping also prevents the agglomeration and improves the distribution as well as stability of metal nanoparticles on carbon support and highly durable by introducing more binding sites to the carbon surface that anchor metal precursor or metal nanoparticles. [103, 111, 112] The incorporation of N atoms within graphene sheets could also activate the neighboring carbon atoms in the C-N_x functionalized moieties for oxygen adsorption, and contribute more active sites for catalytic reactions along facilitate ORR on Pd. Consequently, nitrogen doped graphitized materials have been regarded as one very promising metal catalyst support.

1.2.5 Limitations with Fabricating Porous Nitrogen Doped Graphitized Supports

While three dimensional (3D) graphitized carbonaceous materials have gained considerable interest as promising supports for fuel cell electrocatalysts and other energy conversion devices,[113-115] the controlled synthesis of 3D graphene nanostructures and their integration into the electrodes of fuel cells remains a challenging task. Most graphene-like supports or nitrogen doped graphenes in literature supports have been prepared by nitrogen plasma

treatment[101], chemical vapor deposition (CVD)[116], pyrolysis of nitrogen-containing precursors[117] and other microwave assisted [118] or electrochemical exfoliation techniques[119]. While these methods produce high quality graphene sheets and are highly effective in terms of doping. These methods however, tend to yield nitrogen-doped graphene materials in low or un-scalable quantities with un-controlled morphological properties.

On the other hand, highly graphitic materials usually have a low surface areas mainly attributable to the strong aggregation tendency of graphene or restacking of graphene sheets, which not only hinder the dispersion of nanoparticles deposited on them, but also its mass transport capabilities.[120, 121] Hence, developing porous heteroatom doped graphene materials[122] doped with more tailored morphologies[123, 124] have gained interest since they provide a favorable framework for electron transport and enable the nanoparticles to interact with the reactants not only at the surfaces but also through their porous structure for carbon-based ORR catalysts.

The task of rationally designing graphitized materials with tunable pore structures and controlled morphologies has become increasingly imperative due to the advantages of both graphite and graphene to be combined, such good mechanical strength and high surface areas. However, fuel cell electrocatalysts and their support structures are complex heterogeneous materials, and the underlying relationship between catalytic activity, surface morphology and physical-chemical properties of graphene-like supports are not well characterized. Although there have been several studies on investigating the intrinsic properties of graphene and nitrogen-doped graphene itself, the controlled synthesis of 3D graphene nanostructures with abundant remains a challenging task. As a result, in spite of the large body of literature concerning the structure dependent activity of Pd/Graphene

nanocomposites[56, 58, 104], the knowledge related to understanding the influence of the graphitic supports morphology on ORR performances, and the structure-to-property correlation between the porosity of the three-dimensional graphene supports and ORR kinetics in alkaline media is still requires further investigating. Additionally, the role played by nitrogen moieties in nitrogen doped graphene supports towards influencing the electrochemical performance of the materials is not abundantly clear, especially due to the broad range in binding energies values reported for different types of nitrogen moieties. Due to these uncertainties, the derivation of detailed structure-to-property relationships remains difficult.

Moreover, the performance of electrocatalysts not only depend on its intrinsic activity but also on the fuel mass transport mechanisms within the supports in the membrane electrode assembly (MEA). The density of the triple-phase boundary (TPB) structure in the membrane layer, where reactions are taking place in the electrolyte, gaseous fuel, and electrode interface, along with the intrinsic activities of the catalysts can play an important role in determining the overall performance in the fuel cell. One of the other limitations of utilizing graphitized supports in MEAs would be the inevitable aggregation hindering ionic accessibility, and there is little information of how graphitized supports perform in AEMFCs. Moreover, majority of the AEMFCs studies have primarily focused on optimizing commercial anion exchange membranes using platinum as one or both electrodes.[125] Although Pd-based catalysts have been investigated in direct liquid fuel cells such as Direct Ethanol Fuel Cells, Direct Formic Acid Fuel Cells and others, [126] there are only a limited number of studies that have investigated the performance of Pd-based electrocatalysts in H_2/O_2 fed AEMFCs, requiring relatively high loadings of 1.5 mg_{Pd} cm^{-2} and need alloying

with other active metals such as Ni, Ru.[34, 127] Hence, its increasingly important to demonstrate that three dimensional graphitized supports can be not only be designed, but can also utilized as supports for monometallic Pd nanoparticles in AEMFCs.

1.3 Research Objectives

The aim of this research project was to design highly electrocatalytically active palladium-nitrogen-graphene nanocomposites for catalyzing electrochemical reduction of oxygen in Anion Exchange Membrane Fuel Cells. In particular, homogeneous palladium nanoparticles were synthesized using a surfactant free method and deposited on spatially arranged three-dimensional nitrogen doped graphene nanosheets (N/3D-Graphene) both fabricated using scalable and cost effective processes. A comparative assessment on the relatively unexplored effect of surface functionalization, morphology, and graphitization and electronic modification of N-doped/3D-Graphene nanosheets towards modifying and enhancing the electrochemical properties of Pd nanoparticles in the synthesized nanocomposites was thoroughly investigated, according to the following objectives:

1: Design porous, high-surface-area, 3D-Graphene nanosheets (3D-GNS) with a hierarchically structured three-dimensional morphology using silica based sacrificial templates and catalyzing the supports with palladium nanoparticles using a surfactant-free method.

2: Investigate the effects of physicochemical properties of the chemically modified 3D-Graphene support on electrochemical performance of the Pd nanoparticles using various surface characterization and potentiodynamic techniques.

3: Tailor the porosity of the 3D-GNS supports using different sized silica templates, and investigate the effect of support morphology in modifying ORR performance

4: Doping 3D-Graphene nanosheets with nitrogen and investigating the nature of these moieties and their abundances enhancing oxygen electroreduction kinetics.

5: Demonstrate the performance of the catalysts in optimized MEA fabricated AEM fuel cell.

In particular, hierarchically structured graphene nanosheets as support materials were designed with a controlled three dimensional morphologies (3D-GNS). The functionalization and chemical structure of the of the 3D-Graphene nanosheets supports were modified using chemical reduction or thermal pyrolysis. Palladium nanoparticles were then synthesized using the surfactant free Soft Alcohol Reduction method, and then deposited on the chemically modified supports to analyze if the surface chemical properties of the 3D-Graphene sheets had an effect on the size and dispersion of the Pd nanoparticles. The morphology of the functionally optimized 3D-GNS supports were then tailored using different sized amorphous silica templates. With the morphological, physical and chemical characteristics optimized, the 3D-GNS supports were then further activated and enhanced with nitrogen doping under high temperatures. The nitrogen doped 3D-Graphene nanocomposites (N/3D-GNS) were then utilized as enhanced activated supports for Palladium nanoparticles, to study the effect of nitrogen doping and the role played by nitrogen moieties on enhancing ORR performance. In order to form a comparative analysis, Pd nanoparticles synthesized by SARM were also loaded onto commercial carbon Vulcan (XC-72R) and 2D-Graphene nanosheets. The surface areas, chemical composition and

structural properties of these supports were characterized using various types of surface analysis and spectroscopic techniques. The effect of support's physical-chemical properties on the electrochemical performance of the as-prepared catalysts was studied using potentiostatic and potentiodynamic methods in corroboration with the surface analysis techniques in order to form structure-to-performance correlations of the as-prepared catalysts. The ORR activity (mass activity, Kouteky-Levich analysis, Tafel plots) and electrochemically active surface area Pd nanocomposites, as well we overall performance will be determined using a rotating ring disc electrodes. The Pd/Graphene composite materials were then integrated into a catalyst coated membrane, optimized for their performance (assembly, activation, electrode fabrication) and analyzed for their performance in H_2/O_2 fed Anion Exchange Membrane Fuel Cell (AEMFC).

The concepts introduced and tested in this research, as well as the results obtained, provides a synthetic procedure for constructing hierarchically structure nanocomposite materials, but also analyzes how modifying the morphology and chemistry of graphitized supports can play a key role in facilitating electrochemical reactions such as oxygen electroreduction. This results in this study further highlights the importance of rationally designing electrocatalysts for high-performance energy conversion devices such as AEMFCs and other energy conversion and storage applications such as super capacitors, direct ethanol fuel cells. etc.

Chapter 2

Methods: Fabrication, Characterization, Electrochemical Activity and Fuel Cell Performance

2.1 Fabrication of Morphologically and Chemically Modified 3D-Graphene Nanosheets

2.1.1 Synthesis of Graphene oxide

Synthesis of 3D-GNS began with the preparation of graphene oxide (GO_x) nanopallets were by the initial adoption of the modified Hummers Method [128] where graphite flakes are intercalated and oxidized to produce Graphene Oxide (using potassium permanganate, sulphuric acid and hydrogen peroxide. The synthesized GOx was washed with DI water in a centrifuge operating at 3500 RPM twice and fully exfoliated in a water solution using a high power ultrasonic probe (600 kJ were delivered to 10g of GOx in 1L of DI water for 2 hours).

2.1.2 Sacrificial Templating for Varying Morphology

In order to assess the role played by the sacrificial template in modifying 3D-graphenes porosity, sacrificial templates of two different sizes were infused into the exfoliated GO_x, according to the Sacrificial Support Method[38, 129, 130]. Commercially obtained amorphous fumed silica sacrificial templates: i) smaller sized EH5 (Cab-O-Sil® EH5, surface area ~400 $m^2\ g^{-1}$, agglomerate size 0.14 µm) and (i) larger sized commercially obtained silica template (Cab-O-Sil® L90 surface area ~90 $m^2\ g^{-1}$, agglomerate size 0.22 µm) was infused into the GO_x mixture following a 2:1 weight ratio of silica:GO_x via further high energy ultrasonic

treatment. The morphologically modified 3D-GNS supports were labelled as **3D-GNS-L90** and **3D-GNS-EH5.**

2.1.3 Reduction Treatments for Varying Chemistry

In order to assess the role of 3D-Graphenes surface chemistry on nanoparticle distribution and ORR performance, two reduction treatments were employed. **(**a) Thermal Reduction**:** A batch of GO_x-EH5 exfoliated mixture was dried in an oven operating at T=85°C overnight, ball-milled at 400 RPM for 15 min and subjected to thermal reduction in 7at.% H_2 (flow rate = 100 ccm) at T = 800°C for 1 h; (b) Chemical Reduction: 40wt.% Hydrazine Hydrate (N_2H_4*xH_2O) was added drop wise to another batch of continuously stirred mixture of GO_x-EH5 at 80°C for 2 hours, dried and ball-milled to powder overnight at T= 85°C. The chemically and thermally reduced 3D-GNS supports are labelled as **3D-GNS-N_2H_4** and **3D-GNS-H_2.**

2.1.4 Etching of Sacrificial Silica Templates

The resulting batches of dried powder obtained from morphologically modified samples in 2.1.2 and thermally and chemically reduced samples in 2.1.3 were then leached with 25wt.% HF overnight in order to remove the sacrificial template. The black suspension was then washed by centrifugation to a neutral pH and dried overnight at T=85°C.

2.2 Synthesis of 2D-Graphene

As a control experiment, graphene nanosheets without the incorporation of a sacrificial template were also synthesized using a similar to mentioned above procedure. In this method, a batch of sonicated and exfoliated GOx suspension was dried overnight in an oven

operating at T = 85□C, ground to powder using a mortar and pestle and then reduced using methods described in 2.1.2 and labeled as **2D-GNS.**

2.3 Synthesis of Nitrogen Doped 3D-Graphene

The 3D-Graphene nanosheets were divided into three batches and doped with nitrogen using 10 at% NH3 (flow rate 100 cc min^{-1}, 20 deg min^{-1} temperature ramp rate) for 2 hours at T= 650°C, 850°C and 1050°C, and then allowed to cool down to room temperature. The subsequent pyrolyzed nitrogen doped graphene samples were labelled as **N/3D-GNS-650, N/3D-GNS-850 and N/3D-GNS-1050** respectively.

2.4 Palladium Deposition using Soft Alcohol Reduction Method (SARM)

Palladium nanoparticles were then deposited on GNS supports fabricated in section 2.1-2.5 using the surfactant-free Soft Alcohol Reduction Method,(51) where a calculated amount (based on 30 wt% Pd in final catalyst) of the precursor Pd(NO3)2•xH2O was reduced to metallic Pd and deposited on the surface of the 3D-GNS (L90 and EH5) supports using a 1:1 ratio of de-ionized water : ethanol solution via ultrasonic treatment. For sake of comparison, Pd nanoparticles were also deposited on Vulcan XC-72R using SARM.

2.5 Physical and Chemical Characterization of the Synthesized Nanocomposites

The morphology of the synthesized materials and size of the Pd nanoparticles was determined by Scanning Electron Microscopy (SEM, Hitachi S-5200) and Transmission Electron Microscopy (TEM, JEOL 2010 instrument with an accelerating voltage of 200 keV). The structure of the prepared catalysts was obtained by recording their X-ray diffraction (XRD) patterns on thee Rigaku Smartlab diffractometer with Bragg-Brentano focusing geometry and a Cu anode operating at 40 kV and 40 mA. The detector used was

the Rigaku D/teX Ultra 250 1D silicon strip detector with a K-β incident beam monochromator. The angle 2θ was varied between 5 and 145° with a step width of 2° min−1. The average crystallite size of the Pd nanoparticles was determined using Williamson-Hall (W-H) analysis and Scherrer's equation: $D = k\lambda/\beta\cos\theta$, where D is the average diameter of the nanoparticles (nm), K is the Scherrer constant (0.89), λ is the X-ray wavelength (0.154056 nm), β is the corresponding full width at half maximum of the diffraction peak and θ is Bragg's diffraction angle. Surface areas of the modified 3D-GNS supports were measured by N_2-sorption (Brunauer–Emmett–Teller method, BET) using a Micrometrics 2360 Gemini Analyzer. Surface areas were measured by the N_2-Brunauer–Emmett–Teller (BET) method using a Micromeritics 2360 Gemini Analyzer The pore size distributions of the porous carbons were analyzed using the Barrett-Joyner-Halenda (BJH) method. The composition as well as the chemical properties of chemically and thermally modified 3D-Graphene supports was analyzed using Energy-dispersive X-ray spectroscopy (EDS) and Raman Spectroscopy. Surface composition analysis was performed using Kratos Axis DLD Ultra X-ray photoelectron spectrometer. A monochromatic K-alpha source, operating at 150W, was used without the charge neutralization. Pass energies of 20 eV and 80 eV were used for high resolution and survey spectra, respectively. High resolution N 1s, C 1s and O 1s spectra were acquired from three areas per sample. Low resolution survey scans were acquired at 80 eV pass energy for 2 minutes and high resolution Pd 3d and C 1s spectra were acquired at pass energy for 4 minutes Data analysis and quantification was done on CasaXPS software. High resolution C 1s spectrum was fitted using asymmetric line shape for sp2 graphitic carbon at 284.4 eV and symmetric Gaussian-Lorentzian (30) line shape for the rest of peaks.

2.6 Electrochemical Characterization

Electrochemical studies of the synthesized materials was performed using the Pine Instrument Company electrochemical analysis system in a three-electrode cell containing 0.1 M NaOH electrolyte saturated with N_2 and O_2 at 25°C. A Pt wire counter-electrode and a Hg/HgO reference electrode was used. The current densities were normalized to the geometric area of the electrode and potentials in the manuscript are referred to the reversible hydrogen electrode (RHE). The working electrodes were prepared by mixing 5 mg of the as-prepared electrocatalyst with 925 μL of de-ionized water and isopropyl alcohol (4:1) mixture, and 75 μL of Nafion® (0.5 wt. % solution, DuPont). The ink was sonicated before 10 μL was applied onto a glassy carbon disk with a catalyst loading of 0.2 mg cm^{-2}.

The electrochemically accessible surface area (ECSA) of Pd/3D-Graphene and Pd/Vulcan catalysts were determined by implementing two widely accepted methods:

1) charge integration of the Pd oxide reduction peak between 0.8 and 0.6 V vs. RHE, according to the formula: $EASA = Q/(m \cdot C)$

where Q is the charge of Pd-oxide reduction, m is the amount of Pd loaded onto the electrode (mg), and C is the theoretical charge of Pd oxide monolayer reduction,424 μC cm^{-2}

2) CO-stripping coulometry were performed in 0.1 M H_2SO_4 solution, prepared using high-purity reagents (Merck, Suprapur®) and thermo-stated at 25°C. A carbon plate and a mercury sulphate electrode was used as counter and reference electrodes, respectively. To determine the ECSA value, the working electrode was polarized at 0.15 V vs. RHE while carbon monoxide was introduced in the solution for 6 minutes, followed by removal of the

CO excess by argon gas for 39 minutes. Then, a cyclic-voltammetry was recorded at 20 mV s^{-1} between 0.1 and 1.33 V vs. RHE.

In alkaline media, the oxygen reduction reaction pathway proceeds to the efficient 4 electron (e-) process where O_2 is completely reduced to OH-,

$$O_2 + 2H_2O + 4e^- \rightarrow 4OH^- \quad [1]$$

versus the two-by-two electron (2x2e-) mechanism where O2 is reduced to peroxide intermediates according to the following equations:

$$O_2 + H_2O + 2e^- \rightarrow HO_2^- + OH^- \quad [2]$$

$$H_2O + HO_2^- + 2e^- \rightarrow 3OH^- \quad [3]$$

The HO2- detected on the ring of the rotating ring disc electrode (RRDE) can be used to calculate the % HO2- yield and the no. of electrons transferred (ne-) to and deduce the ORR mechanism according to the following equation:

$$H_2O_2\ (\%) = 200 * \frac{J_R/N}{J_R/N - J_D} \quad [5]$$

$$n = \frac{-4\,J_D}{J_R/N - J_D} \quad [6]$$

Where J_R and J_D are the disk and ring current densities, respectively, and N is the ring collection efficiency (0.40). The reaction kinetics were further analyzed by using rotating-disk electrode (RDE) voltammetry. By using RDE measurements carried out at different rotation rates (600-3600 RPM), the overall number of the electron transferred (n) per O_2 molecule was calculated using the Koutecky-Levich equation:

$$\frac{1}{J} = \frac{1}{J_k} + \frac{1}{J_D} = -\frac{1}{nFkC_{O_2}^b} - \frac{1}{0.62nFD_{O_2}^{2/3}\nu^{-1/6}C_{O_2}^b\omega^{1/2}} \quad [7]$$

where J is the measured current density, J_K is the kinetic current density, J_D is the diffusion-limited current density, n is the no. of electrons transferred, k is the rate of reaction for ORR, F is the Faraday constant (96,485 C mol^{-1}), ω is the rotation rate (rad s^{-1}), $C_{O_2}^b$ is the concentration of O_2 in the bulk solution (1.2×10^{-6} mol cm^{-3}), $D_{O_2}^{2/3}$ is the diffusion coefficient of O_2 (1.9×10^{-5} cm^2 s^{-1}) and *v* is the kinematic viscosity of the electrolyte (0.01 cm^2 s^{-1}).

Chapter 3

The Effect of Graphene's Surface Chemistry on Oxygen Electroreduction

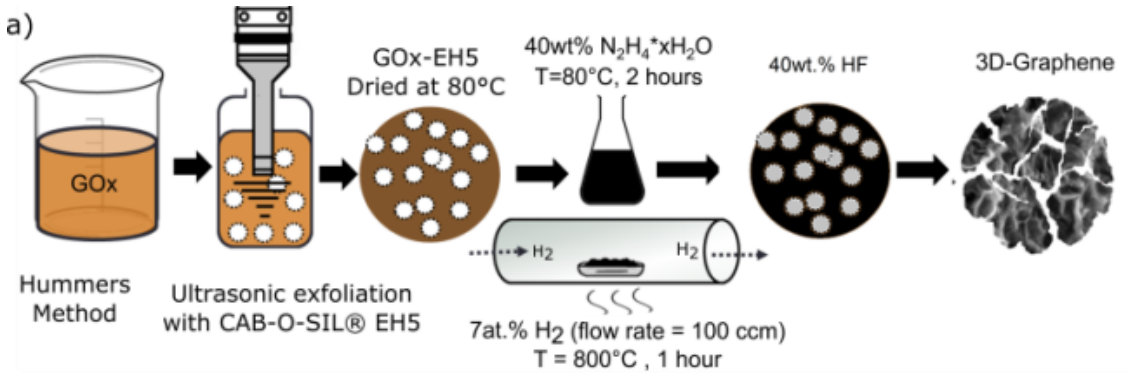

Figure 3. Schematic illustration of chemically and thermally reduced 3D-GNS supports fabricated using the Sacrificial Support Method.

3.1 Morphology of Chemically and Thermally Reduced 3D-GNS

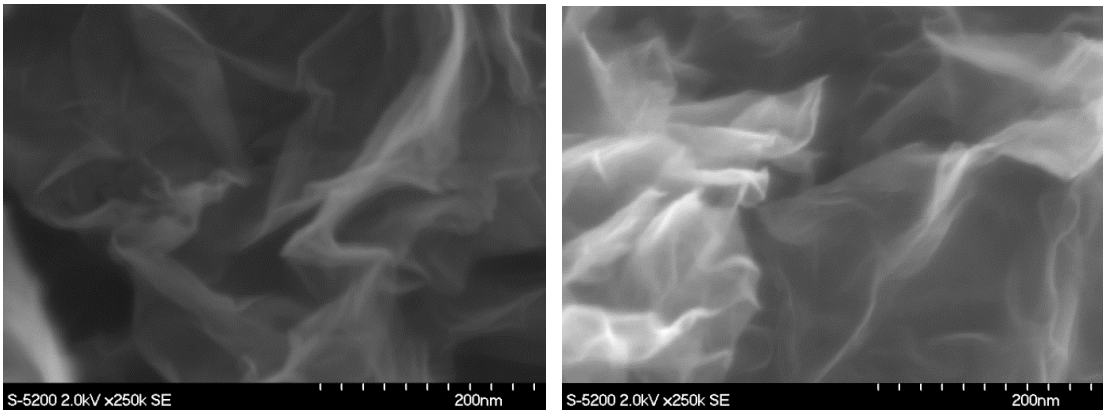

Figure 4. SEM images of chemically reduced (3D-GNS-N_2H_4, left) and thermally reduced (3D-GNS-H_2, right) 3D-Graphene nanosheets modified with the EH5 sacrificial template.

Fig. 3 illustrates the procedure for fabricating highly porous 3D-GNS supports with using the Sacrificial Support Method (SSM). [99, 129, 131] The surface chemistries of the 3D-GNS supports were modified during chemical (3D-GNS-N_2H_4) and thermal reduction treatments (3D-GNS-H_2) as described in the methods section, 2.1.3. The sacrificial template – (CAB-

O-SIL® EH5) – was utilized during both the reduction treatments. A flake-shaped 3-dimensional morphology of the graphene nanosheets can be observed, which was most likely formed due to the network of porous channeled introduced within its matrix through acid etching of the sacrificial EH5 silica template. This was also confirmed by comparing highly magnified SEM micrographs, which revealed that both the thermally and chemically reduced EH5 modified 3D-GNS supports had almost identical morphologies, allowing us to make comparison of the 3D-GNS support's chemical properties. Since the supports were synthesized using the same sacrificial EH5 silica template (SSM), both the chemically (3D-GNS-N_2H_4) and thermally reduced (3D-GNS-H_2) 3D-Graphene had similar Brunauer–Emmett–Teller (BET) surface area of 400-500 m^2 g^{-1}.

3.2 Surface Chemistry of Chemically and Thermally Reduced 3D-GNS

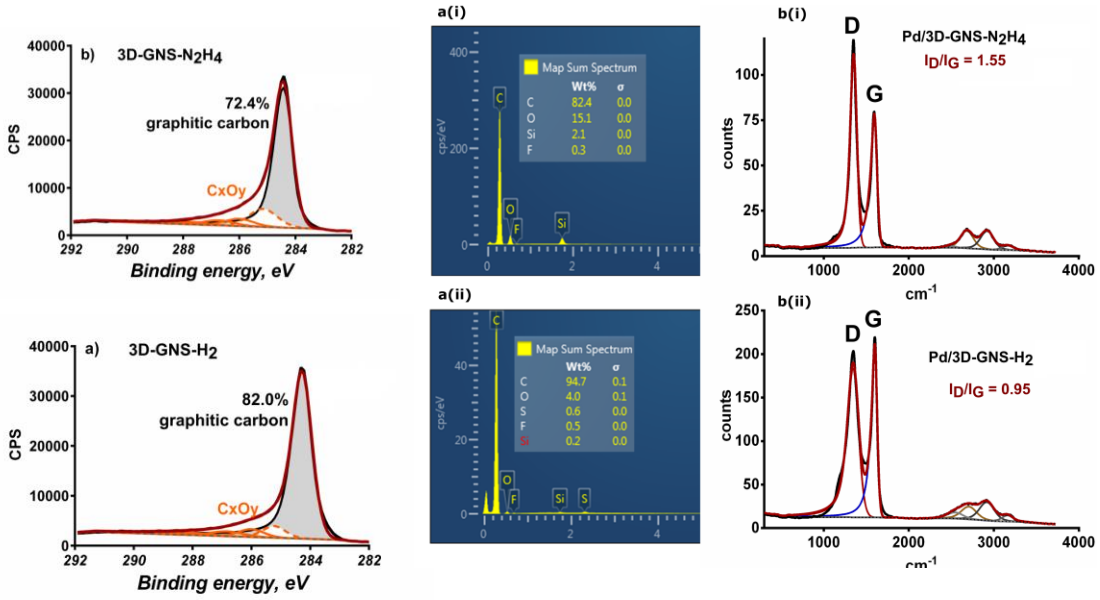

Figure 5. C1s XPS, EDS Analysis, and Raman Spectra of (i) chemically (3D-GNS-N2H4) and (ii) thermally (3D-GNS-H2) reduced 3D-Graphene Nanosheets

However, although the morphologies were similar - the surface compositions of the chemically and thermally reduced 3D-GNS supports varied in terms functionalization. The chemical nature of the 3D-GNS supports was determined using high resolution C 1s X-ray Photoelectron Spectroscopy. As it can be seen from Fig. 5a, thermally reduced 3D-GNS-H_2 supports had a higher percentage of graphitic carbon (82%) and smaller amount of surface oxide (C_xO_y) peaks detected, while chemically reduced 3D-GNS-N_2H_4 supports had a lower percentage of graphitic carbon (73%, Fig. 5b) and higher amount of oxygenated species. These results show that the thermally reduced 3D-GNS-H_2 supports had a higher degree of graphitization, which could be due to the thermal decomposition of surface functional groups at high pyrolysis temperatures (7 at% H_2, 800^{o}C).

Using EDS analysis, it was found that the chemically reduced 3D-Graphene nanosheets (3D-GNS-N_2H_4_EH5) had a higher oxygen content (~15 wt.%, Fig. 5a.i.) in comparison to thermally reduced 3D-Graphene nanosheets (3D-GNS-N_2H_4_EH5), which had a significantly lower oxygen content (~4.0 wt.%, Fig. 5a.ii) The presence of oxygenated species could be due the presence of functionalized groups such as C-OH or C-OOH present on the surface. These results also suggest 7at.% H_2 to be significantly more effective as a reducing agent in comparison to hydrazine hydrate (N_2H_4*H_2O).

Raman spectra was used to examine the structural changes induced into the C-C network of the 3D-Graphene supports due to chemical and thermal reduction treatments. The characteristic resonances observed around 1580 cm^{-1} and 1350 cm^{-1} in Fig. 5b9i) and b(ii) correspond to in-plane vibrational mode involving sp^2 hybridized carbon atoms that comprise of graphene sheets (G band) and defects (D band) in the carbon network, respectively. The ratio of the D to G band peak intensities (I_D/I_G) from the Raman Spectra

was used to characterize the level of disorder in the 3D-Graphene supports. It was found that the chemically reduced graphene support had an I_D/I_G ratio of 1.55 (Fig. 5b.i), whereas the thermally 3D-Graphene supports had an I_D/I_G ratio of 0.95 (Fig. 5b.ii), corresponding to a lower level of disorder.

3.3 Effect of Surface Chemistry on Palladium Nanoparticle size and distribution

For investigating the effect of 3D-GNS surface chemistry on nanoparticle size and distribution, - and eventually towards O_2 electroreduction - Pd nanoparticles of the same loading (30 wt%) were deposited on both the chemically and thermally reduced 3D-GNS supports using the Soft Alcohol Reduction Method (SARM). SARM enables the deposition of Pd nanoparticles on 3D-GNS supports by reducing the Pd precursor [$Pd(NO_3)_2{\cdot}2H_2O$] to metallic Pd using simple reducing solvents such as ethanol. For sake of comparison, Pd nanoparticles were also deposited on commercial carbon black Vulcan (XC-72R) using the same method (SARM). A powder X-ray diffraction (XRD) analysis of Pd/3D-GNS-H_2, Pd/3D-GNS-N_2H_4 and Pd/Vulcan nanocomposites was carried out for obtaining information about the crystallographic structure of these Pd nanoparticles. Fig. 6 exhibits the X-ray diffraction patterns of Pd nanoparticles deposited on the (i) thermally reduced (Pd/3D-GNS-H_2) and (ii) chemically (Pd/3D-GNS-N_2H_4) graphene nanosheets sheets, as well as Pd on commercial carbon support, Pd/Vulcan (iii). The first peak at 26.1° refers to crystalline graphene. The observed intense peaks (indicated by asterisks) at 2θ =40, 46, 68, 82 and 87 deg. corresponds to the [111], [200], [220], [311] and [222] crystalline face centered cubic (FCC) structure of palladium, respectively. The average crystallite size and lattice strains of

the Pd nanoparticles were evaluated using Williamson-Hall (W-H) analysis and Scherrer's equation: $D = \frac{k\lambda}{\beta cos\theta}$

where D is the average diameter of the nanoparticles (nm), K is the Scherrer constant (0.89), λ is the X-ray wavelength (0.154056 nm), β is the corresponding full width at half maximum of the diffraction peak and θ is Bragg's diffraction angle.

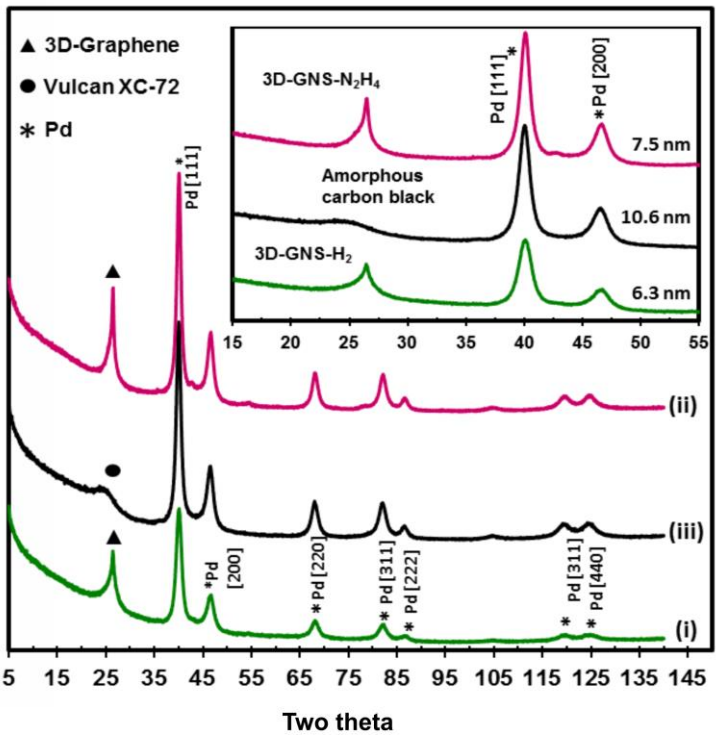

Figure 6. X-ray Diffractograms and SEM micrographs of Pd nanoparticles deposited on thermally (Pd/3D-GNS-H2) and (ii) chemically (Pd/3D-GNS-N2H4) reduced 3D-Graphene nanosheets using SARM. (iii) Pd nanoparticles deposited on commercial carbon black Vulcan (XC-72R)

Using Scherrer's equation, the average crystallite size of the Pd nanoparticles (marked with asterisk,*) in Fig. 6 was estimated to be ca. 6.3, 7.5 and 10.6 nm for Pd/3D-GNS-H_2, Pd/3D-GNS-N_2H_4 and Pd/Vulcan, respectively. The XRD patterns in Fig. 6 demonstrate that all the Pd nanoparticles deposited on the three different supports have a face-centered cubic (FCC) structure corresponding to the Pd(111) and Pd(200) lattice spacing at 42.5°

and 47.5° respectively, further verifying that SARM essentially yields metallic Pd nanoparticles with the same crystallite structure (FCC). Moreover, the intense peaks detected ca. 27° (Fig. 6i and Fig. 6ii) from carbon point towards the crystalline structure and graphitization of 3D-GNS supports, corroborating the findings from C1s XPS spectra shown in Fig. 6. The broad peak around the same region for Pd/Vulcan (Fig. 6iii) however corresponds to the amorphous nature of the carbon black support (Vulcan XC-72R).

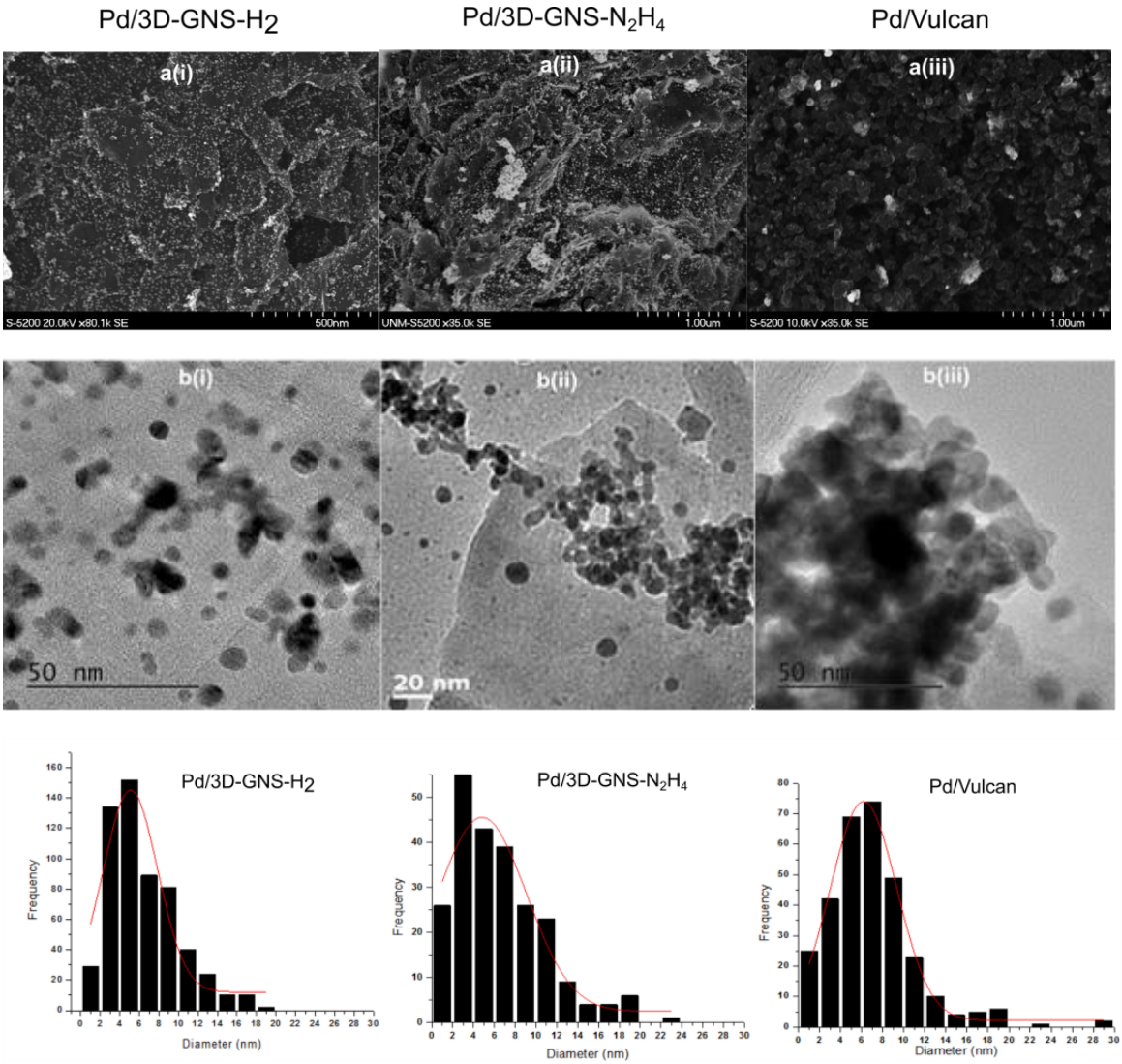

Figure 7. a) SEM, b) TEM and particle size distribution of Pd nanoparticles supported on thermally reduced (i) (3D-GNS-H_2) and chemically reduced (ii) 3D-GNS-N_2H_4 - 3D-Graphene nanosheets; and (i) Vulcan for comparison, deposited using the Soft Alcohol Reduction Method.

Further SEM and TEM analysis of the metal-doped nanocomposites was carried out for obtaining correlations between the physicochemical properties of the support and the size as well as dispersion of the Pd nanoparticles. The SEM and TEM micrographs in Fig. 7b show the existence of quasi-spherical palladium nanoparticles deposited on the three different supports. A statistical TEM particle size distribution analysis revealed that Pd nanoparticles deposited on both the chemically and thermally reduced 3D-GNS supports have an average particle size of 5 nm (Fig. 7). The average crystallite sizes estimated from XRD were slightly higher than the values determined from TEM data, since XRD peak widths of Pd are related to domain sizes estimated from the [111] and [100] facets using the Scherrer's equation, where larger crystallites usually dominate. However, as it can be seen from Fig. 7ai and Fig. 7bi, the Pd nanoparticles were uniformly distributed over the 3D-GNS-H_2 support, whereas the Pd nanoparticles on 3D-GNS-N_2H_4 (Fig. 7aii and Fig 7bii) were slightly agglomerated in certain regions. Since both the Pd/3D-GNS composites were synthesized using the same surfactant-free method (SARM) with a constant Pd precursor loading (30 wt.%), and only the methods of reduction were varied, these differences in distribution can be attributed to the varying surface chemistries of the 3D-GNS supports arising from the two different reduction treatments.

Using a combination of XPS and EDS, the chemically reduced 3D-GNS-N_2H_4 supports were shown to have a higher oxygen content (~15 wt.%, in comparison to thermally reduced 3D-GNS supports (~4.0 wt.%). This higher degree of oxidation of the 3D-GNS support was attributed to the relatively weak reduction power of hydrazine hydrate

($N_2H_4.xH_2O$) in comparison to 7at.% H_2 under thermal pyrolysis.[132] These results have now been further corroborated using XPS, which shows that 3D-GNS-N_2H_4 supports have a higher amount of C_xO_y species (Fig. 5b). These oxygenated functional groups could be playing a role in determining the dispersion Pd nuclei formed during the surfactant-free soft alcohol reduction of the Pd precursor, and the discrepancies of the Pd nanoparticle distribution might be accounted for by the nanoparticle growth dynamics on the supports. Chemically reduced 3D-GNS-N_2H_4 supports were shown to have a higher level of defects using Raman Spectra analysis, indicating a higher presence of surface functional groups. These oxygenated functional groups may serve as the anchoring site for metal ion chelation and the growth of metal nanoparticles. A higher % of these C_xO_y groups present in defected sp^2 matrix of the 3D-GNS-N_2H_4 support can therefore, cause the Pd nanoparticles to aggregate in certain regions, as evidenced by TEM.

Conversely, at high pyrolysis temperatures (800°C), thermally reduced 3D-GNS-H_2 became less defected, with a higher level of C-C sp^2 hybridization - with fewer % of oxygenated functional groups, as evidenced using EDS and XPS analysis, possibly due to the decomposition these at high temperatures (800°C). This synergistic combination of higher degree of graphitization (82%). C-C sp^2 hybridization, and lower number of C_xO_y oxygenated functional groups in thermally reduced 3D-GNS-H_2 supports (Fig. 5a) could be inducing the Pd nanoparticles to disperse evenly on the surface, whereas the lower degree of graphitization (72%) of and higher number of surface functional groups such as C-OOH, C-OH in the chemically reduced 3D-GNS-N_2H_4 supports could be interacting with the Pd nanoparticles and restricting their dispersion. Hence, although the loading (30 wt% Pd),

crystal structure (FCC) and size (~5 nm) of the Pd nanoparticles on both 3D-GNS-H_2 and 3D-GNS-N_2H_4 supports are similar, their dispersions are different.

In contrast, Pd nanoparticles deposited on amorphous carbon black support - Vulcan (XC-72R) - were sporadically distributed on the surface, as evidenced by the higher number of agglomerates observed in Fig 7aiii. These agglomerated nanoclusters can also be observed in the TEM micrographs, (Fig. 7biii) where the nanoparticles are estimated to have an average size of 8 nm, with the occasional presence of even larger ~20 nm particles. However, it should be noted that these agglomerates seem to be formed by individual Pd nanoparticles with the same average particle size of 8 nm. The increased agglomeration could be due to the comparatively low BET surface areas (210 m^2 g^{-1}) and lower degree of graphitization (30-40%) in Vulcan.[133] Moreover, commercial carbon blacks are also usually heavily contaminated with impurities such as sulfur, various surface functional groups and large number of defects - all of which could be affecting the Pd nuclei coalescence and causing the Pd nanoparticles to agglomerate. These results further demonstrate that the chemistry as well as the degree of graphitization in carbonaceous supports can play an important role in modifying the size and dispersion of palladium nanoparticles.

3.4 Effect of Surface Chemistry on Electrochemically Accessible Surface Area of Pd Nanoparticles

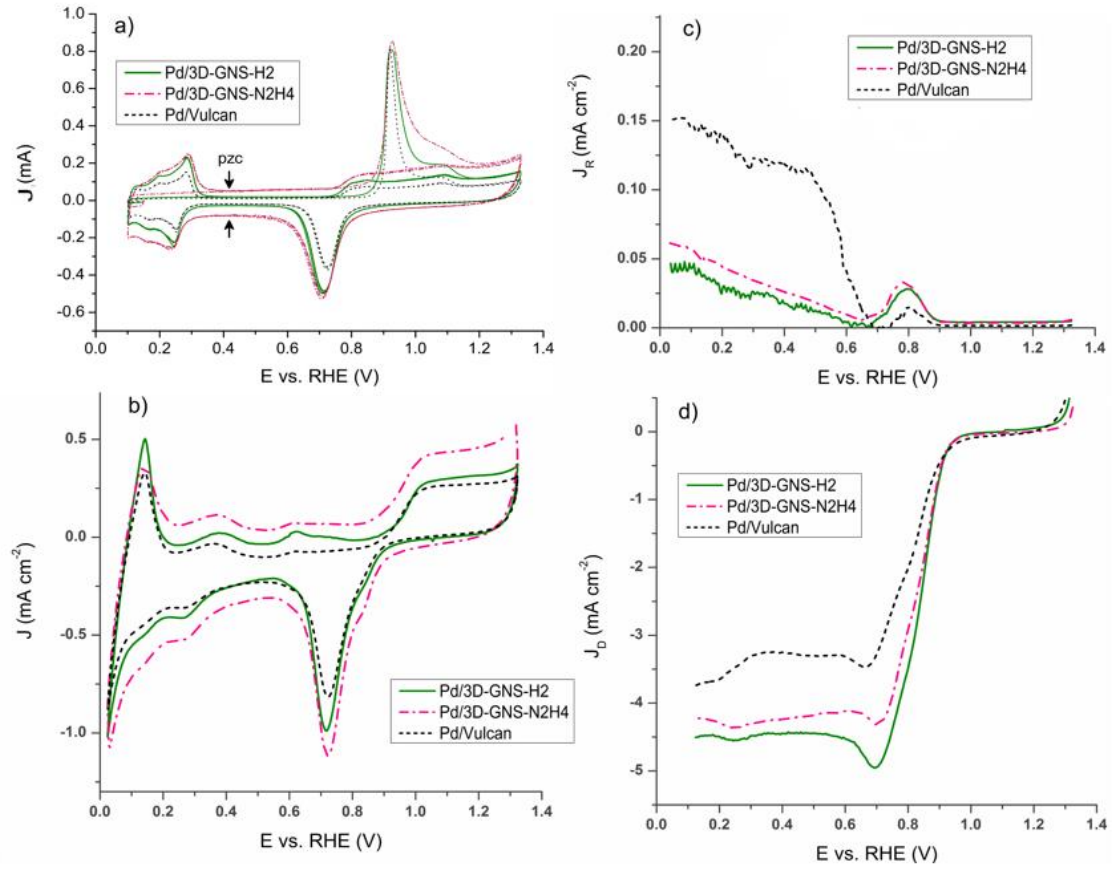

Figure 8. a) CO stripping curves obtained in 0.1 M H_2SO_4 at 25°C and 20 mV s^{-1} c) Cyclic voltammograms recorded in N_2 saturated 0.1 M NaOH at 5 mV s-1 and 1600 RPM; c-d) Dual Electrode Linear Sweep Voltammograms of Pd nanoparticles deposited on 3D-GNS-H_2, 3D-GNS-N_2H_4 and Vulcan

The electrochemically accessible surface area (EASA) of the Pd nanoparticles ($m^2\ g^{-1}$) can be estimated using Eqn. 8:

$$EASA = 6000/\rho_d$$

Where ρ is the density of Palladium (12.02 g cm^{-3}) and d is the size of the nanoparticles (nm). Using Eqn.8 and the size of the Pd nanocrystals obtained using XRD, the electrochemically accessible surface area (EASA) of the Pd nanoparticles deposited on 3D-GNS-H_2, 3D-GNS-N_2H_4 and commercial Vulcan supports was estimated to be 79.4, 66.7 and 47.2 m^2 g^{-1} respectively (Table 1).

Table 1. Electrochemically Accessible Surface Area (EASA) of Pd nanoparticles deposited on thermally and chemically reduced 3D-Graphene nanosheets as well as Vulcan for comparison.

Catalyst	Crystallite size (nm)	EASA (m^2g^{-1})[a]		
		Theoretical	Pd-Oxide Reduction	CO-stripping
Pd/Vulcan	10.6	47	57	28
Pd/3D-GNS-N_2H_4	7,5	67	68	49
Pd/3D-GNS-H_2	6.3	79	62	40

[a] Electrochemically accessible surface area of the synthesized nanocomposites, expressed per gram of Palladium.

However, further CO-stripping experiments were performed in 0.1 M H_2SO_4 at 25°C using a three-electrode station to determine the *observed* EASA of the Pd nanoparticles, Fig. 8a depicts the CO-stripping voltammograms (current, I vs. potential, E) obtained at 20 mV s^{-1}. The current values obtained around the potential of zero charge (PZC) for each catalyst is directly related to the capacitive current from the supports. The higher capacitive current from the Pd/3D-GNS-N_2H_4 catalyst could be due to the synergistic combination of a higher BET surface area (summarized in Table 1) as well as surface functionalization of the chemically reduced 3D-GNS-N_2H_4 support. By assuming a theoretical charge of 420 μC cm^{-2} for monolayer adsorption of CO, the EASA of the Pd/3D-GNS-H_2, Pd/3D-GNS-N_2H_4

and Pd/Vulcan catalysts were estimated to be ca. 40, 49 and 28 $m^2\ g^{-1}$, respectively (Table 1).

However, Palladium nanoparticles are relatively unstable in acidic media, and also agglomerate - which may explain the lower EASA values observed using CO-stripping. Moreover, oxygen reduction reactions tend to proceed through the outer-sphere electron transfer mechanism involving adsorbed OH_{ads} in alkaline media. Hence, the CO-stripping voltammograms obtained in 0.1 M H_2SO_4 might not be providing an accurate depiction of the actual EASA of the Palladium nanoparticles in alkaline media presented in this paper. Therefore, to account for the differences in pH of the electrolyte, additional cyclic voltammetry (CV) experiments were performed in the N_2 saturated 0.1 M NaOH blank electrolyte for characterizing the EASA of the Pd nanoparticles in alkaline media. Fig. 5b represents CV curves (current density, J vs. potential, E) of Pd/3D-GNS-H_2, Pd/3D-GNS-N_2H_4 and Pd/Vulcan catalysts in the blank electrolyte obtained at a scan rate of 5 mV s^{-1} and 1600 RPM.

In general, the features of the Pd-based nanocomposites in their CV profiles are similar to each other, indicating successful synthesis of chemically homogenous Pd nanoparticles deposited on the three different supports with batch-to-batch reproducibility. Particularly, peaks corresponding to the hydrogen adsorption/desorption between 0.1–0.3 V, and the cathodic peaks between 0.6–0.8 V from reduction of Pd surface oxides (PdO) can be observed. By assuming the value of 424 μC cm^{-2} as charge density associated with the reduction of a monolayer of PdO, the EASA of Pd/Vulcan was estimated to be 57 $m^2\ g^{-1}$ in alkaline media. On the other hand, the EASA considerably increased to 62 $m^2\ g^{-1}$ and 68 $m^2\ g^{-1}$ for Pd/3D-GNS-H_2 and Pd/3D-GNS-N_2H_4 catalysts respectively. As it can be seen

from Table 1, these values are within range of the theoretically estimated EASA values obtained using Eqn.1, and provide a more accurate representation of the *actual* EASA of the Pd nanoparticles in alkaline media. Moreover, the EASA of the Pd-based nanocomposites corroborate the results obtained using TEM (Fig. 7) and XRD (Fig. 6), where the Pd/3D-GNS catalysts are shown to have the highest dispersion and smallest particle and crystallite sizes. Evidence of the poor dispersion of the Pd nanoparticles on Vulcan as observed from TEM and SEM images (Fig. 4aii and Fig 4aiii) are also consistent with its lower EASA in comparison to the Pd/3D-GNS catalysts. These results further demonstrate that the nature of the carbonaceous supports can play an important role in enhancing the EASA of Pd nanoparticles by affecting their particle size distribution as well as dispersion. It should be noted that as per the theoretical estimations, the Pd/3D-GNS-H_2 catalysts should have a higher EASA compared to Pd/3D-GNS-N_2H_4. The discrepancy in estimated and *observed* values for the Pd/3D-GNS catalysts could be arising from the differences in charging current at the double-layer region due to the higher surface functionalization of the chemically reduced 3D-GNS-N_2H_4 support. However, Pd/3D-GNS-H_2 catalysts still have the smallest crystallite size and highest dispersion among all the synthesized nanocomposites, and could be playing a significant role in enhancing ORR activity.

3.5 Electrochemical Activity of Pd Nanoparticles for Oxygen Reduction Reaction

Fig. 8c depicts the linear sweep voltammograms obtained using a RRDE at 1600 RPM and 5 mV s^{-1} for the Pd/3D-GNS-H_2, Pd/3D-GNS-N_2H_4 and Pd/Vulcan catalysts in 0.1M NaOH saturated with O_2 at room temperature. The RRDE voltammograms in Fig. 6 can be divided to three regions, namely (i) diffusion-controlled region (<0.65 V), mixed diffusion-kinetic limitation region (0.65–0.85 V) and Tafel region (>0.85 V). The negligible amount of ring current (J_R) till 0.9 V, indicates the absence of hydrogen peroxide generation. Although, a sudden increase in ring and disc currents (J_D) in the upper kinetic regions between 0.9 and 0.85 V can be observed- which was prominent especially for the Pd/3D-GNS catalysts - due to local depletion of oxygen in the highly surface area templated pores present in the 3D-GNS nanocomposites. While all the Pd-based catalysts had similar onset potentials of ~0.99 V for ORR, there was a positive shift of the half-wave potential ($E_{1/2}$) by almost 50 mV for the Pd/3D-GNS catalysts compared to Pd/Vulcan, demonstrating improvements in the ORR kinetics. However, the O_2 reduction current densities of the Pd/3D-GNS-H_2 (4.5 mA cm^{-2}) and Pd/3D-GNS-N_2H_4 (4.1 mA cm^{-2}) catalysts at average fuel cell operating voltages of 0.6 V were approximately 25% higher than that of the Pd/Vulcan catalyst at the same potential (3.3 mA cm^{-2}).

Since supports with a highly ordered structure (e.g. crystalline) and BET surface areas have better electrical conductivities and porosity, it could explain the higher ORR current densities of Pd/3D-GNS catalyst compared to the Pd/Vulcan. Moreover, among the Pd/3D-GNS catalysts, the Pd/3D-GNS-H_2 catalyst had the highest activity of 4.5 mA cm^{-2}, which can be attributed to (i) the higher degree hybridization corresponding to in-plane vibrational mode involving sp^2 carbon atoms (confirmed using Raman spectroscopy in our previous

studies [132]) facilitating electron charge transfer and (ii) high BET surface area due to the templated porosity facilitating oxygen diffusivity into the graphene matrix. Additionally, the increase in ORR activities of the Pd/3D-GNS-H_2 support can also be due to its smaller average crystallite size of 6.3 nm, compared to Pd/3D-GNS-N_2H_4 (7.5 nm) and Pd/Vulcan (10.6 nm).

3.6 Peroxide Generation and Number of Electrons Transferred

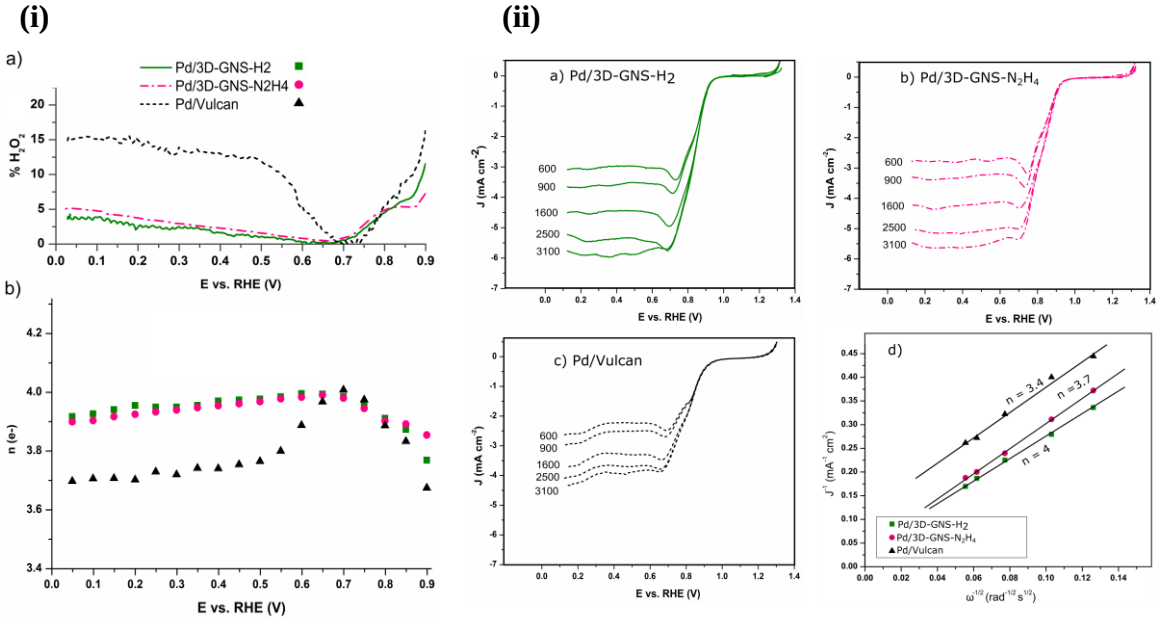

Figure 9. (i) a) Hydrogen peroxide yield (% H_2O_2) and b) number of electrons transferred, n(e-) in O_2 saturated 0.1 M NaOH by Pd/3D-GNS-H_2, Pd/3D-GNS-N_2H_4 and Pd/Vulcan. (ii) RDE voltammetry curves for a) Pd/3D-GNS-H2, b)Pd/3D-GNS-N2H4, c) Pd/Vulcan and d) Koutecky–Levich (K-L) plots and (J^{-1} vs. $\omega^{-1/2}$) for ORR solution obtained from 600-3100 RPM at 5 mV s^{-1} in O_2 saturated 0.1 M NaOH.

The plot in Fig. 9a show the amount of H_2O_2 produced by the catalysts at different potentials during ORR. The onset of H_2O_2 production begins in the kinetic region (0.9 V), but was followed by a significant drop to almost 0% for all the catalysts ca. 0.7 V (n≅4). The negligible H_2O_2 yield on all the Pd-based catalysts indicates that the four-electron (n=4) transfer path is dominant for ORR in the mixed kinetic and mass-transfer regions. With

decreasing potential, there was again a small increase in H_2O_2 yield in the mass transfer controlled regions (< 0.6 V). However, it should be noted that while the H_2O_2 yield increases substantially up to 15% for the Pd/Vulcan catalyst, there is only a marginal increase of H_2O_2 production to a maximum of ~3-4% for the Pd/3D-GNS-H_2 and Pd/3D-Graphene-N_2H_4 catalysts, respectively. The increased in H_2O_2 produced by Pd/Vulcan in the mass transfer controlled region, as compared with those in the mixed kinetic/mass-transfer region can be explained by the H_2O_2 produced on the carbon support itself, as previous studies have shown that carbonaceous supports are active for reducing O_2 to H_2O_2 via the 2x2 electron transfer ORR mechanism in the mass-transfer region.[134, 135]

The peroxide yield of ORR can also involve several other undetermined variables. It is widely accepted that the electrochemical properties of catalytic materials can depend on a combination of factors, such as composition, size and interparticle distance. The interparticle distance – i.e. the degree of agglomeration or dispersion - can be altered by varying the loading of metal nanoparticles on carbonaceous supports, and this agglomeration of nanoparticles can decisively influence the observed catalytic activity. This is known as the "particle proximity effect" hypothesis, which proposes that the catalytic activity, selectivity of carbon-supported Pt nanoparticles towards the ORR and hydrogen peroxide formation [136] is as a function of the Pt catalyst loading and the distance between the catalyst particles. [137] While the composition and size or shape dependent activity of Pd-based catalysts have been investigated extensively, the "proximity" effect is still under debate, mainly due to complications arising with catalyst film formation at higher platinum loadings on Vulcan XC 72R, [138] Other studies have also suggested that the metal loading needs to be increased to achieve the shortest interparticle distance, while avoiding nanoparticle agglomeration in

order to maintain a high surface area. [139] It has also been also shown that the production of H_2O_2 was observed to be higher for potentials below 0.6 V for decreasing interparticle distances. which indicates the important role of a H_2O_2 desorption–readsorption reaction mechanism during the ORR.[140] These findings are also consistent with our results (Fig. 7a), which shows that the H_2O_2 yield of Pd/Vulcan catalysts remained the highest, which could be due to the larger no. agglomerated Pd nanoparticles with a lower EASA being unable to provide enough active sites to readsorb and reduce all of the H_2O_2 being generated to H_2O completely. In contrast, the crystalline nature as well as the higher BET surface area of the Pd/3D-Graphene catalyst seems to have a synergetic effect on the reduced H_2O_2 production. These H_2O_2 yields of 3-4% Pd/3D-GNS catalysts are one the lowest reported in literature among carbon supported metal nanoparticle catalysts for ORR. It should be noted that both the loading of Pd on the 3 different supports (~30wt% Pd) as well as the loading of the catalysts on the glassy carbon electrode (0.2 mg cm^{-2}) was kept constant, which allowed us to exclusively analyze the effect of support on nanoparticle size and distribution under constant loading. These RRDE measurements, in combination with TEM analyses - indicates that the properties of 3D-graphene support not only influence the dispersion or size of the Pd nanoparticles, but also its electrochemical behavior.

Fig. 9b shows that within the potential range of 0.6 to 0.1 V, the Pd/3D-GNS catalysts mainly favored the $4e^-$ ORR pathway. As for Pd/Vulcan, the H_2O_2 yield increases up to 15%, indicating that ORR involved a mixed electron transfer pathway. However, the no. of electrons calculated only estimated for the fixed rotation rate of 1600 RPM. For verifying the mechanistic aspects regarding the *overall* no. of electrons transferred and gaining further insight of the ORR electrochemical process, the reaction kinetics were further

analyzed by using rotating-disk electrode (RDE) voltammetry. By using RDE measurements carried out at different rotation rates (600-3100 RPM), the overall number of the electron transferred (n) per O_2 molecule was calculated using the Koutecky-Levich equation

Fig. 9a shows that the current densities of the synthesized Pd catalysts were linearly dependent on the rotation rates in O_2 saturated 0.1 M NaOH electrolyte. The voltammetric profiles in Fig. 9a-c show that the current densities (J) enhanced with increasing rotation rates (ω, from 600 to 3100 RPM). Furthermore, the plateau and polarization curve obtained for both the Pd/3D-GNS-H_2 and Pd/3D-GNS-N_2H_4 indicates the facilitated electron transfer kinetics in ORR. The Koutecky–Levich (K-L) plots in Fig. 9d (J^{-1} vs. $\omega^{-1/2}$) obtained at different potentials (Fig. S5) from the RDE results in Fig. 9a-c at exhibits a linear dependence and parallelism, indicating first-order ORR kinetics with respect to the concentration of dissolved O_2 in the electrolyte.

The overall number of electrons transferred (n) was calculated to be almost 4 and 3.7 for Pd/3D-GNS-H_2 and Pd/3D-GNS-N_2H_4 from the slopes of the Koutecky-Levich plots, indicating that Pd/3D-GNS catalysts mostly catalyzed the 4-electron reduction reaction of O_2 directly to OH^-. In contrast, the overall no. of electrons transferred were calculated to be n=3.4 for Pd/Vulcan catalyst, which depicts a combination of mixed 2x2e- and $4e^-$ transfer. This also corroborates the higher percentage of H_2O_2 generated by the Pd/Vulcan catalysts, which could be due to the insufficient electroreduction of oxygen by the agglomerated Pd nanoparticles on Vulcan. Conversely, the low H_2O_2 yields and the 4 electron O_2 reduction mechanism can be attributed to the novel 3-dimensional controlled morphology of the 3D-GNS supports designed by the Sacrificial Support Method, where pores and channels are formed inside of the 3D matrix by the sacrificial silica templates

(Cab-O-Sil®, EH5). Forming the pores by the etching templated particles could be providing better accessibility of the Pd nanoparticles to the electrolyte, thereby enhancing the transport of H_2O_2 produced on the surface of the Pd/3D-Graphene catalysts. The templated pores could also be assisting the formation of a triple phase boundary between the electrolyte, oxygen and Pd nanoparticles. Moreover, a rough morphology may also inhibit the expulsion of H_2O_2 from the electrode, where the H_2O_2 could get re-adsorbed on the active sites of Pd which, and can then undergo a further reduction to water via the 2x2 e- pathway if enough Pd active sites are available. Therefore, apart from improving the physical aspects of the Pd nanoparticles, the nanostructured 3D-GNS supports are playing a key role in facilitating the transfer of electrons for ORR as well.

The findings from this study are summarized in Table 2. The results confirm a synergetic promotion of the ORR activity and reduction of peroxide formation using Pd nanoparticles supported on highly graphitized, crystalline and porous few layered 3D-Graphene nanosheets, making them one of the most promising alternative support materials for fuel cell electrocatalysts.

Table 2. Summary of physical and electrochemical properties of Pd nanoparticles supported on the 3D-Graphenen nanosheets supports and commercial Vulcan synthesized in this study.

Catalyst	d (nm) [a]	Graphitic C (%)	EASA (m^2g^{-1}) [b]	$E_{1/2}$ (V) [c]	J (mA cm^{-2}) [d]	H_2O_2 (%) [d]	n [e]
Pd/ Vulcan	10.6	30-40	57	0.81	3.3	7	3.4
Pd/3D-GNS-N_2H_4	7.5	72	68	0.85	4.1	1.1	3.7
Pd/3D-GNS-H_2	6.3	82	62	0.86	4.5	1.1	4

[a] Average crystallite size of Pd nanoparticle obtained using XRD [b] Electrochemically accessible surface area of Pd nanoparticles estimated from charge integration of Pd-Oxide reduction in N_2 saturated 0.1 M NaOH [c] Half wave potential [d] Current densities (J) and Hydrogen Peroxide yield obtained at a scan rate of 5mV s^{-1}, rotating at 1600 RPM at a potential of 0.6 V in O_2 saturated 0.1 M NaOH [e] Number of electrons transferred estimated from slope of Koutekcy-Levich plot.

Chapter 4

Effect of Support Porosity on Oxygen Electroreduction

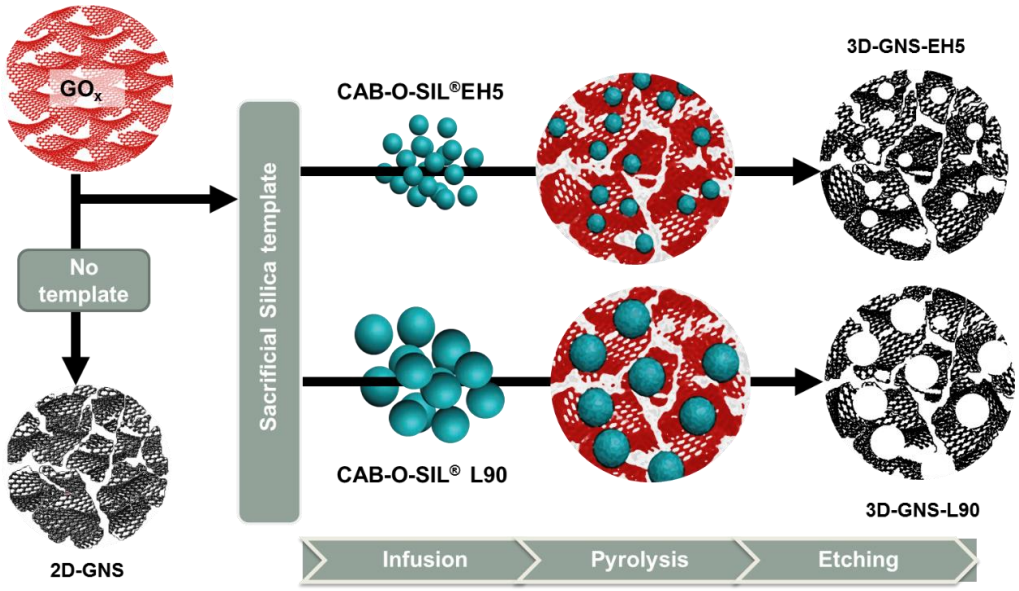

Figure 10. Schematic illustration of the synthesis procedures for modifying 3D-graphene's morphology using Sacrificial Support Method by incorporating the silica templates, thermal pyrolysis and etching.

4.1 Morphological Characterization of 3D-Graphene Nanosheets

This section discusses the fabrication of hierarchically structured 3D-Graphene nanosheets with varying levels of micro-, and macro-porosities by a scalable and facile strategy utilizing smaller and larger sized sacrificial silica templates, EH5 and L90 (Sacrificial Support Method). The method of reduction (thermal pyrolysis, 7 at. % H_2 was kept constant, as thermally reduced 3D-GNS-H_2 supports were optimized to have the highest degree of graphitization in Chapter 2. To form morphological correlations, the surface chemistries (i.e. via thermal reduction) were not varied.

Fig.10 shows a schematic illustration of fabricating 3D-Graphene nanosheets with porous morphologies. As described in section 2.1.1, the exfoliated GO_x was infused with commercial nanosized silica particles available in various sizes, particularly Cab-O-Sil® EH5 (surface area ~400 $m^2 g^{-1}$) and Cab-O-Sil® L90 (surface area ~90 $m^2 g^{-1}$). The GO_x nano pellets were then thermally reduced to graphene nanosheets (GNS) in H_2 atmosphere. After pyrolysis, the removal of the L90 and EH5 silica templates through chemical leaching with HF introduced a network of connected pores within the graphene nanosheets framework

SEM was employed to observe the morphology of 3D-GNS-EH5 and 3D-GNS-L90 supports post HF treatment. The SEM images of the 3D-Graphene nanosheets templated with silica L90 and EH5 are shown in Fig. 11 (a and b, respectively) under the same magnification and scale. Both the 3D-GNS-L90 and 3D-GNS-EH5 have three dimensional morphologies, suggesting that the silica EH5 and L90 templates successfully form 3D frameworks containing large tunnels and small pores. Spherical grooves ranging in several nanometers can be seen engraved into framework during acid etching of the infused template. Other physical-chemical characterization of these supported catalysts (composition, structure, and speciation) was previously described in detail. In brief, these thermally reduced 3D-GNS supports are a few layers thick, highly graphitized (82% graphitic carbon) and crystalline in nature due to the lower level of disorder and higher degree of sp^2 carbons, confirmed using Transmission Electron Microscopy (TEM), X-ray Photoelectron spectroscopy (XPS), X-ray Diffraction (XRD) and Raman Spectroscopy[60, 132, 141] in Chapter 2.

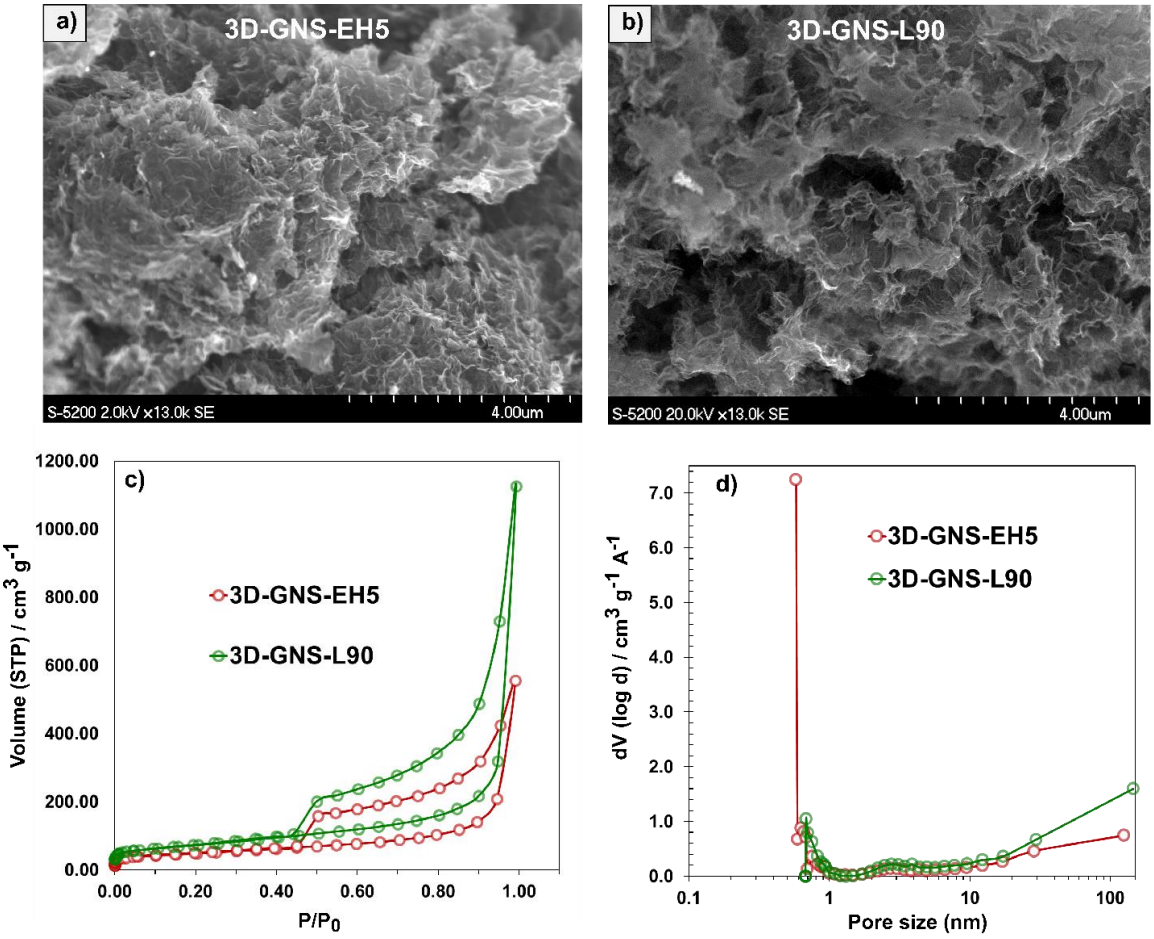

Figure 11. Scanning Electron Microscopy images of 3D-Graphene nanosheets templated with a) EH5 silica template, 3D-GNS-EH5; b) silica L90, 3D-GNS-L90; under the same magnification c) N_2 adsorption and desorption isotherms and d) BJH Pore size distribution curves of three dimensional graphene nanosheets, 3D-GNS-EH5 and 3D-GNS-L90 supports fabricated with two different silica templates

BET analysis in previous studies on ethanol oxidation reactions catalyzed by catalysts from this family also showed that the surface areas of the graphene supports varied greatly from 101 m^2 g^{-1} for 2D-GNS supports that were not templated, to 400 m^2 g^{-1} and 270-320 m^2 g^{-1} for 3D-GNS-EH5 and 3D-GNS-L90, respectively [132]. The lower BET surface area of 2D-GNS was previously attributed to its stacked morphology, whereas differences in surface areas of the templated 3D-GNS supports were attributed to the differences in morphologies

arising from etching of the two different templates, although no detail investigation was previously conducted to estimate the pore size distribution of these materials.

As it can be seen from the SEM images in Fig 11.a-b, – taken as the same magnification –it is evident that the 3D-GNS-L90 support in Fig. 11b has larger pores present, which produces a much more 3D-connected open carbon network, versus the compact, rough and "coral" like morphology of the 3D-GNS-EH5 support (Fig. 11a). Since the total surface area of powdered materials is the sum of the surface areas of pores of all sizes, and is inversely related to the size of pores for a given mass: materials with a greater percentage of small pores generally have a larger surface area than materials with lesser number of large pores.[142] Hence, the differences observed in BET surface areas between the 3D-Graphene supports templated with EH5 and L90 could also be attributed to pores of different sizes.

The micro- and macro-porous features of the 3D-GNS-EH5 and 3D-GNS-L90 supports were further confirmed by N_2 adsorption and desorption isotherms obtained. The porous structures of materials can be determined based on the shapes of isotherms and hysteresis loops. The adsorption-desorption curve shows the typical features of a type-IV isotherms associated with capillary condensation taking place in the pores.[143] Moreover, the hysteresis loop of H2 - between the relative pressure (P/P_0) ranging between of 0.4 to 1.0 in Fig. 11c is indicative of relatively uniform channel-like pores and network connectivity. It can be seen that both the 3D-Graphene supports have a similar *trend* in N_2 adsorption-desorption isotherms – which indicates that the *shape* of the templated pores is similar in both the supports. However, the larger hysteresis loop in the high P/P_0 region for 3D-GNS-L90 corresponds to the unrestricted monolayer-multilayer adsorption in presence of larger

macro pores in the support, which is also consistent with other macroporous graphene supports observed in literature.[144]

Figure 11d shows the BJH pore-size distribution profiles obtained using N_2-adsorption experiments for the porous graphene materials prepared in our lab, 3D-GNS-EH5 and 3D-GNS-L90. The BJH pore size distributions, although not highly precise for this type of intricate pore geometries, does show the existence of a wide pore size range from a nanometer to a few hundred nanometer.[145] Ideally, the N_2 adsorption technique has the ability to detect pores that are larger than the molecular diameter of N_2 (3.5 Å) can be detected by.[143] Pores that are smaller than 2 nm in diameter are considered to be micropores, whereas pores larger than 50 nm are called macropores, while those with diameters in between are mesopores, as defined by IUPAC.[146]

The distribution of pores of various sizes is clearly illustrated in Fig. 11d. The BJH pore size distribution results show that both 3D-GNS-EH5 and 3D-GNS-L90 supports have a similar degree of mesopores between 2-40 nm. However, a significant difference was observed for the degree of micropores of few nanometers in size (<2nm) in the 3D-GNS-EH5 templated supports compared to 3D-GNS-L90, whereas large percentage of the micropores with sizes of < 2 nm are present, indicating the main pore volume is contributed by small size pores. In contrast, 3D-GNS-L90 has a higher degree of macroporosity with pores ranging > 50 nm, with comparatively fewer percentage of micropores < 2 nm in comparison to 3D-GNS-EH5, which indicates that the micropores in EH5 templated graphene contributes towards a higher percentage of the surface area than that of L90 templated graphene.

It is worth noting that the volume of the pores can be tailored through varying the size of the hard template. The smaller sized EH5 template lead to the formation of a higher percentage of smaller pores, with an average pore size volume of 0.94 cm^3 g^{-1}, whereas removal of the larger sized L90 template lead to the formation of a higher percentage of larger pores > 50 nm, with an average pore volume of 1.9 cm^3 g^{-1}, which as is almost twice as large. The combination of these pores formed on the graphene nanosheets could have different effects on electrochemical reactions of Pd nanoparticles deposited on the 3D-GNS supports, and should be studied in order to design cathode materials with high electrocatalytic activities.

4.2 Effect of Porosity on Electrochemical Activity

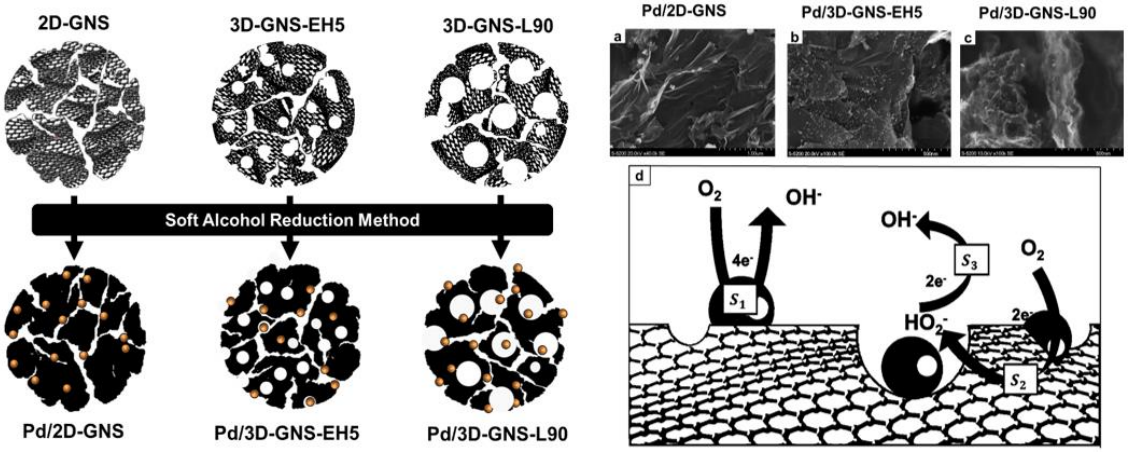

Figure 12. Schematic illustration and SEM micrographs of Pd nanoparticles deposited on a) 2D-GNS, b) 3D-GNS-EH5 and c) 3D-GNS-L90. d) Illustration of proposed direct 4e- and 2x2e- transfer oxygen reduction mechanism proceeding in the synthesized porous catalysts.

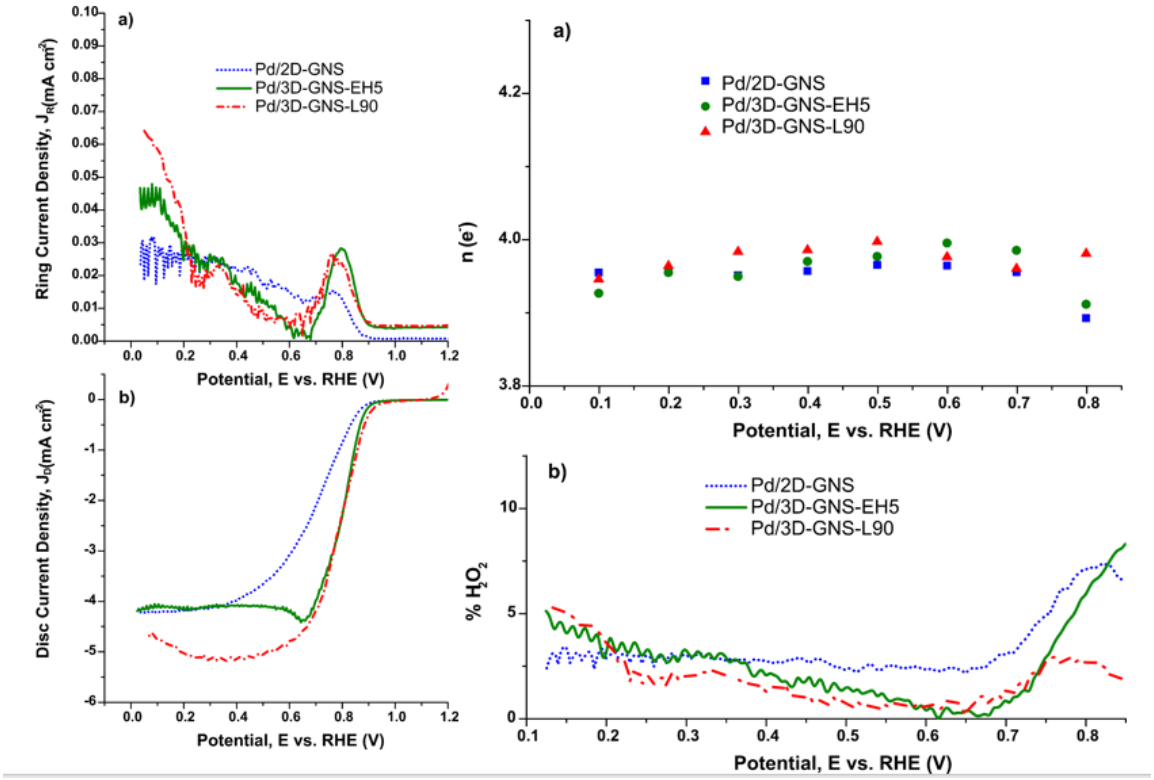

Figure 13. a-b) Dual Electrode Linear sweep voltammograms of Pd/2D-GNS, Pd/3D-GNS-EH5, Pd/3D-GNS-L90 catalysts obtained in O_2 saturated 0.1 M NaOH at 5 mV s^{-1} and 1600 RPM. Note that the Y axis in Fig. 13a was adjusted to a smaller scale to show the differences in JR. Figure. 13 (LHS) a) Hydrogen peroxide yield (% H_2O_2) and number of electrons transferred, n(e-) in O_2 saturated 0.1 M NaOH by Pd/2D-GNS, Pd/3D-GNS-EH5 and Pd/3D-GNS-L90 at 1600 RPM and 5 mV s^{-1}.

The two crucial factors that affect the ORR performance of a catalyst depends on the abundance of the active sites and pore structure of the catalyst layer. Since the loading of the active sites were maintained constant (i.e. 30 wt% Pd), we investigated the effect of support morphology on oxygen electroreduction in alkaline media by obtaining linear sweep voltammetry (LSV) of Pd/3D-GNS-EH5 and Pd/3D-GNS-L90 and Pd/2D-GNS catalysts in 0.1M NaOH saturated with O_2 at room temperature using a rotating ring disc electrode (RRDE).

Fig. 13a and Fig. 13b show the ring and disc current densities of Pd/GNS catalysts. It was observed that there was a positive shift of the half-wave potential ($E_{1/2}$) by almost 150 mV for the Pd/3D-GNS-EH5 and Pd/3D-GNS-L90 catalysts compared to Pd/2D-GNS. There was also a considerable increase in ring and disc currents (J_D) in the upper kinetic regions between 0.9 and 0.8 V which was prominent especially for the Pd/3D-GNS (EH5 and L90) catalysts. This increase could be due to local depletion of oxygen in the highly surface area templated pores present in the 3D-GNS nanocomposites. The ORR current densities of the Pd/2D-GNS, Pd/3D-GNS-EH5 and Pd/3D-GNS-L90 catalysts at 0.6 V were 4.85 mA cm^{-2}, and 3.1 mA cm^{-2} 4.3 mA cm^{-2} and 4.85 mA cm^{-2}, respectively.

The higher current densities obtained from the Pd/3D-GNS catalysts can be attributed to the novel 3-dimensional controlled morphology and higher surface areas of the 3D-GNS supports designed by the Sacrificial Support Method, facilitating oxygen electroreduction. Conversely, the lower performance of the Pd nanoparticles supported on 2D-GNS supports could be due to the stacked 2D-morphology of the non-templated GNS supports obstructing reactant (O_2) and electrolyte transfer to the reaction interface in the active site. Among all, Pd/3D-GNS-L90 displays superior activity to all the other samples, in terms of onset potential and half-wave potential, as well as the diffusion limiting current density, which could be due to the macropores in 3D-GNS-L90 minimizing diffusion limitation commonly observed for microporous materials. The LSV's demonstrate that the electrocatalytic activity and ORR kinetics are dependent on the porosity structure as well as the surface area of the graphene supports.

4.3 Effect of Porosity on Hydrogen Peroxide Yields

To further examine the effect of GNS support morphology, RRDE measurements were employed to evaluate the peroxide intermediates produced and no. of electrons transferred at different potentials during oxygen reduction reactions, calculated from Eqn. (4) and (5). The number of electrons transferred during oxygen electroreduction between 0.85 and 0.1 V vs. RHE was calculated to be between n=3.9 and n=4 for Pd/3D-GNS-L90, Pd/3D-GNS-EH5 and Pd/2D-GNS, indicating that independent of support morphology, all the palladium-graphene catalysts mostly catalyzed the 4-electron reduction reaction process of O_2 directly to OH- (S_1 pathway, Fig. 12d). However, it could also be due to the two-by-two electron (2x2e-) mechanism where O_2 is reduced HO_2^- intermediates. It can be seen that Pd nanoparticles deposited on 3D-graphene supports templated with larger L90 silica template - Pd/3D-GNS-L90 - produced the least amount of HO_2^- in the kinetic regions (0.8 V), with a yield of only ~2.5%, followed by Pd/3D-GNS-EH5 5.8% and Pd/2D-GNS at 7.1%.

However, in the mixed diffusion-kinetics controlled region and average fuel cell operating voltage of 0.6 V, the HO_2^- yield by both the Pd/3D-GNS (L90 and EH5) catalysts was negligible, whereas Pd/2D-GNS continued to produce higher levels of peroxide in comparison. With decreasing potential, there was again a small increase in HO_2^- yield in the mass transfer controlled regions (< 0.6 V), where Pd/GNS catalysts had an average peroxide yields of about 3.5%. All the catalysts seem to be completely reducing oxygen via the 4-electron transfer mechanism. However, the peroxide yields indicate that Pd/3D-GNS-L90 is reducing oxygen via the highly desirable and efficient direct $4e^-$ process where O_2 is completely reduced to OH^-, without producing significant amounts of intermediates

throughout all potentials. Whereas, Pd/3D-GNS-EH5 catalyst might be reducing oxygen via the 2x2 electron mechanism in the upper kinetic region, followed by direct 4e- transfer mechanism in the mixed and diffusion controlled regions.

Overall, the effect of morphology between 3D-GNS -L90 and 3D-GNS-EH5 supported Pd composites was largely pronounced two categories: (ii) limiting current densities (J_d) between 0.7 and 0.1 V and, (ii) peroxide yields between 0.7 and 0.85 V. As it can be seen from Fig 13, Pd nanoparticles deposited on 3D-GNS modified with larger L90 template has higher limiting current densities and lower peroxide yields (1-3%) in the upper kinetic region, compared to Pd nanoparticles deposited on the 3D-GNS support modified with smaller EH5 template ($\%HO_2^-$ = 2-8%). The larger degree of macropores of >50 nm in diameter, seen in the nitrogen adsorption analysis, could be enabling faster oxygen diffusivity into the graphene matrix and facilitating electron charge transfer. Moreover, any amount of HO_2^- generated within the catalyst, could be getting trapped and re-adsorbed in to the larger pores etched inside the 3D-GNS-L90 matrix (s2 pathway, Fig 13d). This would allow the HO_2^- intermediates to renter the active sites of Pd and undergo further reduction (S3 pathway, Fig 13d).

Conversely, the lower limiting current densities of Pd nanoparticles supported on graphene supports modified with smaller EH5 sacrificial template, Pd/3D-GNS-EH5 could be due to the limited transport of oxygen into the active sites through the higher degree of microporous channels < 2nm. Moreover, the micro-pore would either be totally or partially blocked by the similarly sized Pd nanoparticles, rendering them inaccessible and substantially decreasing the efficiency of complete O_2 reduction. (pathway S2, Fig 13d). It is also possible that a significant portion of nanoparticles – which have an average size of 5.3 nm,

may have settled into these micropores, resulting in little or no electrochemical activity because of the difficulty of reactant accessibility.[147, 148] These smaller pores could also be promoting the expulsion of HO_2^- from the catalyst support without giving it a change to get reduced further, thereby contributing to the higher percentage of HO_2^- generated by Pd/3D-GNS-EH5 at higher potentials in comparison to Pd/3D-GNS-L90. In contrast, the larger pores in 3D-GNS-L90 could accommodate Pd nanoparticles ~5nm than micropores. Thus, the utilization for the surface area in the large pores was much higher than that in the small pores. These results also suggest that the role of micropores and mesopores have varying effects towards enhancing or limiting ORR performances at a range of varying potentials. In particular, graphitized supports with fewer micro-pores and larger degree of macro-pores could be playing a role in inhibiting peroxide generation and promoting the direct 4 electron reduction of oxygen.

Chapter 5

Role of Nitrogen in Pd supported Nitrogen doped 3D-Graphene Nanosheets

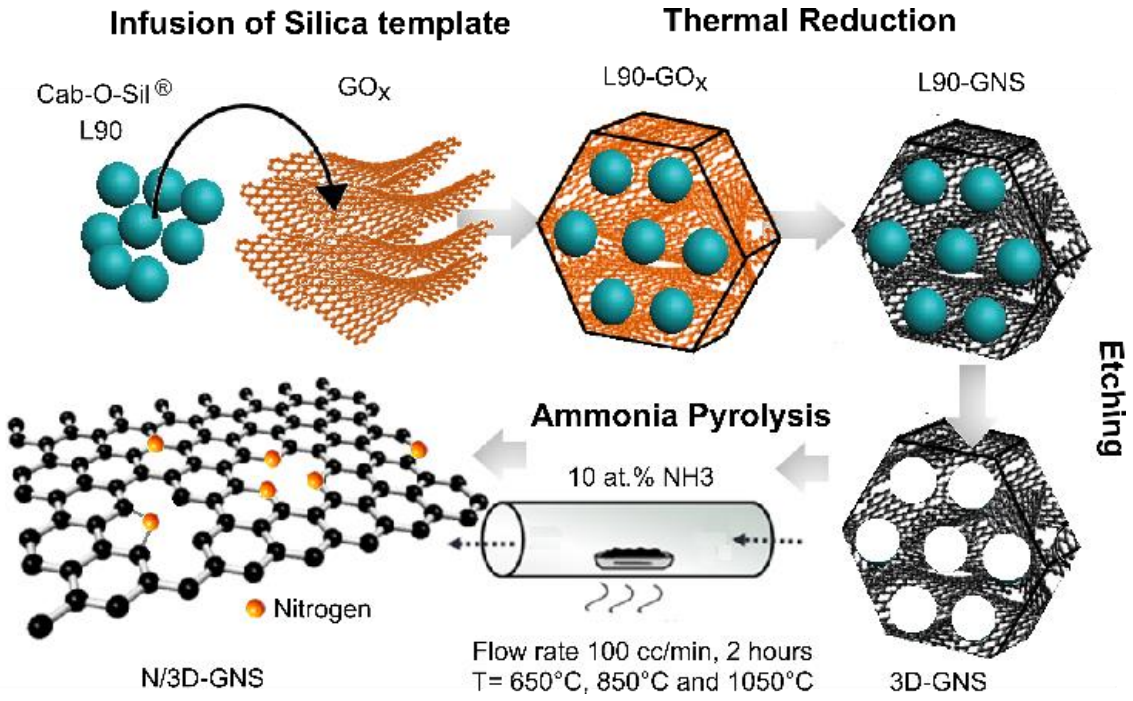

Figure 14. Schematic illustration of the synthesis procedures of nitrogen doped 3D-Graphene nanosheets (N/3D-GNS)

In this section, the synthesis–structure–property correlations of nitrogen moieties doped into Nitrogen doped 3D-graphene nanosheets (N/3D-GNS) is investigated using a combination of spectroscopic and electrochemical techniques. The optimized thermally reduced 3D-Graphene nanosheets from Chapter 2 was templated with the silica L90 template for the optimized macroporous structure, as explained in Chapter 3, and used as precursors for nitrogen doping.

Fig. 14 illustrates the fabrication procedure for synthesizing nitrogen doped three-dimensional graphene nanosheets (N/3D-GNS) using the Sacrificial Support Method. The first step of the synthesis process consisted of impregnating the exfoliated GO_x solution with

a hard template (fumed silica Cab-O-Sil® L90), followed by thermal reduction of the GO_x nanopallets to Graphene nanosheets (GNS). Then, removal of the silica template via acid etching engraved an open-frame porous three-dimensional structured graphene nanosheets, giving it a three-dimensional morphology. Finally, the 3D-GNS supports were doped with nitrogen via NH_3 pyrolysis, at three different temperatures, 650°C, 850°C and 1050°C, as elaborated in Chapter 2.

5.1 Morphology of N-doped 3D-Graphene Nanosheets

(i)

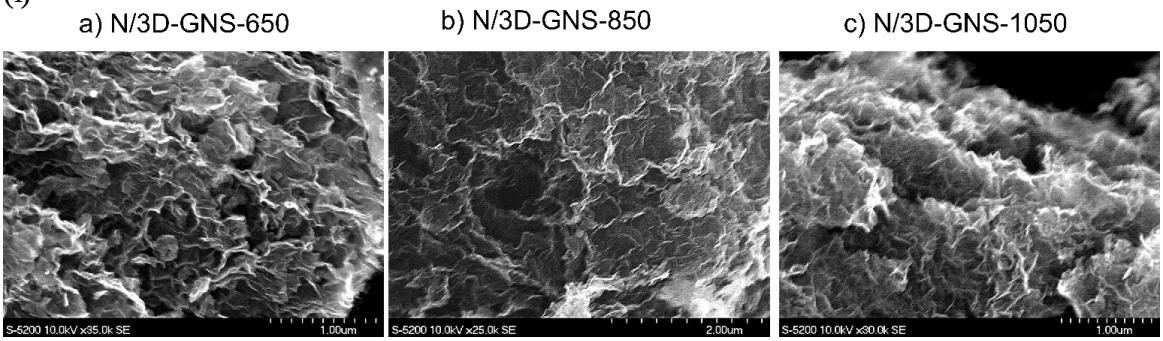

(ii)

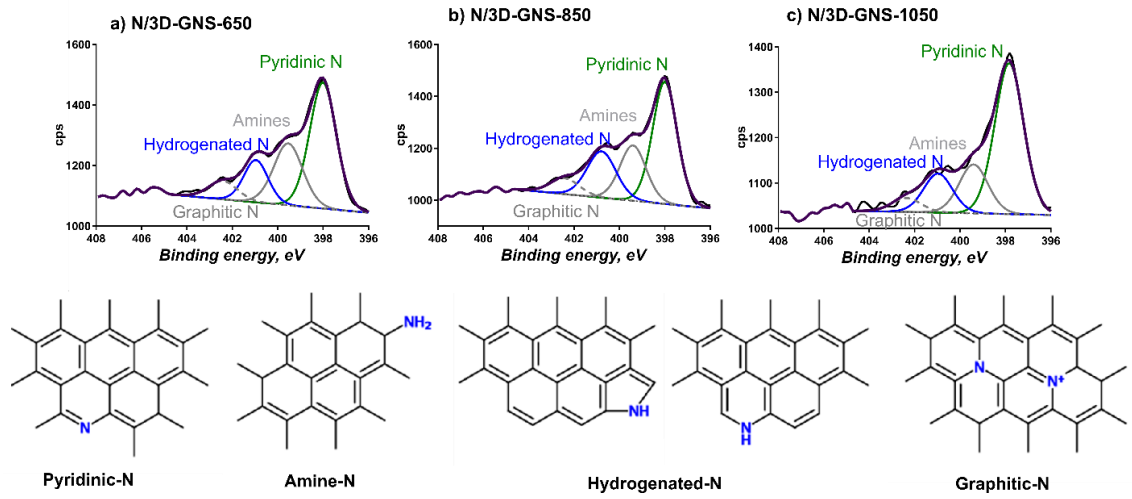

Figure 15. (i) Scanning Electron Microscopy images of the three-dimensional graphene nanosheets (3D-GNS) supports doped with nitrogen at a) 650°C, b) 850°C, c)1050°C. (ii) High-resolution N1s XPS spectrum for three-dimensional graphene nanosheets doped with nitrogen at a)650°C, b) 850°C and c) 1050°C. Schematic representation of different types of N species (graphitic-, pyridinic-, hydrogenated- and amine-N) present in nitrogen doped 3D-graphene nanosheets.

Figure 15(i) shows the SEM micrographs of the 3D-Graphene nanosheets doped with nitrogen at three different temperatures, i.e a) N/3D-GNS-650, b) N-3D-GNS-850 c) N/3D-GNS-1050. As it can be seen, the morphologies of the three materials are relatively identical in terms of its three-dimensional morphology due to the pores engraved into its matrix during acid etching sacrificial templating, which leaves an interconnected network of channels within the graphene nanosheets.

Other physical and chemical characterization the bare 3D-GNS supports were previously described in detail. In brief, these thermally reduced 3D-GNS supports are a few layers thick, highly graphitized (82% graphitic carbon) and crystalline in nature due to the lower level of disorder and higher degree of sp2 carbons, confirmed using Transmission Electron Microscopy (TEM), X-ray Photoelectron Spectroscopy (XPS), X-ray Diffraction (XRD) and Raman Spectroscopy.[60, 132] Since all other parameters (GO_x precursor, thermal reduction, size of template L90) were kept constant prior nitrogen doping, no changes in physical properties of the N/3D-GNS supports are observed except the chemical speciation of the nitrogen functionalized moieties incorporated in this study.

Table 3. The abundance of C 1s, N 1s and O 1s in the 3D-Graphene nanosheets doped with nitrogen at 650°C, 850°C and 1050°C.

Sample Identifier	C 1s %	N 1s %	O 1s %
N/3DGNS-650	93.5	3.4	3.1
N/3DGNS-850	93.3	4.0	2.7
N/3DGNS-1050	93.0	2.6	4.4

5.2 Effect of Pyrolysis temperature on Nitrogen Moieties

X-ray photoelectron spectroscopy (XPS) was performed to evaluate the chemical 3D-GNS supports doped with nitrogen at 650°C, 850°C, and 1050°C. Table 3 shows the atomic composition of three materials obtained from the XPS spectra. The surface of N/3D-GNS-650, N/3D-GNS-850 and N/3D-GNS-1050 consists of carbonaceous (C 1s), nitrogen-functionalized (N 1s) and oxygenated species (O 1s). While the carbon content is relatively the same at ~93.3% – as expected – the nitrogen and oxygenated species varied with temperature. The nitrogen species were doped into the graphene matrix using 10% NH_3, whereas the presence of oxygen could be due to the presence of surface functionalized oxygenated species such as -OH and -OOH.

XPS measurement revealed that samples with a nitrogen (N 1s) concentration of 3.4, 4.0 and 2.6 at. % were obtained at 650°C, 850°C and 1050°C, respectively, thus verifying that nitrogen was successfully doped into 3D-GNS after NH_3, pyrolysis. With the three different temperatures that were chosen to identify the optimal range, XPS results show that thermally doping graphene sheets with nitrogen at 850°C results with the higher nitrogen content (4.0%) and lowest oxygen content (2.7%). Since all the three samples were doped with nitrogen for the same duration (2 hours) under 10% NH_3 pyrolysis, the abundance of the species can be attributed to the difference in pyrolysis temperatures, with 850°C being the optimal temperature that seems to give rise to the highest abundance in nitrogen moieties and lowest degree of oxygenated functionalization.

It is known that nitrogen that is present within the graphitized carbon materials can exist in the form of several different chemical groups, which, in principle, can be distinguished by X-

ray Photoelectron spectroscopy (XPS). Fig. 15.ii) a-c displays the high-resolution N 1s XPS spectrum corresponding to 3D-Graphene nanosheets doped with nitrogen at 650°C, 850°C and 1050°C.

Table 4. Quantitative abundance percentage for each nitrogen moiety detected in the pyrolyzed N/3D-GNS samples

Sample	Pyridinic-N	Amine-N	H-N	Graphitic-N/ N^+	H-N/ Pyridinic-N	Graphitic-C	C_xO_y
N/3D-GNS 650	50.0	26.8	15.3	7.9	*0.30*	61.6	37.6
N/3D-GNS 850	47.9	23.3	21.5	7.3	*0.45*	63.2	35.0
N/3D-GNS-1050	59.6	19.4	15.4	5.5	*0.26*	84.7	13.9

The 70% Gaussian/30% Lorentzian peak fitting technique of the N 1s XPS spectra of the samples revealed the presence of four main types of nitrogen: pyridinic nitrogen at 398.2 eV, amine nitrogen at 399.4 eV, hydrogenated nitrogen (such as pyrrolic and hydrogenated pyridine) at 400.8 eV and mixture of graphitic and protonated nitrogen at 402.3 eV. The quantitative abundance percentage for each nitrogen moiety detected in the pyrolyzed N/3D-GNS samples estimated by deconvoluting the XPS spectra is summarized in Table 4. The abundance of graphitic-N decreased - from 7.9 to 5.5% - with an increase in temperature – from 650°C to 1050°C. As for hydrogenated-N, the abundance increases from 15.3 to 21.5% at 850°C and then decreasing back to 15.4% with increased pyrolysis temperature. It was also noted that at 850°C, the N/3D-GNS supports contained the highest percentage of hydrogenated-N abundance, and the highest hydrogenated-N to the pyridinic-

N ratio (0.45) at the same temperature (850°C). One the other hand, the abundance of pyridinic nitrogen increases – from 50% to ~60% as the temperature rises to 1050°C.

These observations could indicate that graphitic nitrogen moieties could be decomposing and get converted to hydrogenated and pyridinic-N moieties with increase in pyrolysis temperatures, and this gradual change in highest % nitrogen abundances (shown in brackets below, obtained from Table 2) could also be indicative of chemical transformation of the nitrogen moieties in the order of: Pyrolysis $\xrightarrow{650°C}$ Graphitic N (8%) $\xrightarrow{850°C}$ Hydrogenated-N (25%) $\xrightarrow{1050°C}$ Pyridinic-N (60%).

Sample pyrolyzed at highest temperature (1050°C) also had the largest amount of graphitic carbon (84.7%) as shown in Table 2 which is expected, as oxygenated functional groups decompose at higher temperatures.

5.3 Effect of Pyrolysis temperature on the electrochemical performance of nitrogen moieties in Acidic and Alkaline Media

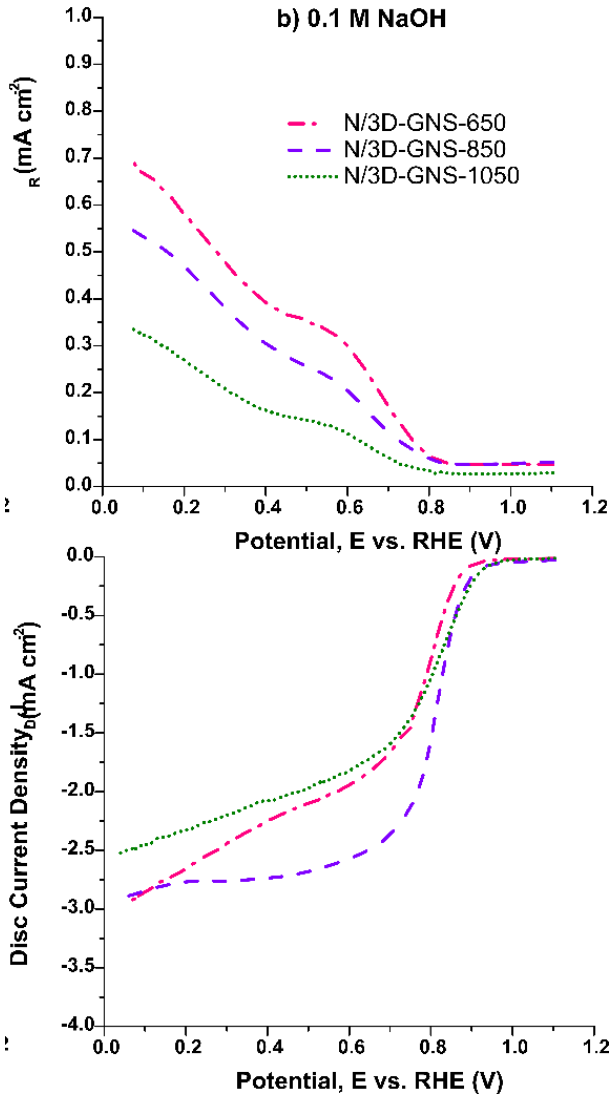

Figure 16. Linear sweep Voltammograms showing Ring and Disc current densities obtained for N/3D-GNS samples pyrolyzed: 650 °C (dash-dot). 850 °C (dash) and 1050 °C (dot) in 0.1 M NaOH electrolytes saturated with O_2 at 1600 RPM and 5 mV s^{-1}.

It is highly desirable that the oxygen reduction reaction pathways proceed to the efficient 4 electrons (e-) process where O_2 is completely reduced, versus the two-by-two electron (2x2e-) mechanism where O_2 is reduced to intermediates.

Table 5. Oxygen Reduction Reaction Pathways in acidic and alkaline media

ORR pathway	Acidic Media	Alkaline Media
4 e-	$O_2 + 4e^- + 4H^+ \rightarrow H_2O$	$O_2 + 2H_2O + 4e^- \rightarrow 4OH^-$
2 x 2 e-	$O_2 + 2e^- + 2H^+ \rightarrow H_2O_2$ $H_2O_2 + 2H^+ + 2e^- \rightarrow 4H_2O$	$O_2 + H_2O + 2e^- \rightarrow HO_2^- + OH$ $H_2O + HO_2^- + 2e^- \rightarrow 3OH^-$

Since a multitude of specific nitrogen moieties was shown to form with a temperature dependence abundance as shown in the XPS spectrum analysis in Figure 15 and Table 4, RRDE measurements were performed to provide qualitative as well as quantitative information about the effect of the abundance of specific nitrogen moieties on electrochemical reactions taking place in alkaline media. Hence, to better understand the oxygen reduction activity of the nitrogen moieties in doped graphene in both acidic and alkaline media linear sweep voltammetry (LSV) measurements were recorded on N/3D-GNS doped supports prepared at different temperatures in O_2 saturated 0.1 M NaOH solution. The dual electrode linear sweep voltammograms of the N/3D-GNS-650, N/3D-GNS-850 and N/3D-GNS-1050C materials in alkaline media are shown in Fig. 16.

Table 6. Onset (E_{on}) and ($E_{1/2}$) half-wave potentials of the 3D-Graphene nanosheets doped with nitrogen at 650C, 850C and 1050C in alkaline (0.1 M NaOH) media.

Sample	E_{on} (V vs. RHE)	$E_{1/2}$ (V vs. RHE)
Electrolyte	0.1 M NaOH	0.1 M NaOH
N/3D-GNS-650	0.88	0.71
N/3D-GNS-850	0.90	0.80
N/3D-GNS-1050	0.90	0.78

In general, the performance of material towards oxygen reduction reactions can be determined potential wise based on onset and half wave potentials in the kinetic region. From the polarization curves in Fig 16, it was noted that all the three materials have similar onset potentials of ~0.9V in alkaline media. N/3D-GNS-850 shows the higher limiting current densities in alkaline media (3.0 mA cm^{-2}), followed by N/3D-GNS-650 and N/3D-GNS-1050. It was also observed that as the ratio of hydrogenated-N/pyridinic-N increases (given in brackets) in the order N/3D-GNS-1050 (0.26) < N/3D-GNS-650 (0.30) < N/3D-GNS-850 (0.45), so did their limiting current densities.

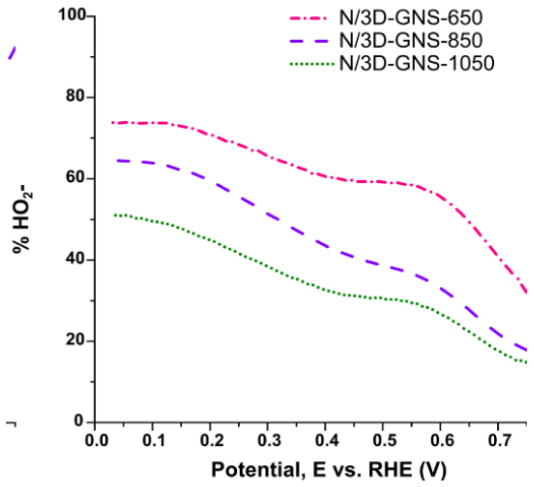

Figure 17. Peroxide yield (% HO_2^-) of N/3D-GNS materials in 0.1 M NaOH taken at 5 mV s^{-1} and 1600 RPM.

Table 7. Peroxide yields and no. of electrons transferred for 3D-Graphene nanosheets doped with nitrogen at 650°C, 850°C and 1050°C obtained at 0.6 V vs. RHE at 1600 RPM, 5 mV s^{-1}.

Sample	$\%H_2O_2/ HO_2^-$	n (e-)
Electrolyte	0.1 M NaOH	0.1 M NaOH
N/3D-GNS-650	55	2.8
N/3D-GNS-850	32	3.3
N/3D-1050	27	3.4

The ring current densities, shown in Figure 17, were then used to calculate the in (HO_2^-) yield. The HO_2^- yields generated at medium fuel cell operating voltages of 0.6 V is given in Table 2. It was also observed that N/3D-GNS-850, a sample with the highest hydrogenated-N, generated lower H_2O_2 yields in comparison to N/3D-GNS-1050, sample with the highest pyridinic-N abundance. However, N/3D-GNS-650, a sample with the highest graphitic-N, generated the highest peroxide yields.

Table 8. The abundance of C 1s, N 1s, O 1s, F 1as and S 2p of the dried RRDE inks comprising of Nafion and N/3D-GNS materials

Sample	C 1s %	O 1s %	N 1s %	F 1s	S 2p %
N/3D-GNS 650	77.0	10.6	2.5	9.5	0.3
N/3D-GNS 850	58.0	9.1	1.6	30.7	0.5
N/3D-GNS-1050	84.4	3.6	1.5	10.2	0.2

Moreover, XPS analysis of the dried inks prepared for RRDE experiment showed different ionomer to catalyst (I/C) ratios with N/3D-GNS-650 and N/3D-GNS-1050 materials having three times lower fluorine concentrations from nafion (9-10 at% of F) than for N/3D-GNS-850 sample (30 at% F, Table 8). This indicates the better integration of the ionomer and catalyst for the best performing sample. N/3D-GNS-850 also has the highest

amount of hydrogenated nitrogen (21.5%) which has high affinity towards interaction with sulfonate groups of ionomer and high amount of surface oxides (35%) which have shown to be beneficial for good carbon-ionomer interactions as well. [149] In contrast, although N/3D-GNS-650 possesses a high amount of surface oxides, it has a deficiency of hydrogenated nitrogen, while N/3D-GNS-1050 has both low surface oxides and low amount of hydrogenated nitrogen at the catalyst surface resulting in a bad integration of ionomer within the catalyst resulting in lower current densities.

While the role of the real electrocatalytically active sites is still controversial since their contribution to the catalytic activity is not well defined, some studies have suggested that pyridinic-N and pyrrolic-N enhance electrocatalytic activities, where other studies have shown graphitic-N plays a more prominent role. Density Functional Theory studies have shown that graphitic-N moieties are positively charged due electrons being transfer from N atom to the π conjugated state[150] also corroborated by the higher N 1s binding energy shift in the XPS spectrum is the positive charge on the N atom in the carbon matrix induces a negative on the neighbouring carbon atoms due to the screening effect. Hydrogenated and pyridinic nitrogen atoms, on the other hand, are formed by carbon atom substitution by N atoms, predominantly on edges of defect sites in the graphene plane because such carbon atoms are much more chemically active than those within the plane of perfect graphene. It is believed that carbon atoms next to these nitrogen defects have a significantly higher positive charge density for counterbalancing the strong electronic affinity of the nitrogen atom, resulting in an enhanced adsorption of O_2 and reactive intermediates that proceed to accelerate the ORR.[110, 151, 152]

Our XPS results indicate that the integration of catalyst with ionomer is essential for good performance, and although the graphene nanosheets doped with nitrogen contained all the three functional groups (pyridinic- N, hydrogenated-N, and graphitic-N),we were able to control their abundances using different pyrolysis temperatures to elucidate their role towards ORR kinetics in both alkaline and acidic media.

(ii) Alkaline Media:

In alkaline media, the high HO_2^- yields generated by N/3D-GNS-650 (55% at 0.6 V vs. RHE) still indicates that it mostly catalyzes the 2e- reduction of oxygen: $O_2 + H_2O + 2e^- \rightarrow HO_2^- + OH^-$. However, as the pyrolysis temperature increased to 850°C, there was a significant reduction in HO_2^- yields to (32% at 0.6 V) and increase in half-wave potential (0.80 V) for N/3D-GNS-850. This indicates that hydrogenated-N most probably catalyzes the 2x2 e- reduction of oxygen in alkaline media, i.e $O_2 + H_2O + 2e^- \rightarrow HO_2^- + OH^-$ followed by $H_2O + HO_2^- + 2e^- \rightarrow 3OH^-$. However, with further increase in temperature to 1050°C, there was a decrease in hydrogenated-N content, which lowered current densities but increase in pyridinic-N content, thereby maintaining the high half wave potentials and reduction in peroxide generation. In fact, N/3D-GNS-1050 generated lower HO_2^- yields (27%) in comparison to N/3D-GNS-850 (32%), suggesting that pyridinic-N might be acting as the second site for peroxihydroxyl reduction in alkaline media. Hence, pyridinic-N could be acting as the second catalytically active site that gradually converts the second step of the $2e^-$ pathway for the complete reduction of HO_2^- in alkaline media ($H_2O + HO_2^- + 2e^- \rightarrow 3OH^-$) which was also suggested and demonstrated in the previous study.[153]

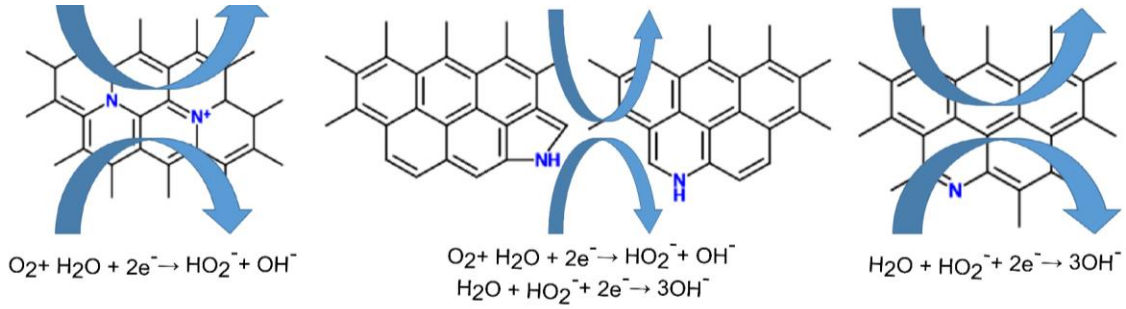

Figure 18. Proposed ORR mechanism steps on graphitic-, hydrogenated- and pyridinic- nitrogen moieties based on XPS and RDE results.

Hence, the results indicate that doping in 650°C gives rise to the highest % of graphitic-N, which decreases ORR electrokinetics such as half wave and onset potentials, more significantly in acidic media than in alkaline. On the contrary, doping at higher temperatures up to 1050°C decreases the abundance of graphitic nitrogen. Hence we see a positive shift in $E_{1/2}$ as well as E_{on}, but also decreases the abundance of hydrogenated-N moieties, which decreases its limiting current densities. It was also revealed that the ORR activities of samples prepared at a series of temperatures most closely correlated to the ratios of hydrogenated/pyridinic-N content. These results verify that the temperature of doping is crucial when fabricating N-doped graphene nanosheets as active catalytic or support materials, as each nitrogen moiety might be playing a role in enhancing or diminishing the ORR kinetics and performances various ways in different medias. Hence, it seems that nitrogen doping is optimal at 850°C, where having a higher abundance of hydrogenated-N in comparison to pyridinic-N, with a ratio of 0.45 gives rise to highest ORR current densities, highest onset, and half wave potentials. However, in any case, none of the nitrogen moieties

seemed to be catalyzing the *direct* 4e- reduction of oxygen, in neither acidic (O_2 + 4e- + $4H^+ \rightarrow H_2O$) nor alkaline media ($O_2 + 2H_2O$ + 4e- $\rightarrow 4OH^-$). Hence, nitrogen doped graphene materials – especially ones with a high abundance of hydrogenated-N moieties - would do best when utilized as a support for nanoparticles such Pd.

5.4 Catalyzing Nitrogen Doped 3D-Graphene Nanosheets with Palladium Nanoparticles for ORR in alkaline media

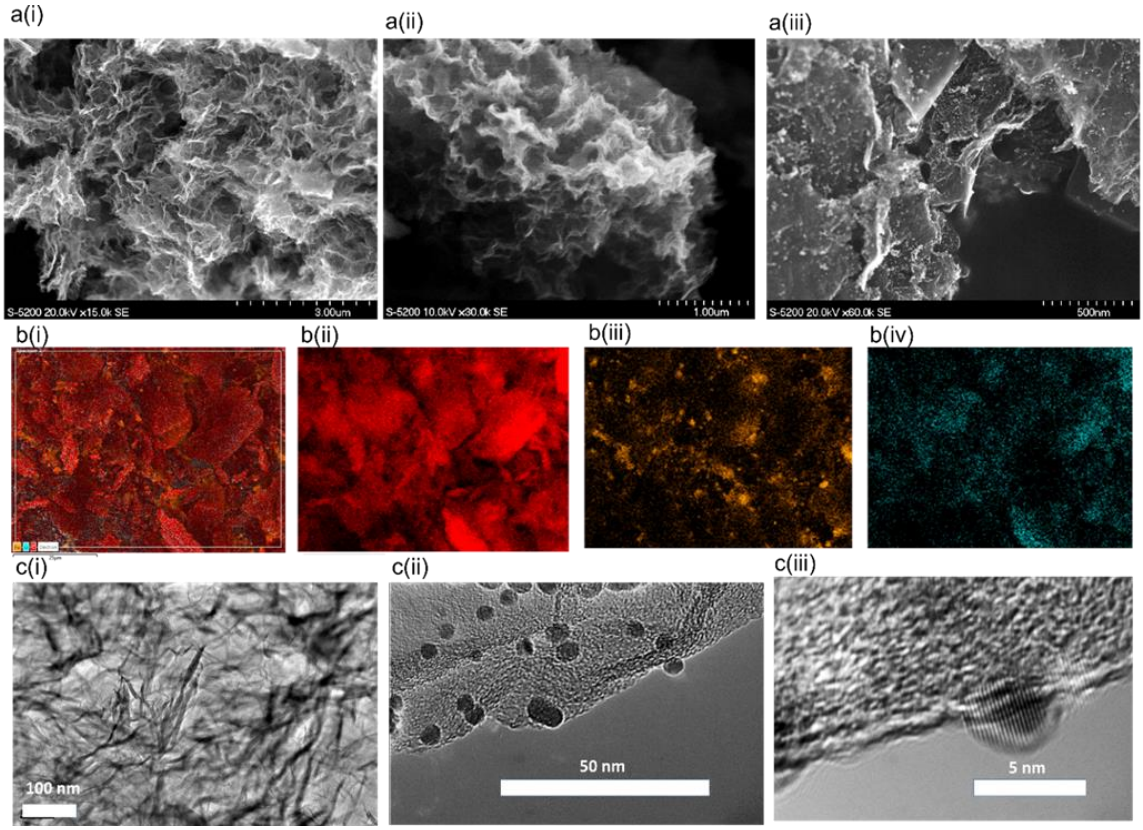

Figure 19 a) Scanning Electron Microscopy (SEM) images of (i) three-dimensional graphene nanosheets (3D-GNS) synthesized using the Sacrificial Support Method (ii) 3D-Graphene nanosheets doped with nitrogen using 10 at. % NH_3 (N/3D-GNS) and (iii) Pd nanoparticles deposited on N/3D-GNS using Soft Alcohol Reduction Method. b(i) Elemental distribution of Pd-N/3D-GNS nanocomposites determined using Energy Dispersive Spectroscopy (EDS) showing mapped distribution of b(i) carbon (red), palladium (amber) and oxygenated functional groups on carbon (cyan). Transmission Electron Microscopy (TEM) images of c(i) nitrogen doped 3D-Graphene nanosheets (N/3D-GNS), c(ii) Palladium nanoparticles deposited on the nitrogen three-dimensional graphene nanosheets (Pd/N-3D-GNS), c(iii) High Resolution Transmission Electron Microscopy (HRTEM) image showing the lattice fringes of a palladium nanoparticle supported on N/3D-GNS.

Palladium nanoparticles were deposited on the 3D-Graphene nanosheets doped with nitrogen at 850◦C, Pd-N/3D-GNS. The morphology of the Pd-N/3D-GNS nanocomposites was analyzed using Scanning Electron Microscopy (SEM). Fig. 19a(i) is a SEM micrograph of thermally reduced three-dimensional graphene nanosheets (3D-GNS) synthesized using

the Sacrificial Support Method. A hierarchy of spherical pores that were formed during etching of the sacrificial silica template can be observed. The network of pores also seems to be interconnected, forming channels within the matrix. Fig.19a(ii) shows the SEM micrograph of the 3D-GNS supports doped with nitrogen st 850◦C under 10 at% NH_3 pyrolysis. The porous morphology in the N/3D-GNS material can be observed following the pyrolysis treatment, and the average BET surface area was determined to be about 390 m^2 g^{-1}.

Fig 19a(iii) shows the SEM micrograph of palladium nanoparticle that were deposited on the N/3D-GNS supports using the Soft Alcohol Reduction Method (SARM). An elemental distribution of Pd-N/3D-GNS nanocomposites (Fig 19bi) determined using Energy Dispersive Spectroscopy (EDS) shows the relatively uniform distribution of the Pd nanoparticles (amber, Fig 19bii) that are deposited on the graphene supports (Fig 19bii, red), that contain oxygenated functional groups (Fig. 19biii, cyan), explained previously. Fig. 19c(i) shows the Transmission Electron Microscopy (TEM) image of the N/3D-GNS support, which is highly planar in nature. Fig. 19c(ii) shows the TEM image of Pd nanoparticles on N/3D-GNS supports deposited using the previously established surfactant-free Soft Alcohol Reduction Method. This method was shown to consistently deposit Pd nanoparticles with an average diameter of 5 nm uniformly dispersed on the surface.[154]

Fig. 20a shows the X-ray Diffraction patterns recorded for the 3D-GNS support and palladium nanoparticles deposited on the N/3D-GNS supports. The shift and increased intensity of the peak corresponding to graphitic carbon (*) at 26.3◦ (Fig. 20aii) indicates the increased graphitization of the N/3D-GNS supports following the additional NH_3 pyrolysis at 850◦C. The observed intense peaks at 2θ =40.0, 46.4, 68.1, 82.0 and 86.5, 119.7 and 124.7

deg. corresponds to the [111], [200], [220], [311], [222], [311] and [440] crystalline face centered cubic (FCC) structure of palladium in the Pd-N/3D-GNS nanocomposite (Fig. 20aii) respectively. This highly ordered crystalline facet of the Pd nanoparticles synthesized using SARM was also observed in the lattice fringes of the Pd nanoparticles as obseved in the High Resolution Transmission Electron Microscopy image in Fig. 19c(iii). X-ray photoelectron spectroscopy (XPS) was performed for analysing the surface composition of the Pd-N/3D-GNS nanocomposite and evaluating the chemical speciation of the elements present (Fig. 19a-b). Table 9 shows the abundances of the carbonaceous (C 1s), nitrogen (N 1s) and oxygenated (O 1s) and palladium (Pd 3d) – species obtained from the XPS spectra of Pd-N/3D-GNS. Carbon was present in its highly graphitized form, with 62.4% of the total signal coming from graphitic carbon.

Table 9. a) Percentage abundance of C 1s, N 1s, O 1s and Pd 3d species detected in the Pd-N/3D-GNS nanocomposite using X-ray Photoelectron Spectroscopy; b) abundance of functionalized C 1s carbon species; c) abundance of each nitrogen moiety detected and d) abundance of Pd species

a)	**C 1s**	**N 1s**	**O 1s**	**Pd 3d**	
	83.1	3.5	11.2	2.2	
b)	**Graphitic-C**	**C*, C-N %**	**C_xO_y**	**C 7 shake**	
	62.4	20.8	15.8	1.0	
c)	**Pyridinic-N**	**N_x-Pd/Amines**	**N-H**	**Graphitic-N**	**N-O**
	38.5	21.3	16.1	6.4	17.6
d)	**Pd**	**Pd-N_x, satellite**	**PdO**		
	44.2	30.9	24.7		

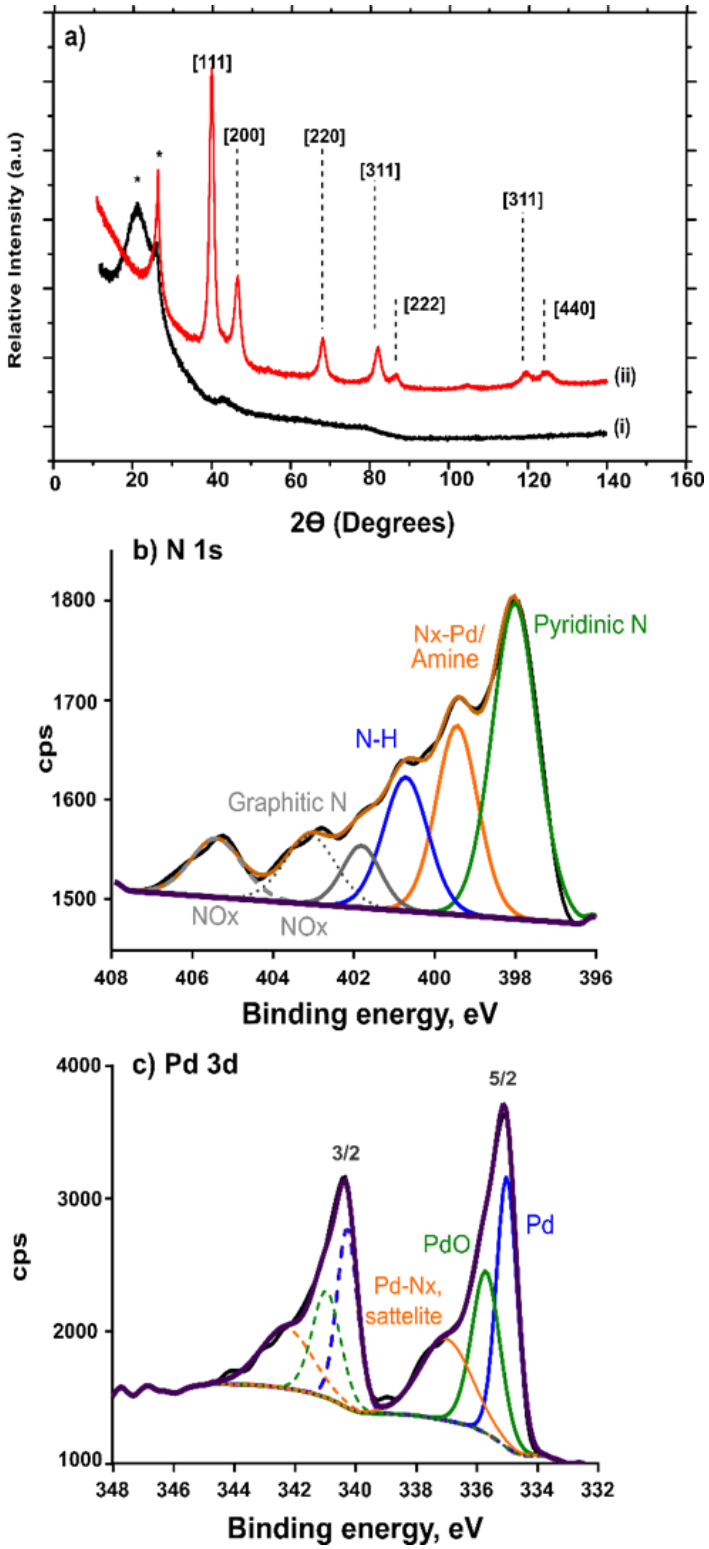

Figure 20. Powder X-ray Diffraction patterns of (i) 3D-GNS and (i) Palladium nanoparticles deposited on N/3D-GNS(ii); b) N 1s and c) P 3d X-ray Photoelectron Spectra of the Pd-N/3D-GNS nanocomposites.

This observation was also corroborated with the XRD patterns obtained in Fig 20a(ii). The high-resolution XPS spectra in the N 1s region is shown Fig. 20b. The overall nitrogen content in the Pd-N/3D-GNS nanocomposite from the XPS data was estimated to be around 3.5 at.%. The N 1s spectrum was deconvoluted into five major peaks that correspond to five main types of nitrogen: pyridinic nitrogen at 398.2 eV, nitrogen coordinated to Pd and amines at 399.4 eV, hydrogenated nitrogen, N-H (such as pyrrolic and hydrogenated pyridine) at 400.8 eV and mixture of graphitic and protonated nitrogen at 402.3 eV and oxidized nitrogen at 405 eV. A significant portion in the Pd 3d spectra (Fig. 20c) was from a major contribution coming from metallic Pd (44.2%, 335.0 eV), though oxidized Pd (335.6 eV) and some amount of Pd coordinated to nitrogen (Pd-Nx, 337.2 eV) which is also overlapped with satellite peak due to oxide, was also present. The XPS, along with the EDS and XRD results confirmed that the incorporation of Pd nanoparticles as well as nitrogen onto the 3D-Graphene structure was successful.

5.5 Electrochemical Activity of Pd-N/3D-GNS nanocomposites for Oxygen Reduction Reactions in Alkaline Media

The ORR electrocatalytic activity and reaction kinetics of the Pd-N/3D-GNS in alkaline media was studied from linear sweep voltammograms. Fig. 21a and Fig. 21b depicts ring and disc current desnities obtained obtained using a RRDE at 1600 RPM at 5 mV s^{-1} for bare 3D-GNS support, nitrogen doped 3D-GNS support N/3D-GNS, and Pd-N/3D-GNS nanoctromposite in 0.1 M NaOH saturated with O_2 at room temperature.

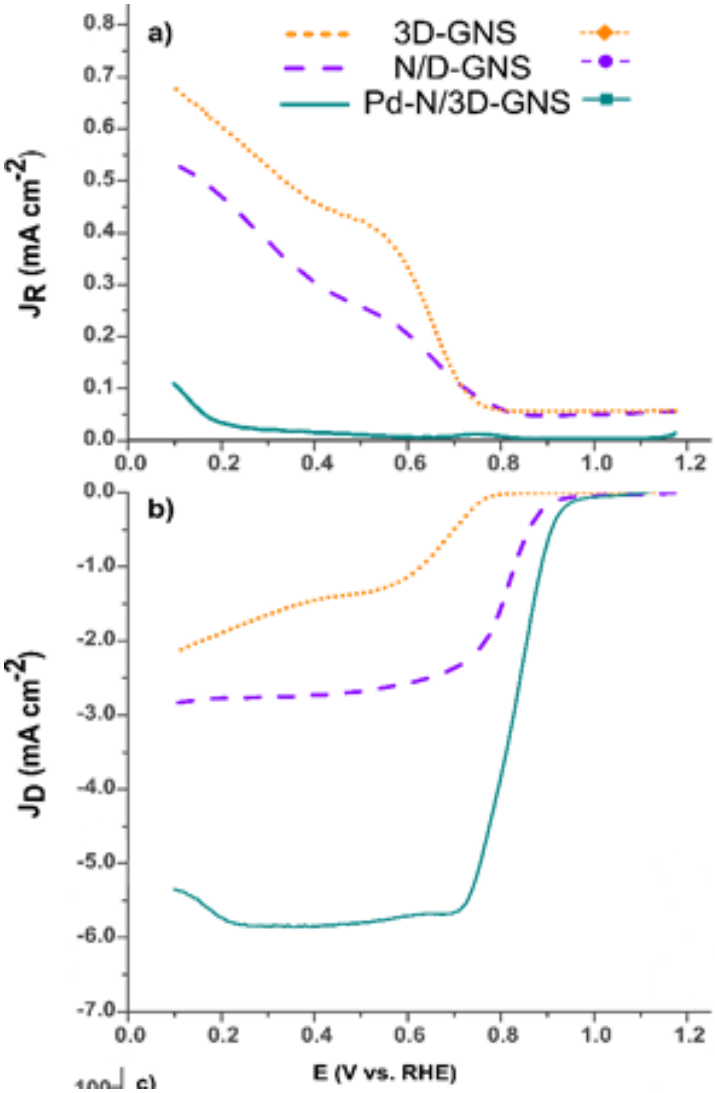

Figure 21 a-b) Dual electrode RRDE voltammograms for 3D-GNS, N/3D-GNS and Pd-N/3D-GNS in O2 saturated 0.1 M NaOH at 5 mV s-1 and 1600 RPM.

The absence of a ring current between 1.2 to 0.8 V vs. RHE indicates that the supports as well as the doped nanocompites all generate negligible quatities of peroxide intermediates at higher potentials. Fig. 21b shows that the Pd-N/3D-GNS nanocomposites had a high onset potential of 1.0 V vs. RHE. For oxygen electroreduction to be efficent, the reactions should occurring at potentials as close as possible to the thermodynamic reversible electrode potential.

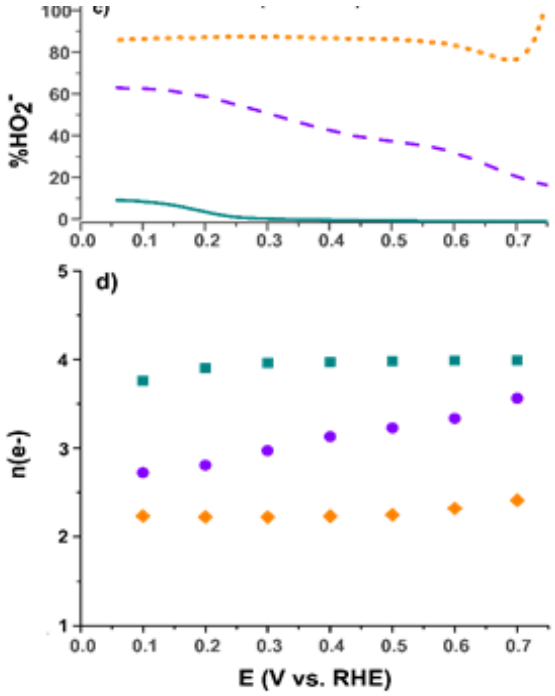

Figure 22. Fig 5. a-b) RRDE voltammograms, peroxide yield (HO_2^-) and number of electrons transferred, n(e-) by 3D-GNS, N/3D-GNS and Pd-N/3D-GNS in O_2 saturated 0.1 M NaOH at 5 mV s^{-1} and 1600 RPM.

A positive shift in the half wave potential by almost 100 mV of Pd-N/3D-GNS nanocomposites also indicates enhanced electrokinetic performance of the nanocomposite towards ORR. Moreover, the higher ORR current densities obtained for the nitrogen doped 3D-GNS support (N/3D-GNS) suggests that the nitrogen moieties might be providing additional active sites for peroxide reduction as well as oxygen electroreduction via the dual 2x2 e- mechanism, where as the bare 3D-GNS support was mainly responsible for peroxide generation by the 2e- ORR mechanism (Fig 22d). Based on the RRDE voltammograms obtained at 1600 RPM, it was determined that at average fuel cell operating voltages of 0.6 V, the Pd-N/3D-GNS nanocomposite generated negligible amonts of peroxide intermediates (0.5%), had the highest limiting current densities (5.75 mA cm^{-2}) and catalyzed the direct 4e- reduction of oxygen in alkaline media. Table 10 summarizes the paraments obtained for

the bare 3D-GNS and nitrogen doped N-3D/GNS, and compared to Pd-N/3D-GNS nanocomposite.

Table 10. Summary of the electrochemical properties of the 3D-GNS supports, Nitrogen doped 3D-GNS and Pd nanoparticles supported on nitrogen doped 3D graphene nanocomposites synthesized in this study.

		Parameters obtained at 0.6 V vs. RHE		
Catalyst/ Support	**Onset Potential, E_{on}, (V)**	**Limiting current, J_D (mA cm^{-2})**	**Peroxide yield (% HO_2^-)**	**No. of electrons, (ne-)**
3D-GNS	0.75	-1.14	84.4	2.3
N/3D-GNS	0.89	-2.6	33.3	3.3
Pd-N/3D-GNS	1.0	-5.75	0.5	4.0

To obtain further insight into the kinetics of oxygen electroreduction mechanism, the reaction kinetics was further analyzed using by Koutecky–Levich (K-L) carrying out RRDE measurements at different rotation rates (400-3500 RPM). The voltammetric profiles in Fig. 23a(i-iii) for 3D-GNS, N/3D-GNS and Pd-N/3D-GNS nanocomposites demonstrate the increasing current densities (J) enhanced with faster rotation rates (400 to 3500 RPM), ascribed to the shortened diffusion distance for O_2. Fig. 23a shows that the current densities of the synthesized Pd-N/3D-GNS catalysts were linearly dependent on the rotation speed. The Koutecky–Levich (K-L) plots in Fig. 23 a-c. The KL plot for Pd/N-3D-GNS exhibits excellent linear dependence and parallelism in comparison to N/3D-GNS and 3D-GNS, indicating first-order ORR kinetics with respect to the concentration of dissolved O_2 in the electrolyte.

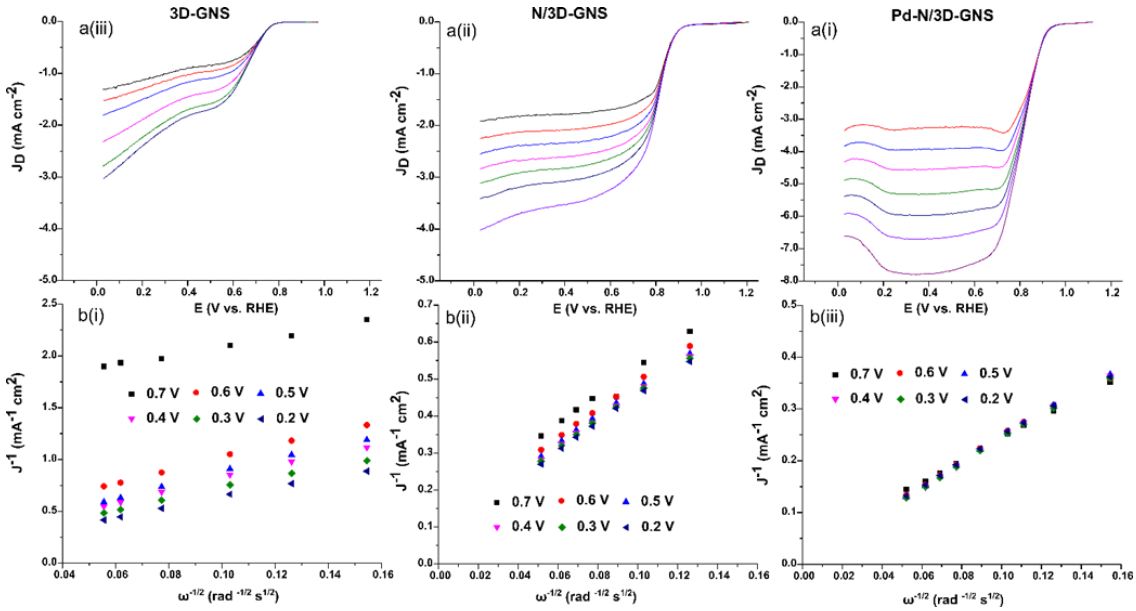

Figure 23. RRDE voltammetry curves obtained at different rotations (400 to 3500 RPM) at a scan rate of 5 mV s^{-1} and b) Koutecky–Levich plot of J^{-1} versus $\omega^{-1/2}$ obtained from 0.7 to 0.2 V for (i) 3D-Graphene nanosheets, 3-GNS; (ii) nitrogen doped 3D-Graphene nanosheets, N/3D-GNS and (ii) Pd-N/3D-GNS nanocomposites in O_2 saturated 0.1 M NaOH.

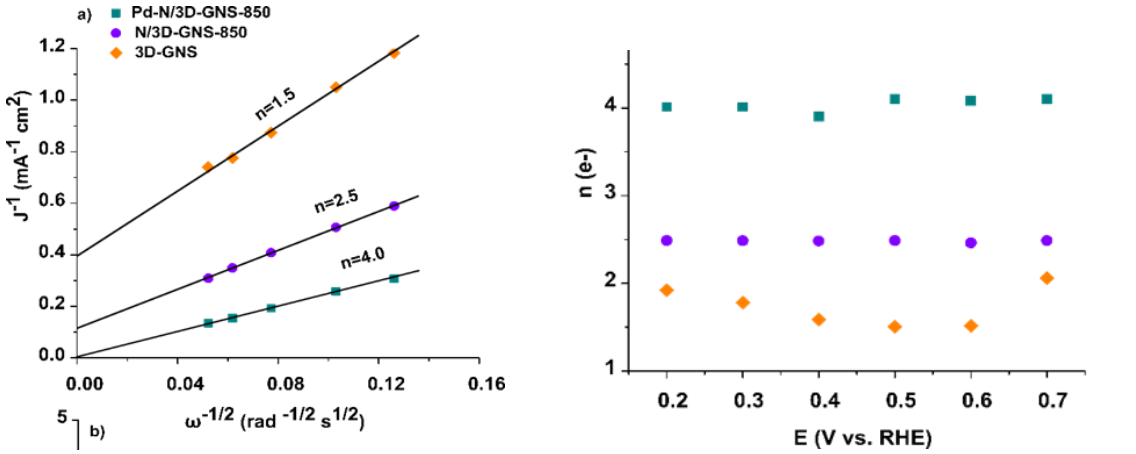

Figure 24. a) Koutecky–Levich plot of J^{-1} versus $\omega^{-1/2}$ obtained at 0.6 V for 3D-GNS, N/3D-GNS and Pd/N-3D-GNS at 0.6 V, the lines representing a linear regression. No. of electrons transferred between 0.7 and 0.2 V, estimated from K-L eqn.

The overall number of electrons transferred (n) at average fuel cell operating voltages of 0.6 V was estimated from the slopes of the K-L plots in Fig. 24a. While Pd-N/3D-GNS nanocomposite mostly catalysed the 4e- reduction of O_2 in alkaline media, the no. of

electrons transferred was estimated to be 2.5, and 1.5 for N/3D-GNS and 3D-GNS supports at 0.6 V. The overall no. of electrons transferred between 0.7 to 0.1 V was also estimated and plotted in Fig. 24b. Based on the results obtained using the rotating ring disc electrode voltammograms in Fig. 5a and overall no. of electrons transferred estimated from the K-L plots, it can be confirmed that:

(i) 3D-GNS support materials only catalysed the 2-electron reduction of oxygen to peroxide intermediates, i.e : $O_2 + H_2O + 2e^- \rightarrow HO_2^- + OH^-$, and were mainly responsible for peroxide generation;

(ii) N/3D-GNS catalysed the indirect 2x2 mixed electron reduction of peroxide, i.e.: $O_2 + H_2O + 2e^- \rightarrow HO_2^- + OH^-$ followed by $H_2O + HO_2^- + 2e^- \rightarrow 3OH$

(iii) and Pd-N/3D-GNS nanocomposites had enhanced electro kinetics and catalysed the direct 4-electron reduction reaction of O_2 to OH^- via the 4-electron mechanism, i.e $O_2 + 2H_2O + 4e^- \rightarrow 2H_2O$

Chapter 6

Performance of Pd/Graphene Nanocomposites in H_2/O_2 Fed Anion Exchange Membrane Fuel Cell

6.1 Ideal and Actual Fuel Cell Voltage/Current Characteristic

The ideal performance of a fuel cell is defined by its Nernst potential, represented as cell voltage.

$$E = E° + \left(\frac{RT}{2F}\right) \ln \left[\frac{P_{H_2}}{P_{H_2O}}\right] + \left(\frac{RT}{2F}\right) \ln \left[P_{O_2}^{1/2}\right]$$

Where E is equilibrium potential, E° is the standard potential, R is the universal gas constant, T is temperature, F is Faradays constant, and P is gas pressure.

The Nerst equation provides a relationship between the ideal standard potential (E□) for the cell reaction and the ideal equilibrium potential (E) at other temperatures and partial pressures of reactants and products. Once the ideal potential at standard conditions is known, the ideal voltage can be determined at other temperatures and pressures using these equations. According to the Nernst equation, the ideal cell potential at a given temperature can be increased by operating at higher reactant pressures, and improvements in fuel cell performance have, in fact, been observed at higher pressures.

Anode: $2H_2 + 4OH^- \rightarrow 4H_2O + 4e^-$, E = -0.828 V

Cathode: $O_2 + 2H_2O + 4e^- \rightarrow 4\ OH^-$, E = 0.401 V

Overall: $2H_2 + O_2 \rightarrow 2H_2O$, E = 1.23 V

The ideal standard potential of an H_2/O_2 fuel cell (E_o) is 1.229 volts with liquid water product. This value is shown in numerous chemistry texts as the oxidation potential of H_2. Useful amounts of work (electrical energy) are obtained from a fuel cell only when a reasonably current is drawn, but the actual cell potential is decreased from its equilibrium potential because of irreversible losses as shown in Figure 21. Several sources contribute to irreversible losses in a practical fuel cell. The losses, which are often called polarization, overpotential or overvoltage. originate primarily from three sources: (i) activation polarization, (ii) ohmic polarization and (iii) concentration polarization. These losses result in a cell voltage (V) for a fuel cell that is less than its ideal potential.

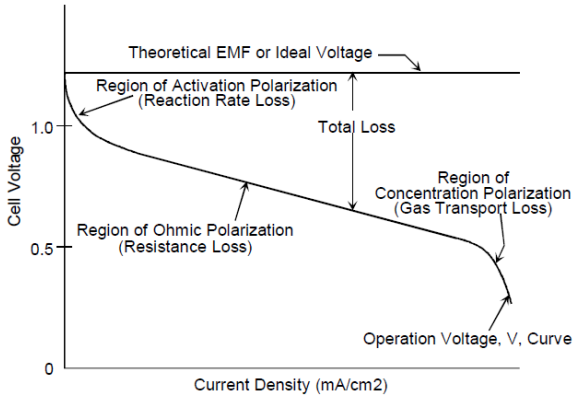

Figure 25. Ideal and Actual Fuel Cell Voltage/Current Characteristic

There are three regions of a polarization curve that contribute to the measured cell voltage:

1. **Activation Polarization:** The kinetic region between 1 to 0.8 V indicates the catalytic reaction efficiency. This region is also known Activation polarization is present when the rate of an electrochemical reaction at an electrode surface is controlled by sluggish electrode kinetics. In other words, activation polarization is directly related to the rates of electrochemical reactions. There is a close similarity

between electrochemical and chemical reactions in that both involve an activation barrier that must be overcome by the reacting species.

2. **Ohmic Polarization:** The ohmic region around 0.6 V indicates the ionic and electronic resistances in the cell. Ohmic losses occur because of resistance to the flow of ions in the electrolyte and resistance to flow of electrons through the electrode materials. The dominant ohmic losses, through the electrolyte, are reduced by decreasing the electrode separation and enhancing the ionic conductivity of the electrolyte. These resistances encompass all components including ionic resistance in the membrane, ionic and electronic resistance in the electrodes, and electronic resistance in the GDL and cell hardware.
3. **Concentration Polarization*:*** the region near 0.4 V indicates the efficiency of moving reactant gases and water to and from the active sites. a reactant is consumed at the electrode by electrochemical reaction, there is a loss of potential due to the inability of the surrounding material to maintain the initial concentration of the bulk fluid. That is, a concentration gradient is formed. Several processes may contribute to concentration polarization: slow diffusion in the gas phase in the electrode pores, solution/dissolution of reactants/products into/out of the electrolyte, or diffusion of reactants/products through the electrolyte to/from the electrochemical reaction site.

Although polarization curves cannot separate out individual microscopic phenomena occurring within the catalyst layer, they do provide enough information for performance comparison, provided they the polarization curves were obtained under the same operating

conditions. Pd-based catalysts have been investigated in direct liquid fuel cells such as Direct Ethanol fuel cells, Direct Formic Acid Fuel cells etc.[126] However, the number of research studies incorporating a Pd-based electrocatalysts in H_2/O_2 fed Anion Exchange Membrane Fuel Cells has been quite limited to date. Few studies that have focused or have done so, required to loading of Pd to be as high as 1.5 mg_{Pd} cm^{-2} and need alloying with other active metals such as Ni, Ru.[34, 127] Moreover, there are almost no reported literature on integrating porous graphene-like supports into a membrane electrode assembly for fuel cell testing, as most other groups have focused on optimizing commercial alkaline membranes using platinum as one or both electrodes.[125] In order to address these limitations, this chapter details the integration of Pd/Graphene composites in H_2/O_2 fed Anion Exchange Membrane Fuel Cell

6.2 Catalyst Coated Membrane Fabrication

6.2.1 Ink Formulation

Catalyst inks were prepared as follows: 65 wt.% of the anode and cathode catalysts, Pt/Carbon (50 wt% Pt on Carbon, Alfa Aesar) and Pd/3D-Graphene (30 wt% Pd on 3D-GNS)) respectively was mixed with 35 wt.% of the ionomer (Tokuyama® AS4) and isopropyl alcohol (catalyst concentration 50 mg mL^{-1}). The ionomer, catalyst powder and solvent was ball milled at 40 Hz for 30 mins in two 50 mL agate jars with 5 mm agate balls, followed by ultrasonication using a microtip for 10 minutes before deposition on the membrane.

6.2.2 Catalyst coated membrane fabrication

To prepare the CCM, a homogeneous mixture of the anode and cathode inks prepared in section 2.5.1 were then transferred to and sprayed by hand using a 0.3 mm nozzle air brush directly on the Tokuyama® A201 Anion Exchange Membrane with an active area of 5 cm^2. The membrane was held against a glass plate heated to 55°C using a Teflon gasket and the ink sprayed in very light layers alternating vertical and horizontal. Once the one side of electrode was sprayed it was allowed to dry before spraying the other side in the same fashion. AS4 content in the catalyst layers was 35 wt% and Pd/Pt loading was 0.25 mgPt/Pd cm^{-2} for both cathode and anode, respectively. The loaded CCM was then soaked in 3M KOH for 2 hours, followed by excessive rinsing in DI water.

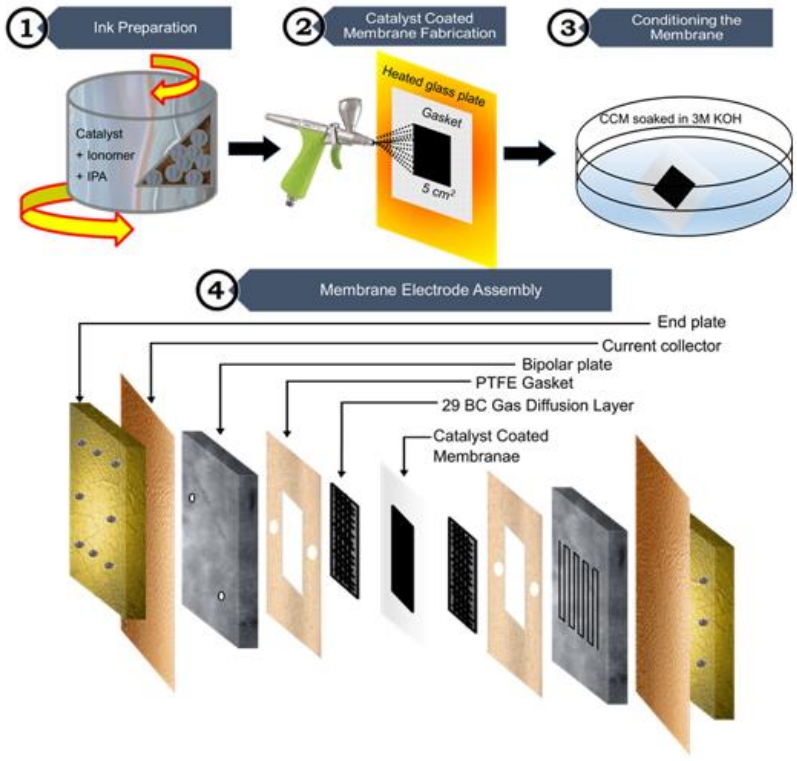

Figure 26 Fig. coated membrane fabrication and membrane electrode assembly.

6.3 Membrane Electrode Assembly (MEA)

Once the CCM electrodes were finished being rinsed, they were sandwiched between gas diffusion layers (GDLs) and polytetrafluoroethylene (PTFE) gaskets to make an MEA in the following order: 125 μm gasket, 29 BC Sigracet® GDL - CCM - 29 BC Sigracet® GDL - 125 μm gasket. The MEA was placed between two flow field plates with serpentine channels and assembled inside the cell hardware (Fuel Cell Technology Inc, 5 cm2) with bolts tightened to 40 inch-pounds and 4.4 Nm torque. The effective area of MEA was 5 cm2.

6.4 Fuel Cell Tests

For unit cell operations conducted in a Fuel Cell Technologies test station, hydrogen (H2) and oxygen (O2) were fully pre-humidified at 65°C and supplied to the cathode and anode at flow rates of 200 and 250 sccm, respectively. The cell operating temperature was maintained at 60 °C. The MEA in the cell was then activated by holding the cell potential at 0.3 V until the current was stable. Polarization curves were then obtained potientiostatically with a 30 second delay before data acquisition at 20 psi gauge back pressure.

6.5 MEA Performance: Amorphous vs Graphitized Support

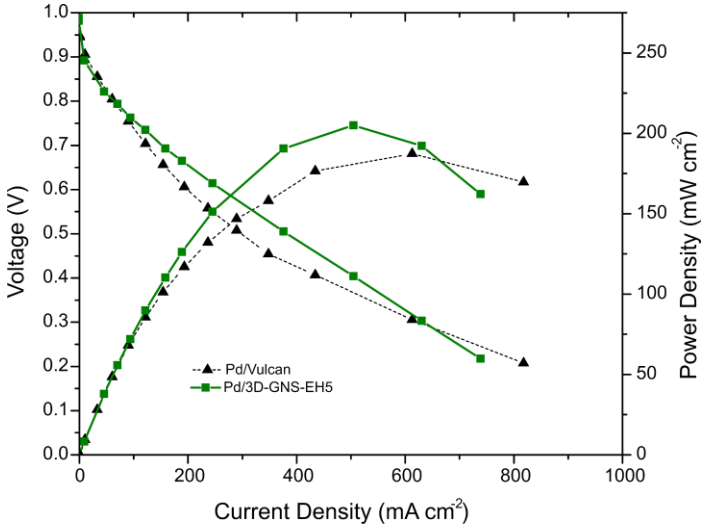

Figure 27. H_2/O_2 polarization and power density curves obtained at 60°C for Pd- 3D-GNS-EH5 and commercial Pd/Vulcan cathode catalysts in an Anion Exchange Membrane Fuel Cell.

Fig.27 shows the polarization curves of the Pd nanoparticles supported on thermally reduced 3D/Graphene nanosheets templated with EH5 (Pd/3D-GNS-EH5, Chapter 3) and compared to Pd nanoparticles supported on traditional Vulcan XC-72R amorphous carbon. Both the Pd-based catalysts were utilized as cathode catalysts (0.25 mg_{Pd} cm^{-2}), whereas Pt/C as anode catalysts (0.25 mg_{Pt} cm^{-2}). The fabrication and characterization and electrochemical comparison of these materials was discussed in Chapter 3.

As it can be seen in Fig 27, both the catalysts have similar onset potentials, indicating that the intrinsic activity of the Pd nanoparticle synthesized using SARM are similar. At current densities, lower than 100 mA cm^{-2}, the fuel cell performance dependence on support structure is not seen. However, at current densities above 100 mA cm^{-2}, the differences in performance of the Pd/Vulcan and Pd/3D-GNS-EH5 nanocomposites are clear. At conventional fuel cell operating voltages of 0.6 V, Pd/Vulcan had a current density of 193

mA cm^{-2}, whereas the current density of Pd/3D-GNS at 0.6 V is 246 mA cm^{-2}. Moreover, it can be seen that between 0.6 and 0.4 V, i.e. the Ohmic region, Pd/3D-GNS-EH5 performs significantly better in terms of reduced ohmic losses.

It is known that ohmic and electronic transport kinetics lies at the heart of energy conversion systems. The ohmic region around 0.6 V comprises losses from both ionic resist and electronic resistances in the membranes, electrodes, gas diffusion layer, cell hardware etc. It can be seen that between 0.6 and 0.4 V, i.e., the ohmic polarization region, Pd/3D-GNS performs significantly better in terms of reduced ohmic losses. Since the method of CCM fabrication, membrane conditioning and the type of GDL used were kept constant, the improvement in the ohmic region, to some extent, could be attributed to the increased graphitization and enhanced electronic properties of the nitrogen doped 3D-Graphene nanosheets.

Moreover, Pd/3D-GNS-EH5 has a maximum power density of 205 mW cm^{-2}, whereas Pd/Vulcan has a max power density of 189 mW cm^{-2}. Since all the related factors such as Pd loading (30 wt.%), Pd deposition using SARM, CCM fabrication and MEA assembly and operating conditions were maintained identical, the arising difference in performance can be attributed to the structural properties of the carbon supports.

6.6 MEA Performance: Microporous vs. Macroporous 3D-Graphene Support

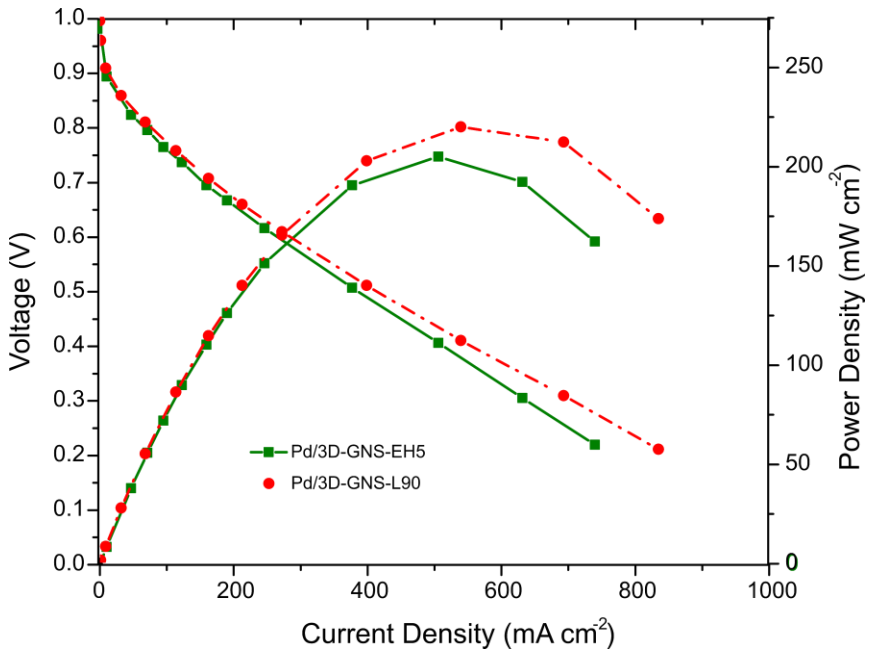

Figure 28. H_2/O_2 polarization and power density curves obtained at 60°C for Pd- 3D-GNS-EH5 and Pd/3D-GNS-L90 cathode catalysts in an Anion Exchange Membrane Fuel Cell.

Fig. 28 shows the polarization curves of Pd nanoparticles deposited on morphologically modified 3D-GNS supports, using two different sacrificial templates, EH5 and L90. The fabrication and characterization and electrochemical comparison of these materials was discussed in Chapter 4. Similar to Fig. 27, no substantial differences in the fuel cell performances were observed in the low current density region of 100 mA cm^{-2}, indicating similar intrinsic activities of the Pd nanoparticles deposited on the 3D-GNS supports. However, while Pd/3D-GNS-EH5 and Pd/3D-GNS-L90 show similar performances in the kinetic region and the ohmic region (1.0 t 0.6 V), the performance of Pd/3D-GNS-L90 in the mass transport-controlled region is higher than Pd/3D-GNS-EH5. At potential of 0.2V, electrode with Pd/3D-GNS-L90 has current density of 845 mA cm^{-2}, which is higher than that of Pd/3D-GNS-EH5 with 740 mA cm^{-2}. The maximum power densities obtained for

Pd/3D-GNS-L90 was 220 mW cm^{-2}, which is also higher than the maximum power density obtained with Pd/3D-GNS at 205 mW cm^{-2}. The difference in MEA performance could be arising mainly the mass transport of the reactant gas O_2 in morphologically modified 3D-GNS supports, as the surface chemistries (thermally reduced with 7at. % H_2) CCM fabrication and operating conditions were kept identical.

Since water consumed in the cathode layer of anion exchange membrane fuel cells according to the reactions: $O_2 + 2H_2O + 4e^- \rightarrow 4\ OH^-$, the provision of an efficient transport of reactants (O_2 and H_2O) in the cathode layer of AEMFCs is imperative. Since electrolytes tend to fill up the pores due to capillary action, larger sized macropores will facilitate on the dispersion of water and enhance the electroreduction of oxygen accordingly. Hence, the macropores in the templated 3D-GNS-L90 support can act as a bulk buffering reservoir for electrolytes to minimize the diffusion distances to the interior surfaces of the pores, and to create a 3-dimensional 3-phase reaction interface for both gas (O_2) liquid (H_2O) and electrocatalyst (Pd), Conversely, the decrease in performance of Pd/3D-GNS-EH5 may be due to the presence of a higher percentage of small micropores etched in the 3D-GNS structure with the EH5 sacrificial silica template. The lower performance could also be due to ineffective formation of triple-phase boundaries among metal catalyst, reactants, and AS4 ionomer, which is one of the critical factors for an effective MEA fabrication. Hence, a large percentage of micropores can ultimately decreases catalyst utilization and hinder the mass transport of reactants, leading to lower performance of Pd/3D-GNS-EH5 in comparison to Pd/3D-GNS-L90

6.6 MEA Performance: Pristine vs. Nitrogen Doped 3D-Graphene Support

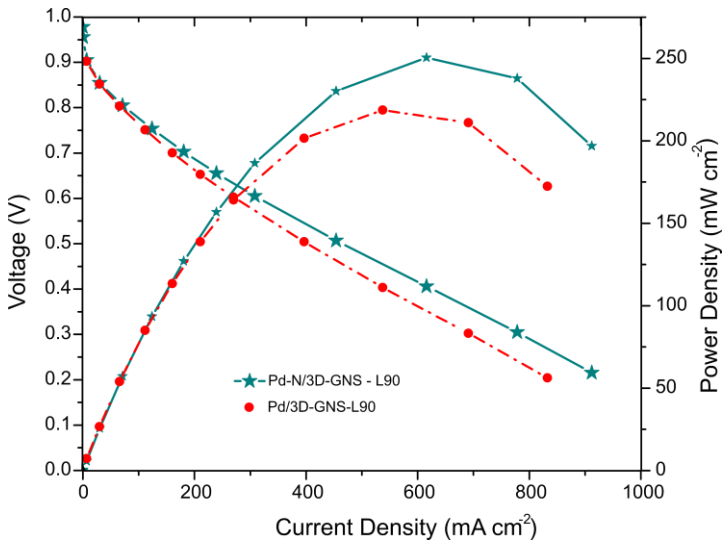

Figure 29. H_2/O_2 polarization and power density curves obtained at 60°C for Pd-N/3D-GNS-L90 and Pd/3D-GNS-L90 cathode catalysts in an Anion Exchange Membrane Fuel Cell.

Figure 29 compares the MEA performance of Pd nanoparticles deposited on nitrogen doped 3D graphene nanosheets that were modified with the L90 silica template, Pd-N/3D-GNS to the un-doped 3D-GNS-L90 support in Fig 28. The structure, chemistry and composition of these materials were discussed in Chapter 4 (Pd/3D-GNS-L90) and Chapter 5 (Pd-N/3D-GNS). As show earlier in Fig 28, Pd/3D-GNS-L90 support showed the higher performance due to its higher degree of macropores facilitating mass transport kinetics. However, as it can be seen from Fig. 24, nitrogen doping of the 3D-GNS-L90 support enhances MEA performance in both the ohmic and transport region. At the concentration polarization region, Pd-N/3D-GNS has the high current density of 912 mA cm^{-2}. In comparison, Pd/3D-GNS-L90 has a maximum power density of 220 mW cm^{-2}, where Pd nanoparticles deposited on the nitrogen doped graphene has a maximum power density of 250 mW cm^{-2}.

As discussed earlier in Chapter 4, nitrogen moieties can modify the electronic properties of graphene via conjugation of the π electrons. Nitrogen dopants can also provide additional active sites for oxygen reduction reactions. An improvement in the 3D-graphene supports conductivity as well as the availability of more oxygen reduction active sites could explain the improved MEA performance of the Pd-N/3D-GNS catalysts in AEMFCs.

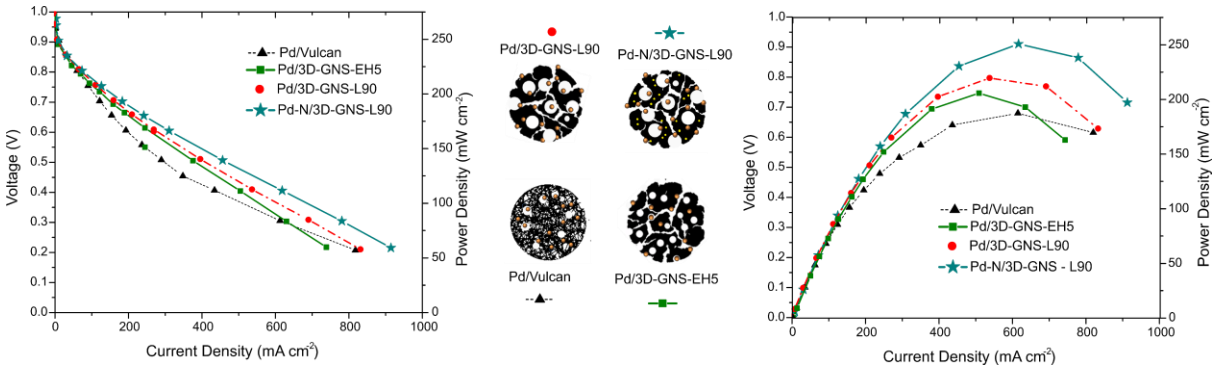

Figure 30. Polarization and power density curves obtained at 60°C for Pd-N/3D-GNS-L90, Pd/3D-GNS-L90, Pd/3D-GNS-EH5 and Pd/Vulcan cathode catalysts in an Anion Exchange Membrane Fuel Cell.

Figure 30 summarizes the performance the optimized Pd-based catalysts that were tested in AEMFCs in this study. The polarization graphs show that utilizing (i) graphitized supports can reduce ohmic losses in the MEA (3D-GNS-EH5) by increasing electrode conductivity, (ii) incorporating macropores into graphitized supports can facilitate mass transport kinetics (3D-GNS-L90), whereas (iii) doping macroporous graphitized supports with nitrogen (N/3D-GNS-L9) will can increase the performance by incorporating secondary ORR active sites. Hence, carbonaceous supports with different structure, surface functionalities and morphologies can play a non-trivial role in tuning the size, active surface area and electrochemical activity as well as performance of the Pd nanoparticles in AEMFCs.

Chapter 7

Conclusion

The development of catalytic materials is essential to activate the electrochemical reactions involved in low temperature fuel cells such as Anion Exchange Membrane Fuel Cell. This research provides a rational design strategy for fabricating high performance Pd/Graphene nanocomposite materials for catalyzing the oxygen reduction reactions in alkaline media, and AEMFCs and demonstrates how the morphological and chemical properties of graphitized supports can be modified to play a key role in improving oxygen electroreduction pathways not only in the alkaline electrolytes, but also in minimizing concentration polarization losses in operating AEMFCs.

While three dimensional carbonaceous materials have promising applications as electrode materials in fuel cells, their controlled fabrication and integration into fuel cells, especially in Anion Exchange Membrane Fuel Cells, have not been investigated in detail. This paper describes the highly scalable and cost effective fabrication process of designing porous nitrogen doped 3D-Graphene nanosheets using the Support Method. An interconnected network of pores was formed after removal of the sacrificial silica template that was embedded into the graphene's matrix. Doping of the 3D-GNS supports under NH_3 pyrolysis resulted in increased graphitization of the N/3D-GNS support and incorporation of 3.5 at% nitrogen. The Pd nanoparticles deposited using the surfactant-free Soft Alcohol Reduction Method had a highly crystalline FCC structure

By modifying the surface chemistry of the 3D-graphene nanosheets using chemical and thermal reduction techniques, developed in this study, it was shown that

(1) the Pd nanoparticles attained better dispersion: TEM and SEM surface analysis of the catalysts showed that the 3D-Graphene supports lead to a higher dispersion of Pd nanoparticles on its surface, whereas Vulcan led the Pd nanoparticles to agglomerate.

(ii) the electrochemically accessible surface area of the Pd nanoparticles increased by at least 30%, the half-wave potential of catalyst shifted positively by ~50 mV, and significant increase in current densities.

The results obtained using the surface analysis and electrochemical studies tell us that the influence of the structure's morphology on electrochemical and fuel cell performances could be quite important. The potentiodynamic studies also confirmed that the electrocatalytic performance of the Pd-Graphene nanocomposites was dependent on the porosity of the morphologically modified 3D graphene nanosheets. Palladium nanoparticles that were deposited on 3D-Graphene supports that were templated to have a higher degree of macroporosity (>50 nm pore size) exhibited superior electrocatalytic activity in terms of the highest limiting current densities, lower peroxide (HO_2^-) yields and direct 4e- reduction of oxygen in alkaline media. On the contrary, Pd nanoparticles that were deposited on 3D-graphene nanosheets templated had a higher density micro-pores <2 nm and showed lower performance, in terms of lower limiting currents and higher hydroperoxyl generation. These results indicated that the surface area of macropores plays an important role in a facilitating the diffusion of oxygen and electrolyte into the active sites, as well as inhibiting peroxide generation by re-adsorbing the peroxide intermediates into its porous matrix and reducing it further. Hence, instead of aiming to designing graphitized supports with higher BET surface areas for fuel cell electrocatalysts, it might be noteworthy take the pore size distribution of the supports into consideration as well.

Moreover, the results from this study also show that it is crucial understand the function of nitrogen moieties while design nitrogen-functionalized graphene or other carbon composites for the targeted incorporation of appropriate nitrogen moieties that can facilitate ORR kinetics. While investigating the role of three major nitrogen moieties: graphitic-, hydrogenated- and pyridinic-N - in modifying oxygen electroreduction kinetics and performance of nitrogen doped graphene sheets in alkaline medias using a combination of spectroscopic and potentiodynamic techniques, it was established that that different nitrogen moieties play different roles during ORR. It was observed that an increase in graphitic-N moieties can lower onset and/or half wave potential and generate significant amounts of hydrogen peroxide, where as an increase in hydrogenated-N can boost limiting current densities and pyridinic-N moieties reduce peroxide generation by acting as the second active site. Among all the three samples, the optimal doping temperature was determined to be 850°C, as this temperature gives rise to the highest ratio of hydrogenated-N to pyridinic-N.

The superior performance of Pd-N/3D-GNS was also clearly demonstrated when utilized as cathode catalysts in H_2/O_2 fed AEMFCs. Owing to its novel morphological templated porous feature and the desirable chemical composition of nitrogen moieties, the Pd-N/3D-GNS catalysts exhibits much enhanced performance as an cathode materials for AEMFCs by facilitating mass transport kinetics and modifying the supports electronic properties through nitrogen doping. When compared to the performance of Pd nanoparticles deposited on Vulcan, the Pd-N/3D-GNS nanocomposites showed twice as high current densities in the ohmic region (308 mA cm^{-2}) as well as concentration polarization region (912 mA cm^{-2}). Based on the tests conducted H_2/O_2 fed AEMFC, it was found that

utilizing nitrogen doped graphene sheets with a macroporous three dimensional morphology can significantly improve performance by facilitating charge transfer through its highly conductive carbon matrix and enhance mass transport kinetics by buffering reservoir for electrolytes to minimize the diffusion distances to the interior surfaces of the macropores by creating a 3-dimensional 3-phase reaction interface for both gas (O_2) liquid (H_2O) and electrocatalyst (Pd). The power density of 250 mW cm^{-2} obtained from the Pd-N/3D-GNS nanocomposites was not only also significantly higher than Pd/Vulcan (189 mW cm^{-2}) – but is also one of the highest achieved for graphene supported nanocomposites and low Pd loadings in AEMFCs.

Overall, this work not only provides a synthetic procedure for constructing novel 3D graphene nano structures with varying levels of porosity and surface chemistries, but also analyzes how modifying the morphology and chemical composition of graphitized supports can play a key role in facilitating oxygen electroreduction in Anion Exchange Membrane Fuel Cells. The results from this study will not only contribute towards the development of highly active ORR electrocatalysts for energy conversion devices such as AEMFCs, but can also be expanded to other energy storage and conversion applications such as electrodes for Li-air batteries and electrolyzers.

List of Journal Publications

Book Chapter:

1. **S. Kabir**, A. Serov, "Anodic Materials for Electrooxidation of Alcohols in Alkaline Media", Electrochemistry: Volume 14, 2017, 14, pp. P006-P010, DOI: 10.1039/9781782622727-00061, eISBN:978-1-78262-272-7

Patent:

2. **S. Kabir**, S. Stariha, A. Serov and P. Atanassov, "Method of Preparation of Nano-sized Materials and Apparatus Incorporating the Same", International Application No.: PCT/US2015/030555, Filed on May 13, 2015.

Journal Papers:

3. A. Perry, **S. Kabir**, M. S. Chavez, I. Matanovic, S. Babanova, A. Serov, and P. Atanassov, Novel Hybrid Catalyst for the Oxidation of Organic Acids: Pd Nanoparticles Supported on Mn-N-3D-graphene Nanosheets, ChemElectroChem. DOI: 10.1002/celc.201700285
4. **S. Kabir**, A. Zadick, P. Atanassov, L. Dubaua, M. Chatenet, Stability of Carbon-Supported Palladium Nanoparticles in Alkaline Media: A Case Study of Graphitized and More Amorphous Supports, *Electrochemistry Communications*, 2017. http://dx.doi.org/10.1016/j.elecom.2017.03.017
5. **S. Kabir**, A. Serov, A. Zadick, K. Artyushkova, P. Atanassov, "Palladium Nanoparticles Supported on 3D-Graphene Nanosheets: Superior Cathode Electrocatalysts", *ChemElectroChem*, 2016, DOI: 10.1002/celc.201600245.

6. **S. Kabir**, A. Serov, P. Atanassov, "Palladium Nanoparticles Supported on 3D-Graphene Nanosheets for Oxygen Reduction Reactions in Alkaline Media", *ECS Transactions*, 72(29):39-47, 2016. DOI: 10.1149/07229.0039ecst.
7. **S. Kabir**, A. Serov, K. Artyushkova and P. Atanassov, "Design of Novel Graphene Materials as a Support for Palladium Nanoparticles: Highly Active Catalysts Towards Ethanol Electrooxidation", *Electrochimica Acta*, 203: 144-153, 2016. http://dx.doi.org/10.1016/j.electacta.2016.04.026.
8. **S. Kabir**, K. Artyushkova, A. Serov and P. Atanassov, "Binding Energy Shifts for Nitrogen-containing Graphene-Based Electrocatalysts - Experiments and DFT Calculations", *Surface and Interface Analysis*, 48: 290–297, 2016. DOI 10.1002/sia.5935
9. **S. Kabir**, K. Artyushkova, B. Kiefer and P. Atanassov, "Computational and Experimental Evidence for a New TM-N3/C Moiety Family in Non-PGM Electrocatalysts", *Physical Chemistry Chemical Physics*, 17: 17785-17789, 2016. DOI: 10.1039/C5CP02230D
10. A. Serov, N.I. Andersen, **S. Kabir**, A. Roy, T. Asset, M. Chatenet, F. Maillard and P. Atanassov, "Palladium Supported on 3D Graphene as an Active Catalyst for Alcohols Electrooxidation", *Journal of The Electrochemical Society*, 162: F1305-F1309, 2015. DOI: 10.1149/2.0301512jes
11. C. Santoro, F. Soavi, C. Arbizzani, A. Serov, **S. Kabir**, K. Carpenter, O. Bretschger, P. Atanassov, "Co-Generation of Hydrogen and Power/Current Pulses From Supercapacitive MFCs using Novel HER Iron-based Catalysts,

Electrochimica Acta, 220: 672–682, 2016. http://dx.doi.org/10.1016/j.electacta.2016.10.154

12. M. Kodali, C. Santoro, A. Serov, **S. Kabir**, K. Artyushkova, I. Matanovic, P. Atanassov, "Air Breathing Cathodes for Oxygen Reduction Reaction in Microbial Fuel Cell using Mn-AAPyr, Fe-AAPyr, Co-AAPyr and Ni-AAPyr PGM-free Catalysts", *Electrochimica Acta*, 231: 115-124, 2016. http://dx.doi.org/10.1016/j.electacta.2017.02.033
13. C. Santoro, M. Kodali, **S. Kabir**, F. Soavi, A. Serov, P. Atanassov, Three-Dimensional Graphene Nanosheets as Cathode Catalysts in Standard and Supercapacitive Microbial Fuel Cell, *Journal of Power Sources*, 2017. DOI: 10.1016/j.jpowsour.2017.03.135

References

1. L. Carrette, K. A. Friedrich and U. Stimming, *Fuel Cells*, 2001, **1**, 5-39.
2. C. E. Thomas, *Int J Hydrogen Energ*, 2009, **34**, 6005-6020.
3. *Fuel Cells Bulletin*, 2010, **2010**, 9-10.
4. *Fuel Cells Bulletin*, 2014, **2014**, 5.
5. M. Warshay and P. R. Prokopius, *J Power Sources*, 1990, **29**, 193-200.
6. C. Wang, N. M. Markovic and V. R. Stamenkovic, *ACS Catalysis*, 2012, **2**, 891-898.
7. J. Greeley, I. E. L. Stephens, A. S. Bondarenko, T. P. Johansson, H. A. Hansen, T. F. Jaramillo, J. Rossmeisl, I. Chorkendorff and J. K. Norskov, *Nat Chem*, 2009, **1**, 552-556.
8. H. A. Gasteiger, S. S. Kocha, B. Sompalli and F. T. Wagner, *Appl Catal B-Environ*, 2005, **56**, 9-35.
9. I. Katsounaros, S. Cherevko, A. R. Zeradjanin and K. J. J. Mayrhofer, *Angewandte Chemie International Edition*, 2014, **53**, 102-121.
10. Y. Shao-Horn, W. Sheng, S. Chen, P. Ferreira, E. Holby and D. Morgan, *Topics in Catalysis*, 2007, **46**, 285-305.
11. B. C. H. Steele and A. Heinzel, *Nature*, 2001, **414**, 345-352.
12. R. Bashyam and P. Zelenay, *Nature*, 2006, **443**, 63-66.
13. M. Shao, A. Peles and K. Shoemaker, *Nano Letters*, 2011, **11**, 3714-3719.

14. R. Borup, J. Meyers, B. Pivovar, Y. S. Kim, R. Mukundan, N. Garland, D. Myers, M. Wilson, F. Garzon, D. Wood, P. Zelenay, K. More, K. Stroh, T. Zawodzinski, J. Boncella, J. E. McGrath, M. Inaba, K. Miyatake, M. Hori, K. Ota, Z. Ogumi, S. Miyata, A. Nishikata, Z. Siroma, Y. Uchimoto, K. Yasuda, K.-i. Kimijima and N. Iwashita, *Chemical Reviews*, 2007, **107**, 3904-3951.

15. Z.-Y. Zhou, Q. Wang, J.-L. Lin, N. Tian and S.-G. Sun, *Electrochimica Acta*, 2010, **55**, 7995-7999.

16. S. Sharma and B. G. Pollet, *Journal of Power Sources*, 2012, **208**, 96-119.

17. L. Castanheira, W. O. Silva, F. H. B. Lima, A. Crisci, L. Dubau and F. Maillard, *ACS Catalysis*, 2015, **5**, 2184-2194.

18. H. A. Gasteiger, S. S. Kocha, B. Sompalli and F. T. Wagner, *Applied Catalysis B: Environmental*, 2005, **56**, 9-35.

19. J. C. Meier, C. Galeano, I. Katsounaros, J. Witte, H. J. Bongard, A. A. Topalov, C. Baldizzone, S. Mezzavilla, F. Schüth and K. J. J. Mayrhofer, *Beilstein Journal of Nanotechnology*, 2014, **5**, 44-67.

20. C. A. Rice, P. Urchaga, A. O. Pistono, B. W. McFerrin, B. T. McComb and J. Hu, *Journal of The Electrochemical Society*, 2015, **162**, F1175-F1180.

21. C. Song and J. Zhang, in *PEM Fuel Cell Electrocatalysts and Catalyst Layers*, ed. J. Zhang, Springer London, 2008, ch. 2, pp. 89-134.

22. H. Tang, Z. Qi, M. Ramani and J. F. Elter, *Journal of Power Sources*, 2006, **158**, 1306-1312.

23. J. R. Varcoe, P. Atanassov, D. R. Dekel, A. M. Herring, M. A. Hickner, P. A. Kohl, A. R. Kucernak, W. E. Mustain, K. Nijmeijer, K. Scott, T. Xu and L. Zhuang, *Energy & Environmental Science*, 2014, **7**, 3135-3191.

24. J. R. Varcoe, M. Beillard, D. M. Halepoto, J. P. Kizewski, S. Poynton and R. C. T. Slade, *ECS Transactions*, 2008, **16**, 1819-1834.

25. J. R. Varcoe and R. C. T. Slade, *Fuel Cells*, 2005, **5**, 187-200.

26. J. R. Varcoe, P. Atanassov, D. R. Dekel, A. M. Herring, M. A. Hickner, P. A. Kohl, A. R. Kucernak, W. E. Mustain, K. Nijmeijer, K. Scott, T. Xu and L. Zhuang, *Energy & Environmental Science*, 2014, **7**, 3135-3191.

27. M. A. Hickner, A. M. Herring and E. B. Coughlin, *Journal of Polymer Science Part B: Polymer Physics*, 2013, **51**, 1727-1735.

28. Y. Wang, L. Li, L. Hu, L. Zhuang, J. Lu and B. Xu, *Electrochemistry Communications*, 2003, **5**, 662-666.

29. M. Pourbaix, National Association of Corrosion Engineers, Houston, 1979, p. 453.

30. M. Chatenet, M. Aurousseau, R. Durand and F. Andolfatto, *J. Electrochem. Soc.*, 2003, **150**, D47-D55.

31. M. Chatenet, L. Génies-Bultel, M. Aurousseau, R. Durand and F. Andolfatto, *J. Appl. Electrochem.*, 2002, **32**, 1131-1140.

32. I. Roche, E. Chainet, M. Chatenet and J. Vondrak, *J. Phys. Chem. C*, 2007, **111**, 1434-1443.

33. V. Di Noto, E. Negro, S. Lavina, S. Gross and G. Pace, *Electrochim Acta*, 2007, **53**, 1604-1617.

34. M. Alesker, M. Page, M. Shviro, Y. Paska, G. Gershinsky, D. R. Dekel and D. Zitoun, *J. Power Sources*, 2016, **304**, 332-339.

35. H. A. Miller, F. Vizza, M. Marelli, A. Zadick, L. Dubau, M. Chatenet, S. Geiger, S. Cherevko, H. Doan, R. K. Pavlicek, S. Mukerjee and D. R. Dekel, *Nano Energy*.

36. A. Serov, U. Martinez and P. Atanassov, *Electrochem. Commun.*, 2013, **34**, 185-188.

37. U. Martinez, A. Serov, M. Padilla and P. Atanassov, *ChemSusChem*, 2014, **7**, 2351-2357.

38. A. Zalineeva, A. Serov, M. Padilla, U. Martinez, K. Artyushkova, S. Baranton, C. Coutanceau and P. Atanassov, *Electrochem. Commun.*, 2015, **57**, 48-51.

39. A. Zalineeva, A. Serov, M. Padilla, U. Martinez, K. Artyushkova, S. Baranton, C. Coutanceau and P. B. Atanassov, *Appl. Catal. B: Environmental*, 2015, **176-177**, 429-435.

40. A. Serov, T. Asset, M. Padilla, I. Matanovic, U. Martinez, A. Roy, K. Artyushkova, M. Chatenet, F. Maillard, D. Bayer, C. Cremers and P. Atanassov, *Appl. Catal. B: Environmental*, 2016, **191**, 76-85.

41. P.-Y. Olu, F. Deschamps, G. Caldarella, M. Chatenet and N. Job, *J. Power Sources*, 2015, **297**, 492-503.

42. A. M. Pasqualeti, P. Y. Olu, M. Chatenet and F. H. B. Lima, *ACS Catal.*, 2015, **5**, 2778-2787.

43. P.-Y. Olu, N. Job and M. Chatenet, *J. Power Sources*, 2016, **327**, 235-257.

44. P.-Y. Olu, A. Zadick, N. Job and M. Chatenet, in *Fuel Cell - Electrocatalysis*, eds. T. Maiyalagan and S. S. Viswanathan, Wiley-VCH, New York, 2016, vol. in press, ch. 9.

45. U. Martinez, K. Asazawa, B. Halevi, A. Falase, B. Kiefer, A. Serov, M. Padilla, T. Olson, A. Datye, H. Tanaka and P. Atanassov, *Phys Chem Chem Phys*, 2012, **14**, 5512-5517.

46. T. Sakamoto, K. Asazawa, J. Sanabria-Chinchilla, U. Martinez, B. Halevi, P. Atanassov, P. Strasser and H. Tanaka, *J. Power Sources*, 2014, **247**, 605-611.

47. T. Asset, A. Roy, T. Sakamoto, M. Padilla, I. Matanovic, K. Artyushkova, A. Serov, F. Maillard, M. Chatenet, K. Asazawa, H. Tanaka and P. Atanassov, *Electrochim. Acta*, 2016, **215**, 420-426.

48. D. Tang, J. Pan, S. Lu, L. Zhuang and J. Lu, *Science China Chemistry*, 2010, **53**, 357-364.

49. A. Zadick, L. Dubau, N. Sergent, G. Berthomé and M. Chatenet, *ACS Catalysis*, 2015, **5**, 4819-4824.

50. J. Prakash and H. Joachin, *Electrochimica Acta*, 2000, **45**, 2289-2296.

51. J. Guo, A. Hsu, D. Chu and R. Chen, *The Journal of Physical Chemistry C*, 2010, **114**, 4324-4330.

52. Y. Liang, H. Wang, P. Diao, W. Chang, G. Hong, Y. Li, M. Gong, L. Xie, J. Zhou, J. Wang, T. Z. Regier, F. Wei and H. Dai, *Journal of the American Chemical Society*, 2012, **134**, 15849-15857.

53. H. Erikson, A. Sarapuu, J. Solla-Gullón and K. Tammeveski, *Journal of Electroanalytical Chemistry*, 2016, **780**, 327-336.

54. E. Antolini, *Energy & Environmental Science*, 2009, **2**, 915-931.

55. S. Kabir and A. Serov, in *Electrochemistry: Volume 14*, The Royal Society of Chemistry, 2017, vol. 14, pp. 61-101.

56. H. Erikson, A. Sarapuu, N. Alexeyeva, K. Tammeveski, J. Solla-Gullón and J. M. Feliu, *Electrochimica Acta*, 2012, **59**, 329-335.

57. M. Shao, J. Odell, M. Humbert, T. Yu and Y. Xia, *The Journal of Physical Chemistry C*, 2013, **117**, 4172-4180.

58. M. H. Seo, S. M. Choi, H. J. Kim and W. B. Kim, *Electrochemistry Communications*, 2011, **13**, 182-185.

59. L. Jiang, A. Hsu, D. Chu and R. Chen, *Journal of The Electrochemical Society*, 2009, **156**, B643-B649.

60. S. Kabir, A. Serov, A. Zadick, K. Artyushkova and P. Atanassov, *ChemElectroChem*, 2016, n/a-n/a.

61. F. H. B. Lima, J. Zhang, M. H. Shao, K. Sasaki, M. B. Vukmirovic, E. A. Ticianelli and R. R. Adzic, *The Journal of Physical Chemistry C*, 2007, **111**, 404-410.

62. A. Serov, T. Nedoseykina, O. Shvachko and C. Kwak, *Journal of Power Sources*, 2010, **195**, 175-180.

63. L. Jiang, A. Hsu, D. Chu and R. Chen, *Electrochimica Acta*, 2010, **55**, 4506-4511.

64. M. Wang, W. Zhang, J. Wang, D. Wexler, S. D. Poynton, R. C. T. Slade, H. Liu, B. Winther-Jensen, R. Kerr, D. Shi and J. Chen, *ACS Applied Materials & Interfaces*, 2013, **5**, 12708-12715.

65. B. Li and J. Prakash, *Electrochemistry Communications*, 2009, **11**, 1162-1165.

66. N. Alexeyeva, A. Sarapuu, K. Tammeveski, F. J. Vidal-Iglesias, J. Solla-Gullón and J. M. Feliu, *Electrochimica Acta*, 2011, **56**, 6702-6708.

67. M. Arenz, T. J. Schmidt, K. Wandelt, P. N. Ross and N. M. Markovic, *The Journal of Physical Chemistry B*, 2003, **107**, 9813-9819.

68. A. Zadick, L. Dubau, U. B. Demirci and M. Chatenet, *Journal of The Electrochemical Society*, 2016, **163**, F781-F787.

69. H. Dai, Y. L. Chen, Y. Y. Lin, G. F. Xu, C. P. Yang, Y. J. Tong, L. H. Guo and G. N. Chen, *Electrochimica Acta*, 2012, **85**, 644-649.

70. E. Antolini and E. R. Gonzalez, *Solid State Ionics*, 2009, **180**, 746-763.

71. A. K. Geim and K. S. Novoselov, *Nat Mater*, 2007, **6**, 183-191.

72. Y. Zhu, S. Murali, W. Cai, X. Li, J. W. Suk, J. R. Potts and R. S. Ruoff, *Advanced Materials*, 2010, **22**, 3906-3924.

73. M. Liu, R. Zhang and W. Chen, *Chemical Reviews*, 2014, **114**, 5117-5160.

74. H. Bai, C. Li and G. Shi, *Advanced Materials*, 2011, **23**, 1089-1115.

75. P. Pasanen, M. Voutilainen, M. Helle, X. F. Song and P. J. Hakonen, *Phys Scripta*, 2012, **T146**.

76. A. K. Geim and K. S. Novoselov, *Nat Mater*, 2007, **6**, 183-191.

77. Y. Lu, Y. Jiang, H. Wu and W. Chen, *The Journal of Physical Chemistry C*, 2013, **117**, 2926-2938.

78. Y. Lu, Y. Jiang and W. Chen, *Nanoscale*, 2014, **6**, 3309-3315.

79. V. Bambagioni, C. Bianchini, A. Marchionni, J. Filippi, F. Vizza, J. Teddy, P. Serp and M. Zhiani, *Journal of Power Sources*, 2009, **190**, 241-251.

80. F. Zhu, G. Ma, Z. Bai, R. Hang, B. Tang, Z. Zhang and X. Wang, *Journal of Power Sources*, 2013, **242**, 610-620.

81. A. N. Geraldes, D. Furtunato da Silva, J. C. Martins da Silva, O. Antonio de Sá, E. V. Spinacé, A. O. Neto and M. Coelho dos Santos, *Journal of Power Sources*, 2015, **275**, 189-199.

82. L. Truong-Phuoc, C. Pham-Huu, V. Da Costa and I. Janowska, *Chemical Communications*, 2014, **50**, 14433-14435.

83. X. Ge, A. Sumboja, D. Wuu, T. An, B. Li, F. W. T. Goh, T. S. A. Hor, Y. Zong and Z. Liu, *ACS Catalysis*, 2015, **5**, 4643-4667.

84. Q. Zhang, Z. Bai, M. Shi, L. Yang, J. Qiao and K. Jiang, *Electrochimica Acta*, 2015, **177**, 113-117.

85. J. Sun, Y. H. Fang and Z. P. Liu, *Phys Chem Chem Phys*, 2014, **16**, 13733-13740.

86. S. Kattel and G. F. Wang, *J Phys Chem Lett*, 2014, **5**, 452-456.

87. Y. Zhang, J. Ge, L. Wang, D. Wang, F. Ding, X. Tao and W. Chen, *Sci Rep-Uk*, 2013, **3**, 2771.

88. A. Titov, P. Zapol, P. Kral, D. J. Liu, H. Iddir, K. Baishya and L. A. Curtiss, *J Phys Chem C*, 2009, **113**, 21629-21634.

89. D. Higgins, M. A. Hoque, M. H. Seo, R. Wang, F. Hassan, J.-Y. Choi, M. Pritzker, A. Yu, J. Zhang and Z. Chen, *Advanced Functional Materials*, 2014, **24**, 4325-4336.

90. S. Kattel, P. Atanassov and B. Kiefer, *J Mater Chem A*, 2014, **2**, 10273-10279.

91. S. R. Stoyanov, A. V. Titov and P. Kral, *Coordin Chem Rev*, 2009, **253**, 2852-2871.

92. D. He, Y. Jiang, H. Lv, M. Pan and S. Mu, *Applied Catalysis B: Environmental*, 2013, **132–133**, 379-388.

93. C.-L. Sun, J.-S. Tang, N. Brazeau, J.-J. Wu, S. Ntais, C.-W. Yin, H.-L. Chou and E. A. Baranova, *Electrochimica Acta*, 2015, **162**, 282-289.

94. P. Wu, Y. Huang, L. Zhou, Y. Wang, Y. Bu and J. Yao, *Electrochimica Acta*, 2015, **152**, 68-74.

95. K. N. Wood, R. O'Hayre and S. Pylypenko, *Energ Environ Sci*, 2014, **7**, 1212-1249.

96. W. J. Lee, U. N. Maiti, J. M. Lee, J. Lim, T. H. Han and S. O. Kim, *Chemical Communications*, 2014, **50**, 6818-6830.

97. S. Kabir, K. Artyushkova, B. Kiefer and P. Atanassov, *Physical Chemistry Chemical Physics*, 2015, **17**, 17785-17789.

98. S. Kabir, K. Artyushkova, A. Serov, B. Kiefer and P. Atanassov, *Surface and Interface Analysis*, 2016.

99. S. Kabir, K. Artyushkova, A. Serov, B. Kiefer and P. Atanassov, *Surface and Interface Analysis*, 2016, n/a-n/a.

100. K. Artyushkova, B. Kiefer, B. Halevi, A. Knop-Gericke, R. Schlogl and P. Atanassov, *Chem Commun*, 2013, **49**, 2539-2541.

101. Y. Y. Shao, S. Zhang, M. H. Engelhard, G. S. Li, G. C. Shao, Y. Wang, J. Liu, I. A. Aksay and Y. H. Lin, *J Mater Chem*, 2010, **20**, 7491-7496.

102. J. R. Pels, F. Kapteijn, J. A. Moulijn, Q. Zhu and K. M. Thomas, *Carbon*, 1995, **33**, 1641-1653.

103. Y. Chen, J. Wang, H. Liu, R. Li, X. Sun, S. Ye and S. Knights, *Electrochemistry Communications*, 2009, **11**, 2071-2076.

104. K. Jukk, N. Kongi, L. Matisen, T. Kallio, K. Kontturi and K. Tammeveski, *Electrochimica Acta*, 2014, **137**, 206-212.

105. F. Su, Z. Tian, C. K. Poh, Z. Wang, S. H. Lim, Z. Liu and J. Lin, *Chemistry of Materials*, 2010, **22**, 832-839.

106. G. Liu, X. G. Li, P. Ganesan and B. N. Popov, *Electrochim Acta*, 2010, **55**, 2853-2858.

107. K. Prehn, A. Warburg, T. Schilling, M. Bron and K. Schulte, *Compos Sci Technol*, 2009, **69**, 1570-1579.

108. A. Q. Zhao, J. Masa, M. Muhler, W. Schuhmann and W. Xia, *Electrochim Acta*, 2013, **98**, 139-145.

109. L. Zhang and Z. Xia, *The Journal of Physical Chemistry C*, 2011, **115**, 11170-11176.

110. S. Maldonado and K. J. Stevenson, *The journal of physical chemistry. B*, 2005, **109**, 4707-4716.

111. J. Zhu, M. Xiao, X. Zhao, C. Liu, J. Ge and W. Xing, *Nano Energy*, 2015, **13**, 318-326.

112. L. Perini, C. Durante, M. Favaro, V. Perazzolo, S. Agnoli, O. Schneider, G. Granozzi and A. Gennaro, *ACS Applied Materials & Interfaces*, 2015, **7**, 1170-1179.

113. Y. Ma, L. Sun, W. Huang, L. Zhang, J. Zhao, Q. Fan and W. Huang, *The Journal of Physical Chemistry C*, 2011, **115**, 24592-24597.

114. Z.-S. Wu, A. Winter, L. Chen, Y. Sun, A. Turchanin, X. Feng and K. Müllen, *Advanced Materials*, 2012, **24**, 5130-5135.

115. Z.-L. Wang, D. Xu, H.-G. Wang, Z. Wu and X.-B. Zhang, *ACS Nano*, 2013, **7**, 2422-2430.

116. D. Wei, Y. Liu, Y. Wang, H. Zhang, L. Huang and G. Yu, *Nano Letters*, 2009, **9**, 1752-1758.

117. Z. Lin, G. Waller, Y. Liu, M. Liu and C.-P. Wong, *Advanced Energy Materials*, 2012, **2**, 884-888.

118. Y. Zhu, S. Murali, M. D. Stoller, A. Velamakanni, R. D. Piner and R. S. Ruoff, *Carbon*, 2010, **48**, 2118-2122.

119. C.-Y. Su, A.-Y. Lu, Y. Xu, F.-R. Chen, A. N. Khlobystov and L.-J. Li, *ACS Nano*, 2011, **5**, 2332-2339.

120. S. Stankovich, D. A. Dikin, G. H. B. Dommett, K. M. Kohlhaas, E. J. Zimney, E. A. Stach, R. D. Piner, S. T. Nguyen and R. S. Ruoff, *Nature*, 2006, **442**, 282-286.

121. M. Endo, K. Takeuchi, T. Hiraoka, T. Furuta, T. Kasai, X. Sun, C. H. Kiang and M. S. Dresselhaus, *Journal of Physics and Chemistry of Solids*, 1997, **58**, 1707-1712.

122. H. Dong, C. Liu, H. Ye, L. Hu, B. Fugetsu, W. Dai, Y. Cao, X. Qi, H. Lu and X. Zhang, *Scientific Reports*, 2015, **5**, 17542.

123. S. Han, D. Wu, S. Li, F. Zhang and X. Feng, *Advanced Materials*, 2014, **26**, 849-864.

124. X. Huang, K. Qian, J. Yang, J. Zhang, L. Li, C. Yu and D. Zhao, *Advanced Materials*, 2012, **24**, 4419-4423.

125. M. Carmo, G. Doubek, R. C. Sekol, M. Linardi and A. D. Taylor, *Journal of Power Sources*, 2013, **230**, 169-175.

126. A. Brouzgou, A. Podias and P. Tsiakaras, *Journal of Applied Electrochemistry*, 2013, **43**, 119-136.

127. T. Fujigaya, C. Kim, K. Matsumoto and N. Nakashima, *ChemPlusChem*, 2014, **79**, 400-405.

128. J. Chen, B. Yao, C. Li and G. Shi, *Carbon*, 2013, **64**, 225-229.

129. A. Serov, K. Artyushkova, N. I. Andersen, S. Stariha and P. Atanassov, *Electrochimica Acta*, 2015, **179**, 154-160.

130. A. Serov, M. H. Robson, M. Smolnik and P. Atanassov, *Electrochimica Acta*, 2013, **109**, 433-439.

131. A. Serov, U. Martinez and P. Atanassov, *Electrochemistry Communications*, 2013, **34**, 185-188.

132. S. Kabir, A. Serov, K. Artyushkova and P. Atanassov, *Electrochimica Acta*, 2016, **203**, 144-153.

133. K. Artyushkova, S. Pylypenko, M. Dowlapalli and P. Atanassov, *Journal of Power Sources*, 2012, **214**, 303-313.

134. S. M. Senthil Kumar, J. Soler Herrero, S. Irusta and K. Scott, *Journal of Electroanalytical Chemistry*, 2010, **647**, 211-221.

135. V. B. Baez and D. Pletcher, *Journal of Electroanalytical Chemistry*, 1995, **382**, 59-64.

136. M. Inaba, H. Yamada, J. Tokunaga and A. Tasaka, *Electrochemical and Solid-State Letters*, 2004, **7**, A474-A476.

137. M. Nesselberger, M. Roefzaad, R. Fayçal Hamou, P. Ulrich Biedermann, F. F. Schweinberger, S. Kunz, K. Schloegl, G. K. H. Wiberg, S. Ashton, U. Heiz, K. J. J. Mayrhofer and M. Arenz, *Nat Mater*, 2013, **12**, 919-924.

138. S. Proch, K. Kodama, M. Inaba, K. Oishi, N. Takahashi and Y. Morimoto, *Electrocatalysis*, 2016, **7**, 249-261.

139. J. Speder, L. Altmann, M. Baumer, J. J. K. Kirkensgaard, K. Mortensen and M. Arenz, *RSC Advances*, 2014, **4**, 14971-14978.

140. E. Fabbri, S. Taylor, A. Rabis, P. Levecque, O. Conrad, R. Kötz and T. J. Schmidt, *ChemCatChem*, 2014, **6**, 1410-1418.

141. S. Kabir, A. Serov and P. Atanassov, *ECS Transactions*, 2016, **72**, 39-47.

142. C. Tran, X.-Q. Yang and D. Qu, *Journal of Power Sources*, 2010, **195**, 2057-2063.

143. T. Soboleva, X. Zhao, K. Malek, Z. Xie, T. Navessin and S. Holdcroft, *ACS Applied Materials & Interfaces*, 2010, **2**, 375-384.

144. Z.-S. Wu, S. Yang, Y. Sun, K. Parvez, X. Feng and K. Müllen, *Journal of the American Chemical Society*, 2012, **134**, 9082-9085.

145. J. Xiao, D. Mei, X. Li, W. Xu, D. Wang, G. L. Graff, W. D. Bennett, Z. Nie, L. V. Saraf and I. A. Aksay, *Nano letters*, 2011, **11**, 5071-5078.

146. J. Rouquerol, D. Avnir, C. W. Fairbridge, D. H. Everett, J. M. Haynes, N. Pernicone, J. D. F. Ramsay, K. S. W. Sing and K. K. Unger, *Journal*, 1994, **66**, 1739.

147. E. Antolini, *Applied Catalysis B: Environmental*, 2009, **88**, 1-24.

148. L. Calvillo, V. Celorrio, R. Moliner and M. Lázaro, *Materials Chemistry and Physics*, 2011, **127**, 335-341.

149. K. Artyushkova, M. J. Workman, I. Matanovic, A. Serov and P. Atanassov, *Angewandte Chemie International Edition*, **in preparation**.

150. T. Kondo, S. Casolo, T. Suzuki, T. Shikano, M. Sakurai, Y. Harada, M. Saito, M. Oshima, M. I. Trioni, G. F. Tantardini and J. Nakamura, *Physical Review B*, 2012, **86**, 035436.

151. K. Gong, F. Du, Z. Xia, M. Durstock and L. Dai, *Science*, 2009, **323**, 760-764.

152. S. Zhang, Y. Shao, G. Yin and Y. Lin, *Journal of Materials Chemistry A*, 2013, **1**, 4631-4641.

153. K. Artyushkova, A. Serov, S. Rojas-Carbonell and P. Atanassov, *The Journal of Physical Chemistry C*, 2015, **119**, 25917-25928.

154. S. Kabir, A. Serov, A. Zadick, K. Artyushkova and P. Atanassov, *ChemElectroChem*, 2016, **3**, 1655-1666.